

# **Strategies to Improve the Efficiency of Hybrid Solar Cells**

## **DISSERTATION**

zur Erlangung des akademischen Grades  
eines Doktors der technischen Wissenschaften  
an der Technischen Universität Graz

vorgelegt von

**DI Christopher Fradler**

Betreuer: Assoc. Prof. DI Dr. Gregor Trimmel  
Institut für Chemische Technologie von Materialien

2014

# **STATUTORY DECLARATION**

I declare that I have authored this thesis independently, that I have not used other than the declared sources / resources, and that I have explicitly marked all material which has been quoted either literally or by content from the used sources.

Graz, February 6<sup>th</sup>, 2014

DI Christopher Fradler

# **EIDESSTATTLICHE ERKLÄRUNG**

Ich erkläre an Eides statt, dass ich die vorliegende Arbeit selbstständig verfasst, andere als die angegebenen Quellen/Hilfsmittel nicht benutzt, und die den benutzten Quellen wörtlich und inhaltlich entnommenen Stellen als solche kenntlich gemacht habe.

Graz, am 6. Februar, 2014

DI Christopher Fradler

*“Technology always develops from the primitive to the complicated and then to the simple.”*

Antoine de Saint-Exupéry

# ACKNOWLEDGEMENTS

First of all, I want to thank my supervising tutor Prof. Gregor Trimmel for giving me the opportunity to work on such a fascinating topic and to write this thesis at a very kind atmosphere. Next to thank is Dr. Thomas Rath, who is not only a great scientist but also was a big help and support for me throughout the whole time.

Furthermore my thank goes to Dr. Mario Arar and Dr. Andreas Pein, colleagues and discussion partners, who became good friends. The same is true for DI Meinhart Roth and Dr. Lucas Hauser, who made life at work so pleasant and amusing. There are so much more people I got to know and learned to appreciate within the last years, who all contributed to the unique atmosphere at this institute. At this stage I want to mention “the girls from the 6<sup>th</sup> floor”, who always had time for a chat at a glass of water and brought so much fun into every single day at work.

Additionally, I want to acknowledge all partners, who have contributed to this thesis with their expertise and help: Dr. Wernfried Haas, Dr. Ilse Letofsky-Papst, Dr. Angelika Reichmann and Prof. Ferdinand Hofer for their support with electron microscopic analyses, Prof. Robert Saf for gas spectrometry analyses, Birgit Kunert and Prof. Roland Resel for the execution of XRD-measurements, Dr. Matthias Edler for the XPS measurements, Dr. Petra Kaschnitz for her support with NMR spectroscopy, Josefine Hobisch for the execution of thermogravimetric analyses, Lukas Troi for his technical support as well as the people working at the XIL-beamline at the PSI Villigen in Switzerland, Dr. Celestino Padeste, Dr. Yasin Ekinici and Michaela Vockenhuber.

Furthermore, I gratefully acknowledge financial support by the Christian Doppler Research Association and the Austrian Federal Ministry of Economy, Family and Youth, FFG, and ISOVOLTAIC AG.

Big thanks go to my friends, who enrich my life so much and in so many different ways.

Last, and most of all, I want to thank my parents. You deserve so much more than just a few words in this work for supporting me the way you did throughout my whole life. I am deeply grateful to you.

*“Nothing inspires science as the chat with colleagues in the hallway.”*

(Arno Penzias, American physicist 20<sup>th</sup> century)

# ABSTRACT

## Strategies to Improve the Efficiency of Hybrid Solar Cells

Hybrid solar cells gained a lot of interest within the last decade, as they offer the possibility to combine the beneficial properties of organic and inorganic solar cells. Within this work, copper indium sulfide (CIS), which was synthesized from copper and indium O-2,2-dimethylpentan-3-yl dithiocarbonate via the *in situ* route, was used as acceptor material. It was tried to improve the performance and the roll-to-roll processability of this approach by several methods. The first part describes how the annealing temperature for polymer/CIS solar cells could be significantly reduced. It is shown that at mild conditions like 140 °C, the addition of a small amount of n-hexylamine leads to a higher crystallinity of the CIS nanoparticles and thus to an efficiency increase of more than 70%. Based on these results, flexible hybrid solar cells and solar cell modules are presented.

The second part deals with the introduction of the inverted architecture to the hybrid system PSiF-DBT/CIS. An optimization of this architecture has been executed, as several different layer structures and their influences on the I-V characteristic were investigated. Thereby the light soaking effect of the titanium oxide interlayer was observed and studied.

At the end, first steps towards highly ordered hybrid solar cells have been initiated by the fabrication of vertically aligned column- and comb-nanostructures of CIS, which were obtained by conversion of the respective metal xanthates via extreme UV-lithography. These structures

are of high interest, as they offer the possibility to fabricate hybrid layers, which exhibit high efficient charge separation and charge transport.

# KURZFASSUNG

## Strategien zur Verbesserung der Effizienz von Hybrid-Solarzellen

Im letzten Jahrzehnt gewannen Hybrid-Solarzellen an Aufmerksamkeit, da sie die Möglichkeit bieten, die positiven Eigenschaften von organischen und anorganischen Solarzellen zu kombinieren. Im Rahmen dieser Arbeit wurde Kupfer-Indium-Sulfid (CIS), das über die *in situ* Route aus Kupfer- und Indium O-2,2-dimethylpentan-3-yl dithiocarbonat synthetisiert wurde, als Akzeptormaterial verwendet. Es wurde versucht mit einigen Verfahren versucht, die Leistung und die Rolle-zu-Rolle dieses Ansatzes zu verbessern.

Der erste Teil beschreibt, wie die Wärmebehandlungstemperatur für Polymer/CIS Solarzellen erheblich reduziert werden konnte. Es wird gezeigt, dass bei milden Bedingungen, wie 140 °C, die Beimengung einer kleinen Menge an n-Hexylamin zu einer höheren Kristallinität der CIS-Nanopartikel und somit zu einer Effizienzsteigerung von mehr als 70% führt. Basierend auf diesen Ergebnissen werden flexible Hybrid-Solarzellen und Solarzellen-Module hergestellt.

Der zweite Teil der Arbeit beschäftigt sich mit der Anwendung der inversen Solarzellenarchitektur auf das Hybrid-System PSiF-DBT/CIS. Eine Optimierung dieser Architektur wurde anhand der Untersuchung mehrere unterschiedlicher Konstruktionen und deren Einflüsse auf die IV-Kennlinie, durchgeführt. Dabei wurde der „Light-soaking-Effekt“ von Titanoxid beobachtet und untersucht.



Am Ende wurden erste Schritte hin zu hochgeordneten Hybridsolarzellen gesetzt, in dem vertikal ausgerichteten Säulen- und Kammnanostrukturen von CIS durch Umsetzung der entsprechenden Metallxanthate mittels extrem UV-Lithographie hergestellt wurden.

Diese Strukturen sind von großem Interesse, da sie die Möglichkeit bieten Hybrid-Schichten herzustellen, die hocheffiziente Ladungstrennung und hocheffizienten Ladungstransport aufweisen.

# TABLE OF CONTENTS

<b>INTRODUCTION .....</b>	<b>1</b>
1 Photovoltaics and the World Energy Market .....	2
1.1 World Energy Consumption and the Role of Fossil Fuels .....	2
1.2 Renewable Energy .....	4
2 Photovoltaics – An Overview.....	7
2.1 Third-generation PV.....	8
2.1.1 Multijunction Cells .....	9
2.1.2 Multiband Cells .....	10
2.1.3 Concentrator Systems.....	10
2.1.4 Hot Carrier Cells.....	11
2.2 Organic Solar Cells.....	11
2.3 Hybrid Solar Cells.....	14
2.3.1 Polymer/Nanoparticle Network Formation.....	15
2.3.2 Nanocomposite Layers via the Xanthate Route .....	17
3 Aim of this Thesis.....	18
<b>BASICS .....</b>	<b>20</b>
1 Physical Principle of Organic and Hybrid Solar Cells .....	21
1.1 Light absorption .....	22
1.2 Exciton Generation.....	24
1.3 Exciton Diffusion.....	24
1.4 Charge Separation.....	25

## Table of Contents

---

1.5	Charge Transport .....	26
1.6	Charge Collection .....	27
1.7	The Entire Energy Conversion Process .....	27
2	Architectures in Hybrid Solar Cells .....	29
2.1	Bilayer vs. Bulk Heterojunction .....	29
2.2	Nanostructured Architecture .....	31
3	Characteristic Photovoltaic Parameters .....	33
<b>FLEXIBLE HYBRID SOLAR CELLS AND MODULES.....</b>		<b>37</b>
1	Introduction .....	39
2	Experimental.....	42
2.1	Sample Preparation .....	42
2.2	Characterization .....	43
3	Results and Discussion .....	45
3.1	Flexible Hybrid Solar Cells .....	56
3.2	Hybrid Solar Cell Modules .....	57
3.3	Stability .....	60
4	Conclusions .....	61
5	Acknowledgement.....	62
6	Supporting Information .....	63
6.1	Structures of the Used Materials.....	63
6.2	Variation of the Annealing Duration.....	64
6.3	Geometries of the Hybrid Solar Cell Modules.....	65
<b>FURTHER INVESTIGATIONS ON THE INFLUENCE OF N-HEXYLAMINE</b> .....		<b>66</b>

## Table of Contents

---

1	Introduction .....	67
2	Influence on the System PSiF-DBT/CIS .....	67
3	Vanadium Oxide as Anode Buffer Layer .....	71
<b>INVERTED HYBRID SOLAR CELLS .....</b>		<b>74</b>
1	Introduction .....	75
2	Experimental Section.....	77
2.1	Sample preparation .....	77
2.1.1	Pre-Treatment of the Substrates .....	77
2.1.2	Titanium Oxide Interlayer .....	77
2.1.3	Cadmium Sulfide Interlayer .....	78
2.1.4	Hybrid Layer.....	78
2.1.5	PEDOT:PSS Layer.....	78
2.1.6	Metal Electrode.....	79
2.2	Characterization .....	79
3	Results and Discussion .....	80
3.1	Formation of the Titanium Oxide Layer .....	80
3.1.1	Layer Thickness.....	80
3.2	Inverted Solar Cells .....	82
3.2.1	Optimization of the Electron Extraction.....	82
3.2.2	Optimization of the Hole Extraction.....	86
3.2.3	Light Soaking Effect.....	88
4	Conclusion.....	92
<b>EXTREME UV-LITHOGRAPHIC CONVERSION OF METAL XANTHATES</b> .....		<b>94</b>
1	Introduction .....	96

## Table of Contents

---

2	Results and Discussion .....	97
3	Experimental Details .....	107
3.1	Sample preparation and UV-illumination .....	107
3.2	Extreme UV (EUV) interference lithography .....	107
3.3	Characterization techniques .....	108
4	Acknowledgement.....	108
5	Supplementary Information .....	109
	<b>CONCLUSION .....</b>	<b>112</b>
1	Summary .....	113
2	Outlook.....	121
	<b>APPENDIX.....</b>	<b>123</b>
1	List of Abbreviations .....	124
2	List of Tables.....	127
3	List of Figures .....	128
4	Bibliography.....	136
5	List of Publications .....	167
6	Curriculum Vitae.....	170

# CHAPTER I

## INTRODUCTION

*“I would put my money on the sun and solar technology. What a source of energy! I hope we do not have to wait for the exhaustion of oil and coal before we tackle that.”*

(Thomas Alva Edison, 1931)

# 1 Photovoltaics and the World Energy Market

## 1.1 World Energy Consumption and the Role of Fossil Fuels

White's law, named after the American anthropologist Leslie White, says:

*“Culture evolves as the amount of energy harnessed per capita per year is increased or as the efficiency of the instrumental means of putting the energy to work is increased.”*[1]

The human wish to develop, advance, and evolve culturally was and still is the driving force for technological progress. This progress tremendously accelerated within the last 250 years. Around 1760 the industrial revolution started, in the late 19<sup>th</sup> and the beginning of the 20<sup>th</sup> century, electrification took place and electrical and mechanical engineering gained in importance. The chemical industry started to grow and the introduction of assembly lines and later automation led to an increase of productivity and therefore to an enormous increase in energy demand. Within the last 50 years analog mechanical and electronic technology were displaced by digital technology and the situation became even more dramatic. The energy consumption increased drastically.

Since technology has progressed, also the world's population has increased (Figure 1), which is the second main cause of rising energy demand. This development is not about to stop in near future, as for 2050 a population of 9.6 billion is predicted by the United Nations (Ref [2]).

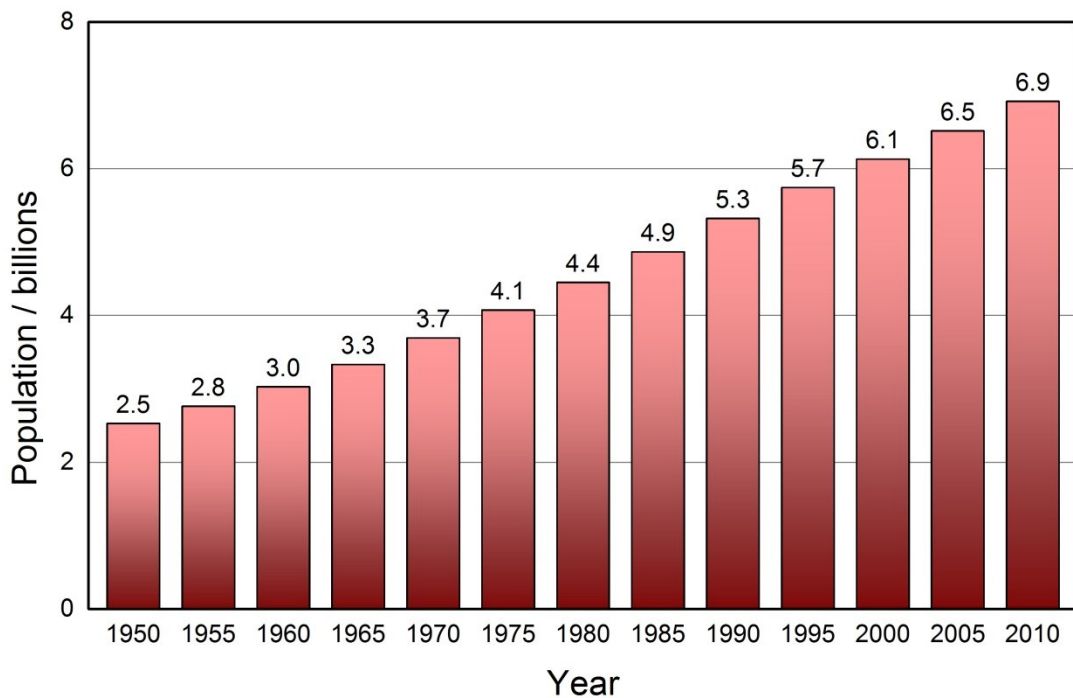


**Figure 1: Development of the world population since 1950. Data taken from Ref [2].**

To cover the growing demand on energy, since the beginning of the industrial revolution, oil is the most used energy source [3]. Together with gas and coal, still nearly 80% of our energy consumption is provided by fossil fuels (Figure 2) [4]; energy sources which are not renewable. Furthermore, the burning of fossil fuels produces carbon dioxide and therefore is one of the main causes of global warming. The International Energy Agency (IEA) predicts a long-term average global temperature increase of 3.6 °C [5,6], which might lead to a climate change. This would result in retreat of the glaciers and a higher risk for heavy rain [7], floods [8] and heat waves [9], and therefore have heavy impact on life on earth.



## 1.2 Renewable Energy

*“One day we will run out of oil, it is not today or tomorrow, but one day we will run out of oil and we have to leave oil before oil leaves us, and we have to prepare ourselves for that day.”*

(Fatih Birol, chief economist of the IEA, November 2011)

To be ready for that day it is necessary to shift the energy production from fossil fuels to renewable energy sources. By now, renewables cover already 19% of the global energy demand (Figure 2) and by 2015 they will become already the world’s second-largest source of power generation [5]. Renewable energy (like wind, solar, geothermal, wave and tidal), at an average annual growth rate of 6.7%, is expected to be the fastest growing segment of the energy industry over the period until 2030 [10]. But still there is a long way to go, to reach complete independence of non-renewable energy sources.

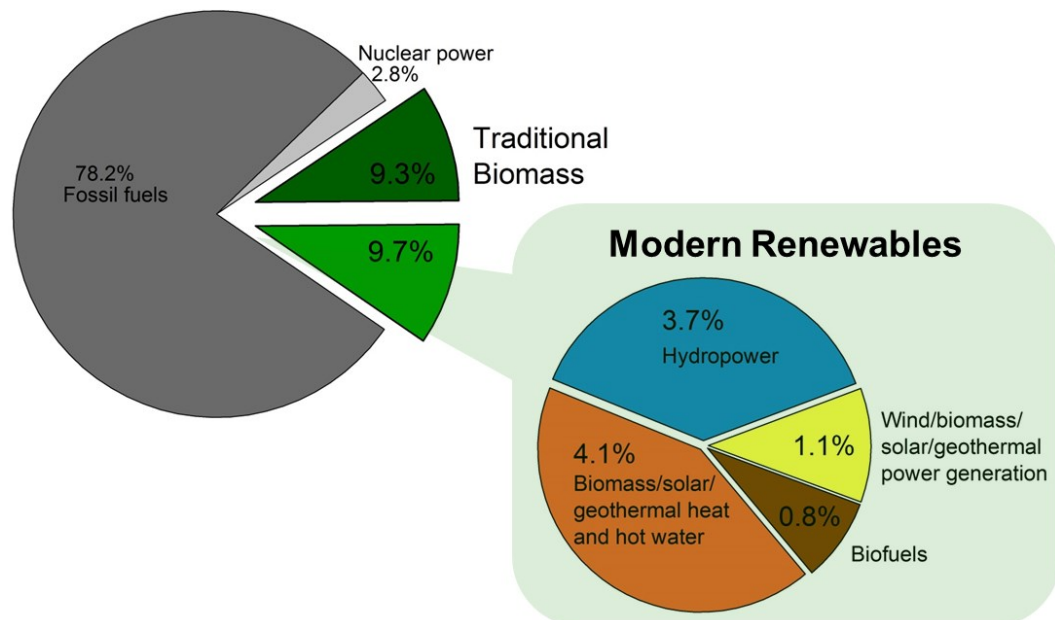


**Figure 2: Estimated renewable energy share of global final energy consumption, 2011. Data taken from Ref [4].**

Solar power is still covering just a very tiny amount of the whole energy demand. It is also not yet the strongest representative of the renewable energy section, but it is by far the fastest growing renewable technology [5] (growth rates are depicted in Figure 3).

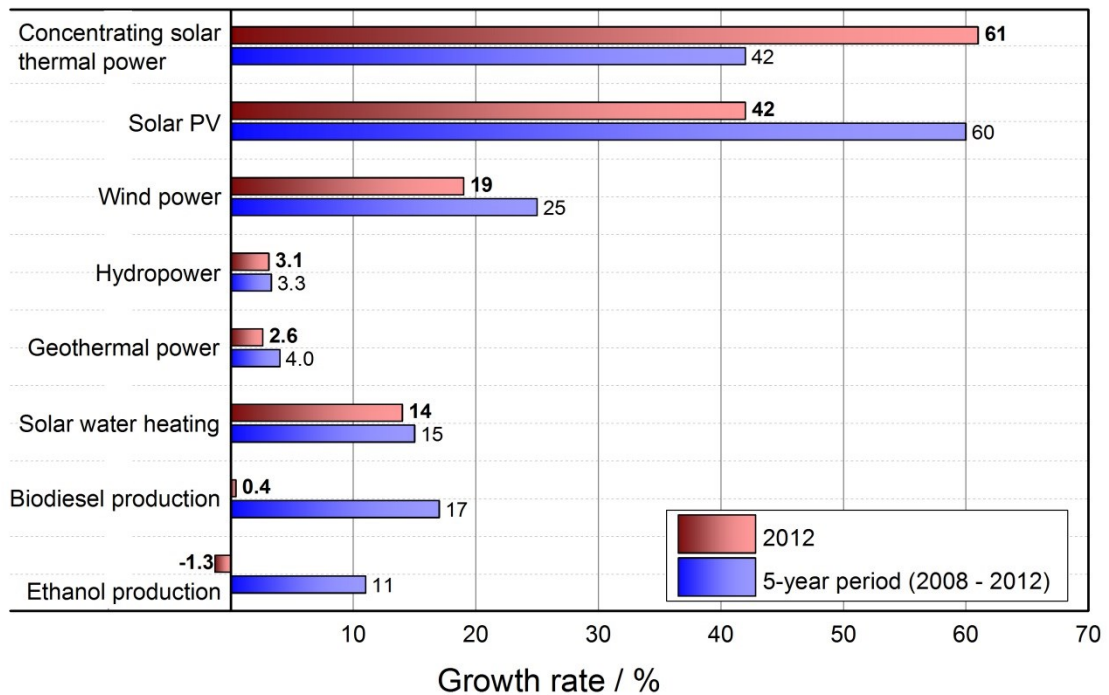


**Figure 3: Growth rates of renewable energy technologies in 2012. Data taken from Ref [4].**

Concentrated solar power (CSP) focuses a large area of sunlight onto a small area, by using optical devices like mirrors or lenses. Absorbing materials convert the sunlight to heat that drives a heat engine, which is connected to an electrical generator. In 2012 the global capacity was 2550 megawatts, which means a sevenfold increase since 2006 [4].

The solar photovoltaic (PV) market has increased even more over the last years as it reached a global operating capacity of 100 gigawatts in 2012 (Figure 4).

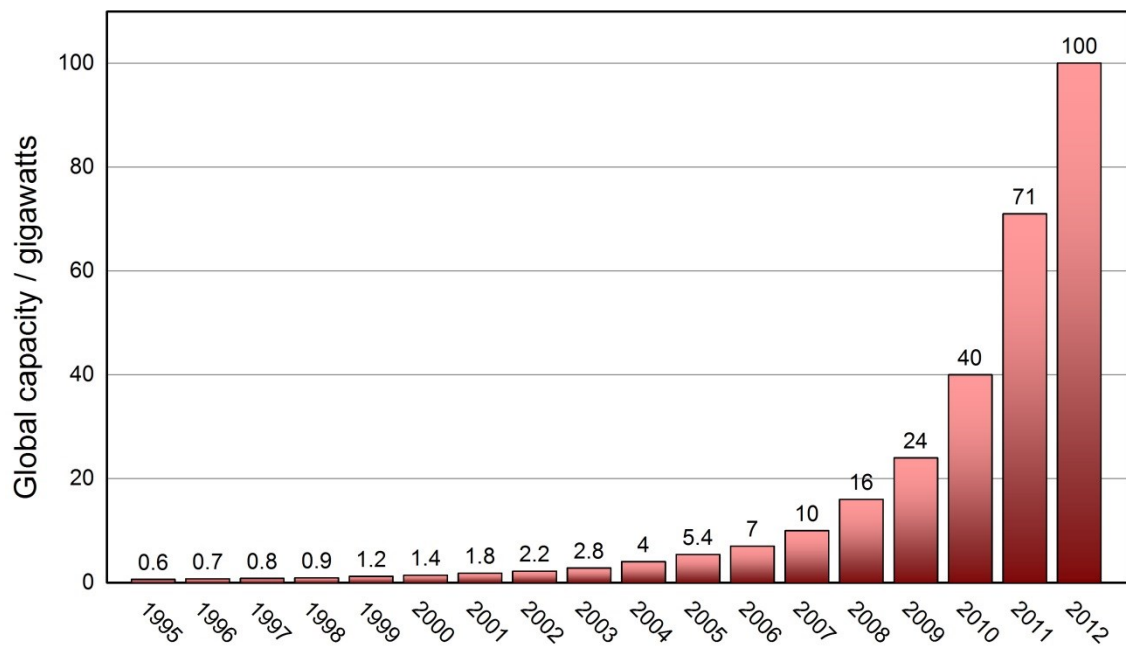


**Figure 4: Global capacity of solar photovoltaics. Data taken from Ref [4].**

Europe was the driving force for this development for years and still is dominating the PV market, with Germany being in the pole position, with 7.6 GW of newly connected systems in 2012 (Figure 5)[11].

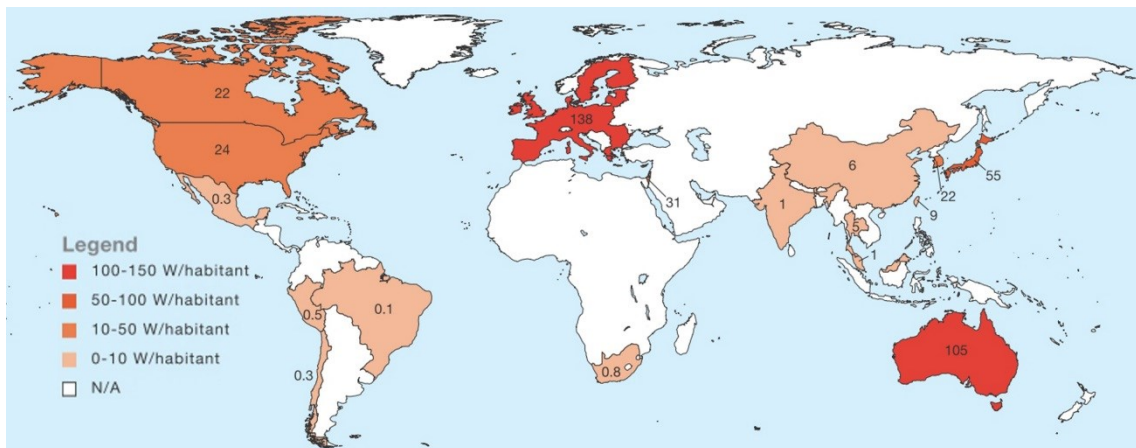


**Figure 5: A “World Power Map”, which shows that Europe is leading the way on the PV market at the moment (data from 2012 was used). © by the European Photovoltaic Industry Association (Ref. [11]).**

Nevertheless Europe's market share was reduced from 74% in 2011 to 55% in 2012, which is an indication, that the rest of the world is starting to use its potential, which is clearly bigger than the one of Europe [11], where the solar irradiation is relatively modest. In 2009, China was the only country located inside the world's Sunbelt (region between the 35<sup>th</sup> parallel north and the 35<sup>th</sup> parallel south) and being listed within the top ten PV markets [12]. Since then also India and Australia became main markets, while several countries from regions with very high solar irradiation, like Africa, the Middle East, South East Asia and Latin America, are on the brink of starting their development [6]. There is definitely a lot of untapped potential for growth for photovoltaics.

## **2 Photovoltaics – An Overview**

Photovoltaic (PV) cells convert incident photons into direct current. Solar cells are usually classified into three so-called generations. First generation PV is based on high-quality fabrication of crystalline silicon PV devices. The theoretical efficiency limit for solar cells with an ideal optical bandgap of 1.43 eV was calculated to be 31% by Shockley and Queisser, introducing the theory of the detailed balance limit [13]. According to its bandgap of 1.1 eV, which is not perfectly matching the maximum of solar radiation, the limit for silicon is 29% [14]. State of the art crystalline silicon solar cells reach efficiencies up to 25% [15,16], which means that the gap for further improvement of this technology has become quite narrow. In order to reach such high efficiencies, very pure silicon is needed, and due to the energy-requiring and time-intensive process, the price is high compared to the power output [14]. Nevertheless, this technology is still dominating the commercial market.

Thin-film technology is the main developing step of second generation solar cells. Compared to crystalline silicon based cells they are only a few micrometers thick and can be made from layers of different semiconducting materials. Besides amorphous (a-Si) and microcrystalline ( $\mu\text{c-Si}$ ) silicon, with which efficiencies slightly above 10% [17,18] can be reached, there are mainly two representative materials of this category namely cadmium telluride (CdTe), and copper indium gallium diselenide (CIGS), both showing efficiencies of about 20% [16,19,20]. The production of solar panels of this technology is much cheaper, due to using less material and lower cost manufacturing processes.

## 2.1 Third-generation PV

The term third-generation is used about many different technologies, which try to combine thin-film deposition techniques and higher efficiency. To reach that goal third-generation photovoltaics try to overcome the Shockley-Queisser limit, as they bypass at least one of the restrictions that were made by Shockley and Queisser and are valid for first-generation PV. A lot of research is done on different concepts of this young PV generation. Within this section I will give a short introduction into some of them. Organic and especially hybrid solar cells will be discussed afterwards in more detail.

The two main loss mechanisms in a crystalline silicon solar cell are its inability to absorb photons with less energy than the bandgap and thermalization of photon energies exceeding the bandgap [14]. Further losses occur at the junction, the electrode contact and through recombination (Figure 6).

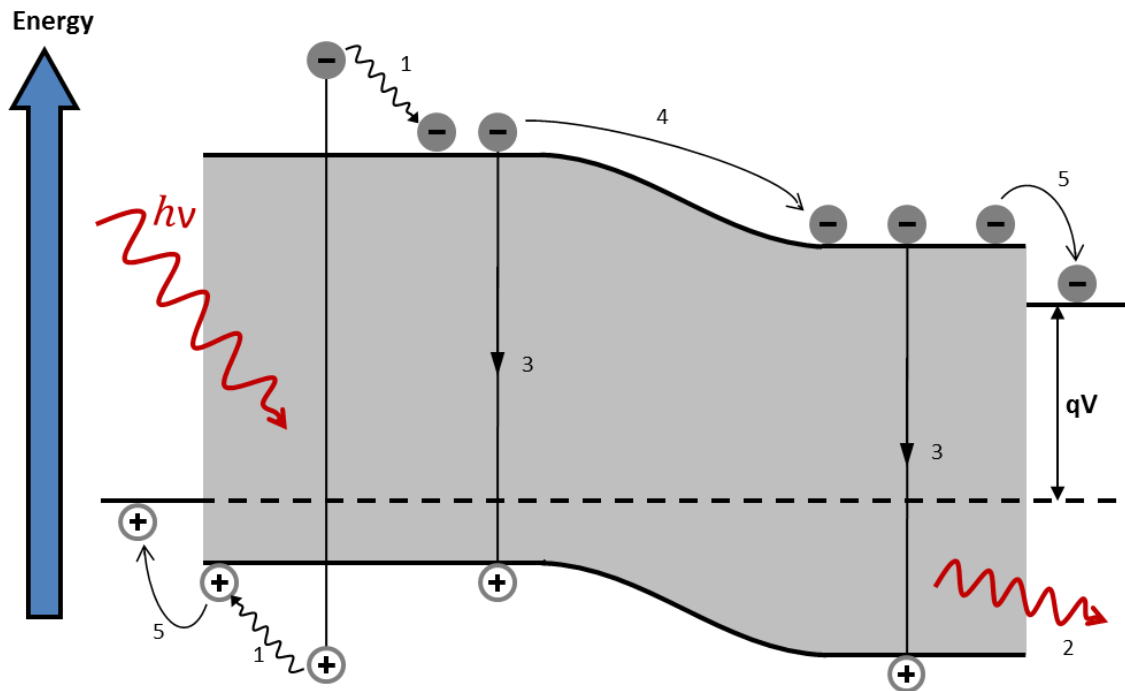


**Figure 6: Loss mechanisms in a standard solar cell. 1) thermalization of photons exceeding the bandgap; 2) non-absorption of photons below the bandgap; 3) recombination of the charges; 4) junction loss; 5) contact loss**

### 2.1.1 Multijunction Cells

By increasing the number of energy levels, multijunction solar cells eliminate losses through thermalization and non-absorption [21] (Figure 6). At this concept, multiple single cells, with slightly differing bandgaps are stacked over another, with the highest bandgap material being on top [21]. Therefore the photons get absorbed selectively after another from the energy-rich ones to the energy-poorer ones [21]. The larger the number of cells in the stack, the higher the theoretically achievable efficiency, with a limit of 86.8% for an infinite stack of independently operated cells [22]. According to Green et al. (Ref [16]) the efficiency record for multijunction devices has been extended by Sharp Solar to 37.9% for unconcentrated light by using a triple-junction system.

### 2.1.2 Multiband Cells

Another way of introducing further energy levels is demonstrated by multiband cells. In this case an additional energy level is represented by a so called impurity band, which is also named intermediate band, due to its energetically location in between the conduction band (CB) and the valence band (VB) of the semiconductor. The introduction of such an impurity band is achieved by inserting elements like Cr [23], Se [24] or rare earths [21]. Therefore, again the losses through mismatching of photon energy and the semiconductors standard single-bandgap are reduced. The spectral sensitivity of this concept is significantly lower than in multijunction solar cells [21]. The current across the two lower energy levels still has to be equal, but the main current across the bandgap is independent [14].

### 2.1.3 Concentrator Systems

Concentrated photovoltaic technology focuses a large amount of sunlight onto a small area of solar cells, by using optical lenses and mirrors. Therefore the photovoltaic cells are exposed to a solar radiation of higher intensity. Concentrator systems are very suitable for multijunction cells, because as the number of cells in the stack increases, the voltage-to-current ratio increases, thus decreasing resistive losses in the high current densities of concentrator cells [14,25]. Thus, again Sharp Solar was able to increase the energy efficiency of a triple-junction solar cell in combination with concentrator systems to 44.4% (Ref [16]).

However, concentrators require direct sunlight and in contrast to flat-plate cell modules, they do not work with a cloudy sky [14]. Concentrator systems are primarily suitable for regions of low cloud coverage and large

photovoltaic installations, as they represent the addition of another complex component to the whole PV system [14].

#### **2.1.4 Hot Carrier Cells**

Hot carrier cells represent a further approach to increase efficiency. This technologies strategy is to allow the absorption of a wide range of photon energies and then collect the photogenerated carriers before they have a chance to thermalize [14]. This process can be achieved by slowing down the rate of photoexcited carrier cooling, which is caused by phonon interaction in the lattice [14]. Therefore the time gap in which the carriers can be collected while they are still “hot”, which means that they are still at their initial elevated excitation level, increases [14]. As a result hot carrier cells achieve higher voltages [26]. A key factor in this concept is the extraction of carriers from the device, which has to occur at a very narrow range of energies through selective energy contacts [14].

## **2.2 Organic Solar Cells**

Over the last years in particular, polymer-based solar cells moved into the point of interest. The working principle of organic semiconductors is intensively discussed at the beginning of the following chapter (page 21). But let me note at this stage that it is fundamentally different from a crystalline inorganic semiconductor with a 3D crystal lattice, where the individual LUMOs and HOMOs form a conduction band and a valence band throughout the material [27]. In organic semiconductors the intermolecular forces are too weak to form 3D crystal lattices and thus the HOMO and the LUMO do not interact strong enough to form a CB and VB [27].



Polymer-based solar cells represent a very cheap source to harvest solar radiation energy [28]. Further they offer the possibility to fabricate flexible, light-weight solar cells by a high-throughput roll-to-roll process [28] as printing coating techniques can be used [29]. Although the technology is very new, a lot of research is going on in this field at the moment, and thus the 10% limit was exceeded recently [16,30,31]. An advantage of the technology is the fact that the possible combinations of donor and acceptor materials are almost infinite, and therefore the potential fields of application are numerous. At the same time their variability is kind of a trap for organic solar cells [32]. According to Jorgensen et al. [32] nearly 9000 papers dealing with OPV have been published in 2012, but all this research is not focused on one or at least some specific variations of materials, as the “perfect” construction is not found yet [32]. Therefore, the authors have to deal with different problems and all the work, which is done, is not going towards the exact same purpose. Nevertheless the development of OPV in this millennium was and still is up-and-coming. This astonishing progress is apparent from the efficiency chart of the National Renewable Laboratory (NREL) of the United States (Figure 7), which depicts the progress of all different kinds of PV technologies.

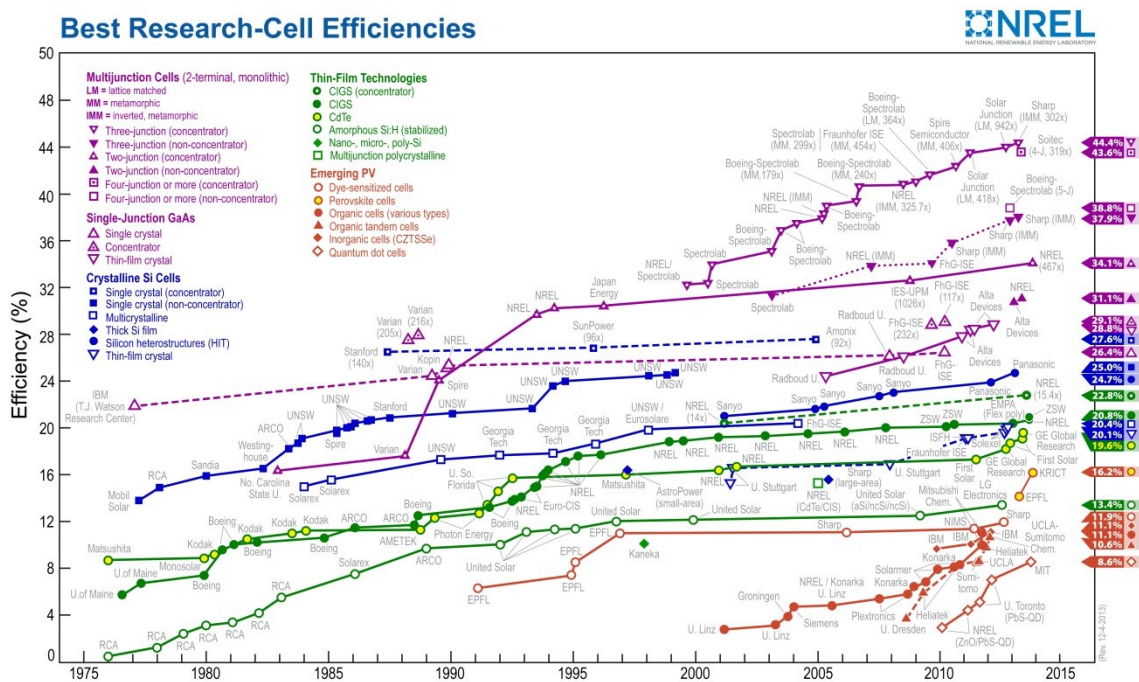


**Figure 7: NREL efficiency chart [33]. Watch the rapid progress of OPV (depicted as red dots) within the last 10 years.**

If the potential for commercialization of a PV technology is discussed, there are three aspects considered to be technology-driving: efficiency, costs and lifetime (Figure 8). Besides the already discussed increase in efficiency also quite promising lifetime studies of organic photovoltaics have been published [34,35]. Similar to efficiency, the stability of organic cells is improving, but not at the level first-generation cells yet. Due to the possible fabrication technologies (roll-to-roll, printing) and especially the low layer thicknesses and the resulting little amount of material per area needed, organic photovoltaics are considered to be competitive on the PV market concerning costs. There is still a way to go for this technology, but recent results and the fact that there is no end of progress in sight allows us to look positively to the future.

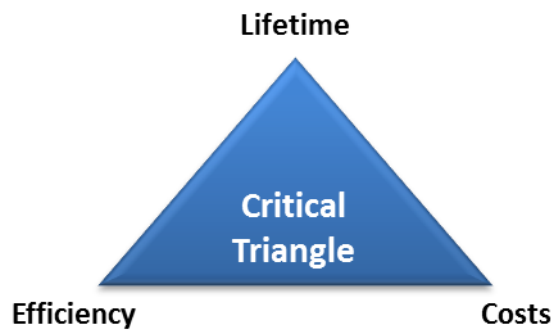


**Figure 8: The critical triangle for PV. All types of new generation solar cells have to fulfil the three requirements, lifetime, efficiency and costs, simultaneously; otherwise they will not be able to compete with established PV technologies [36].**

### 2.3 Hybrid Solar Cells

The challenging goal for photovoltaic researchers is to optimize energy conversion of the incident solar flux to electrons in an external circuit [37]. One promising idea to manage that is represented by organic-inorganic hybrid cells based on conjugated polymers and nanocrystalline inorganic semiconductors, why they are often also named nanoparticle-polymer solar cells. The inorganic part provides high charge carrier mobility while the polymer part exhibits a high absorption coefficient [38], which guarantees a more efficient photon absorption. This technology offers the possibility to combine the beneficial properties of organic and inorganic solar cells. Energy saving processing technologies that are suitable for high throughput low cost production, such as roll-to-roll printing and coating and low temperature annealing, can be applied for hybrid solar cells as well as for organic PV. Additionally, the inorganic phase can contribute to the generation of charge carriers through the absorption of photons at wavelengths, which are not covered by the conjugated polymer [39,40]. At this point it has to be noted, that this effect was also detected and proven

for PCBM in organic PV [41], but is greater and more substantial in hybrid cells [42]. They offer the possibility of tailoring the complementary absorption profile of the inorganic nanoparticles [43]. This is made possible by the quantum confinement effect [44], which describes the change of the bandgap and thus the absorption profile of inorganic nanostructures in dependence of its size, shape and composition. Therefore, the photon absorption yield in hybrid solar cells is not only higher than in single-bandgap silicon solar cells of the first-generation, as silicon exhibits a low bandgap of 1.1 eV, but also than in OPV. Typical used inorganic materials in hybrid solar cells are cadmium selenides [45], cadmium sulfides [46], lead selenides [47], lead sulfides [48], copper indium selenides [49] and copper indium sulfides [50,51].

As mentioned above, promising stability data for organic solar cells [34,35] has been published recently. Nevertheless, hybrid PV technology should be able to achieve even better lifetime results, due to the fact that inorganic acceptor materials are more environmentally stable [52] and not that sensitive to solar radiation concerning degradation [53].

### **2.3.1 Polymer/Nanoparticle Network Formation**

To prepare photoactive hybrid layers (HL) mainly three different approaches have been established [38]. The classical approach is to synthesize the nanoparticles and then mix them with the conjugated polymer. The synthesized nanoparticles tend to agglomerate and as a result not only a inhomogeneous hybrid network is formed, but also the layers get very rough and thus the solar cells are shorted. To avoid agglomeration, the nanoparticle synthesis is done with capping agents. In the following, these capping agents have to be removed by a ligand exchange, as their presence would lead to an isolation of the nanoparticles

in the polymer matrix and therefore charge carrier generation and transport would be impeded [38]. At this stage it has to be noted that besides capping agents also by-products and generally any substances, which are not involved in the energy conversion process, should not be present in the photoactive layer in order to avoid above named negative effects.

To synthesize a vertically-aligned highly ordered inorganic nanostructure, which is then infiltrated by an organic polymer is the second approach. Such a comb-like structure can be realized on different ways, which are discussed in more detail in the following chapter on page 31. The drawbacks of this approach might be the longer reaction times and higher temperatures that are needed, which are not suitable for roll-to-roll production processes [38].

The *in situ* formation of nanoparticles out of precursors directly within the polymer matrix is another, quite elegant approach. This is a one-step-process, where the synthesis of the nanoparticles is carried out in the presence of the polymer in the coating solution or in the active layer [38]. The polymer acts as capping agent and thus prevents agglomeration. Therefore, no stabilization ligands are necessary [38], which is a big advantage of the *in situ* approach. The separated synthesis offers a higher controllability of the nanoparticles size and shape, but the presence of capping agents inevitably leads to separation of the nanoparticles [54]. If the originally long-chained ligands are exchanged by smaller ones, the inter-particle distance reduces and some percolation pathways can be detected [54]. Compared to that *in situ* prepared nanoparticles show intimate contact to each other and lead to continuous inorganic pathways throughout the conjugated polymer matrix [54]. Thus the *in situ* approach leads to increased charge separation efficiency [38,54].

### 2.3.2 Nanocomposite Layers via the Xanthate Route

Metal xanthates proved to be suitable precursor materials for the synthesis of CdS [55] and CIS nanoparticles [56]. The basic process of this work is the *in situ* synthesis of copper indium sulfide by using copper and indium xanthates (copper and indium O-2,2-dimethylpentan-3-yl dithiocarbonate) as precursors. Many different xanthates were synthesized to finally get to the above named ones (the chemical structures are depicted in Figure 9), which show the requested high solubility in organic solvents like chlorobenzene (CB).

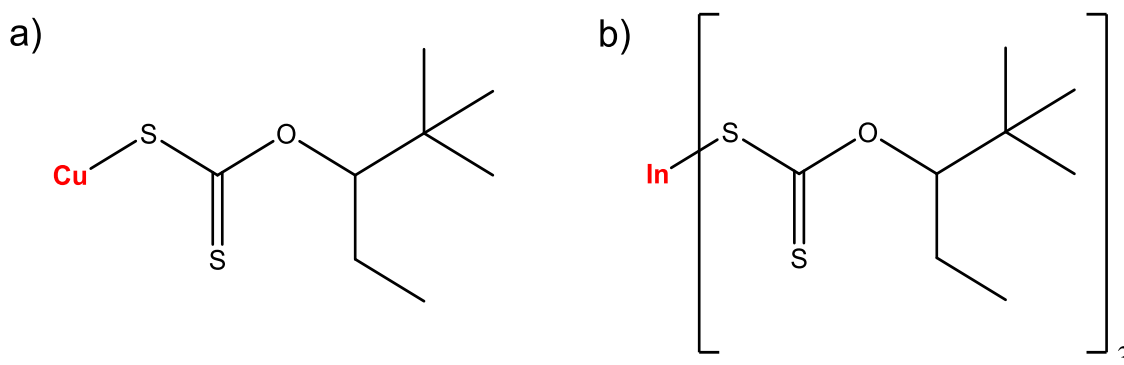


**Figure 9: Chemical structures of the used CIS-precursor materials:**

**a) copper O-2,2-dimethylpentan-3-yl dithiocarbonate**

**b) indium O-2,2-dimethylpentan-3-yl dithiocarbonate**

To form a hybrid polymer/CIS layer a bulk solution containing copper xanthate, indium xanthate and the polymer in the required ratios is applied to a substrate by doctor blading and subsequently annealed at temperatures below 200 °C. During this heating step the metal xanthates are converted to CIS and form a continuous network of nanocrystals within the polymer matrix. The byproducts of this reaction leave the layer, as all of them are volatile [56].

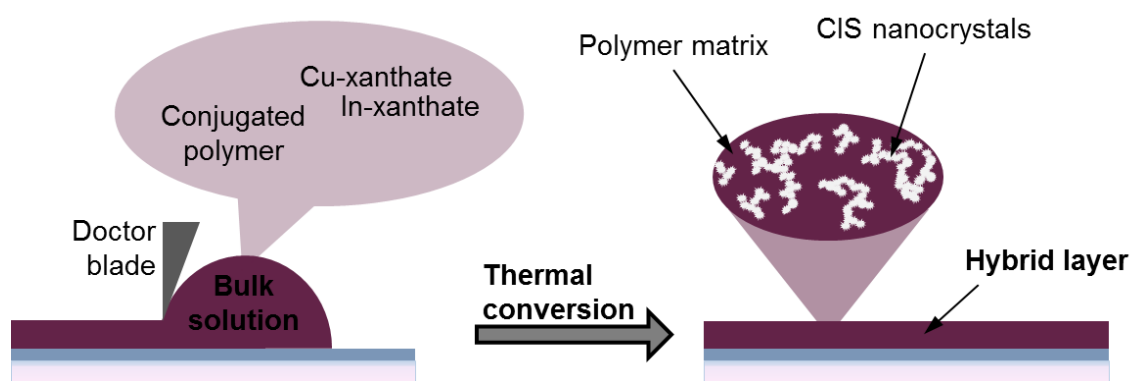


**Figure 10: Schematic depiction of the hybrid layer formation process via the *in situ* xanthate route.**

### 3 Aim of this Thesis

The aim of this thesis was to investigate different approaches, which offers the possibility to enhance the efficiency of polymer/copper indium sulfide hybrid solar cells based on the xanthate route. In chapter III and IV the possibility to establish a low-temperature fabrication process for polymer/CIS solar cells, which should allow the use of polymer foil devices to build flexible hybrid solar cells by using a specific additive compound, is analyzed. The impact of the additive on the performance of polymer/CIS solar cells and on their stability was tested and its influence on the hybrid layer formation process was physically but also chemically investigated.

Another idea to fabricate more efficient but also more stable solar cells was to introduce the inverted architecture, which is already used in organic PVs and in other hybrid system as well, to the polymer/CIS system. This work is summarized in chapter V. In dependence on that, chapter VI deals with fabrication of vertically aligned CIS-nanostructures from the respective copper and indium xanthate precursors by extreme UV-lithography. Ordered structures are a field of high interest due to the

fact that they can be infiltrated by a conjugated polymer and thus lead to a photoactive hybrid layer, which offers high efficient charge separation and charge transport at the same time.

The basics and fundamental physical principles of all the work in this thesis are explained in chapter II.



# **CHAPTER II**

## **BASICS**

*“I learned very early the difference between knowing the name of something and knowing something.”*

(Richard P. Fineman, physicist, 20<sup>th</sup> century)

## 1 Physical Principle of Organic and Hybrid Solar Cells

Compared to silicon or other typical inorganic semiconducting materials, organic semiconductors have a relative low dielectric constant ( $\epsilon_r \sim 3$ ) [57,58]. Therefore the whole energy conversion process in a hybrid solar cell is not only different but also more complex and consists of several steps that are described in detail below (Figure 11).

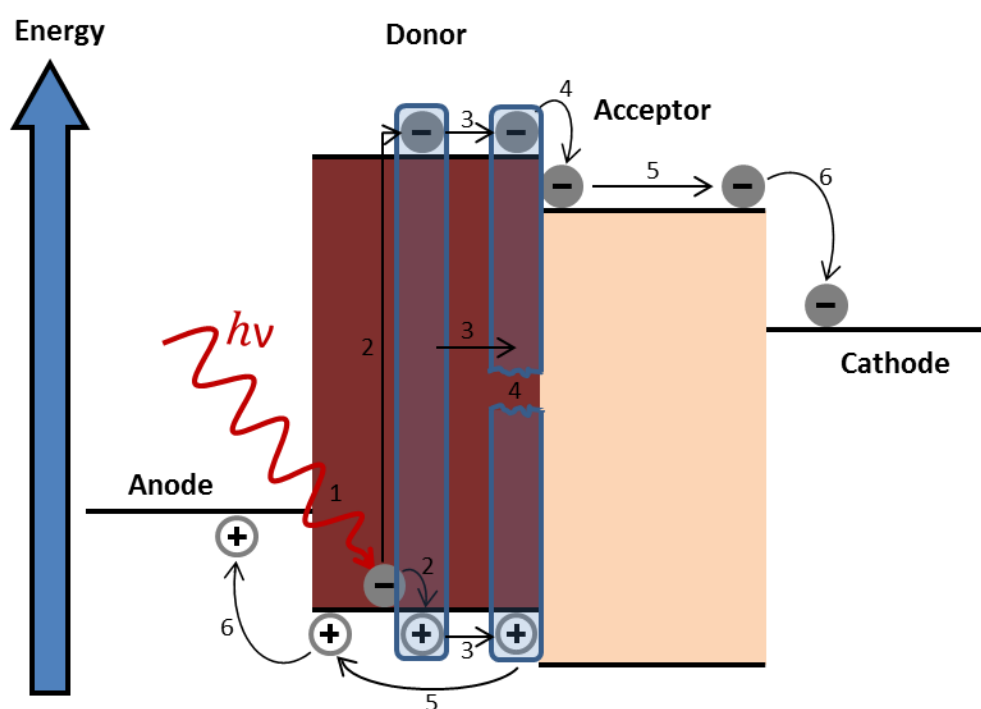


**Figure 11: Scheme of the energy generation process in a hybrid solar cell for photons absorbed by the organic donor phase. Substeps of the energy conversion process: 1) light absorption, 2) exciton generation, 3) exciton diffusion, 4) charge separation, 5) charge transport, 6) charge collection. Photon absorption by the inorganic phase is neglected for clarity.**

## 1.1 Light absorption

The light absorption rate is determined by the optical absorption coefficient of the respective material. At the beginning, very common photoactive polymers like P3HT, MEH-PPV [59,60] or MDMO-PPV [61,62] have a bandgap of 2.0 eV or higher and thus the absorption is limited to about 30% of the total photon flux under air mass 1.5 (AM1.5) [62]. AM1.5 describes the spectrum of the sunlight, when it irradiates under a solar zenith angle ( $\theta$ ) of  $\sim 48.2^\circ$ , which is the illumination that corresponds to the standard testing condition (STC). The air mass is defined as follows.

$$AM = \frac{1}{\cos \theta} \quad (1)$$

Within the last ten years, intense research was directed towards the synthesis of photoactive polymers, which have a bandgap below 2.0 eV have been synthesized [63–65], in order to harvest a greater amount of photons. Nevertheless no polymer is able to cover the whole solar spectrum. Therefore in hybrid cells an inorganic material is chosen, which covers supplementary parts of the spectrum. As mentioned already, nanocrystals or nanoparticles in hybrid cells are able to contribute to the absorption in a considerably greater amount than PCBM in organic cells. The UV—Vis spectra of typical organic and inorganic materials, as they are used in hybrid solar cells are depicted in Figure 12.

The extinction constant of organic semiconductors is higher than the one of inorganic photovoltaic materials [66]. A film of about 300 nm would be enough to absorb most of the incident light at the polymers photoactive spectral range [67]. Nevertheless, the layer thickness always is a compromise between light absorption and charge transport, due to the fact that the charge mobility in organic semiconductors is relatively low

compared to their inorganic counterpart. To secure good charge mobility and thus achieve efficient charge transport, it is crucial to keep the thickness of the polymer layer relatively thin [68]. The optimized layer thickness for most of the polymer solar cells is not more than 100 nm [69,70].

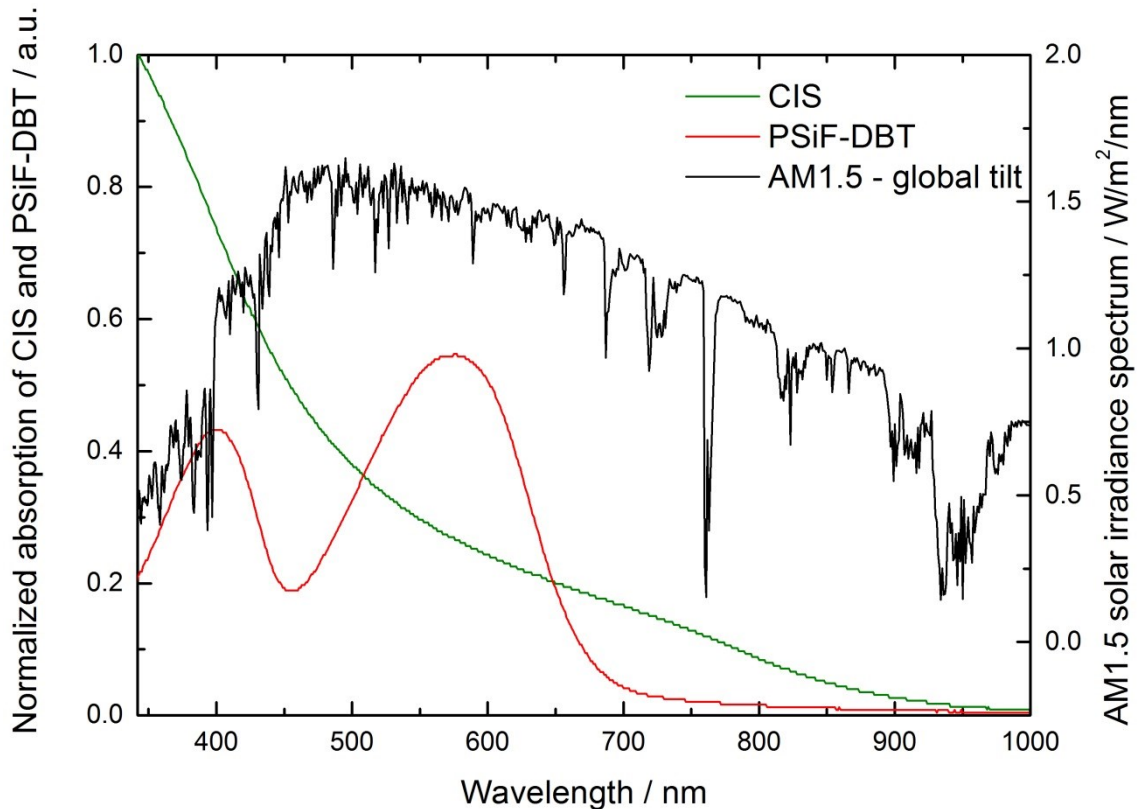


**Figure 12: black: solar spectrum AM 1.5 (global tilt);**

**green: absorption spectrum a typical inorganic semiconductor (CIS);**

**red: absorption spectrum of a typical low bandgap polymer (PSiF-DBT)**

Furthermore the absorption of a solar cell can be increased, by light management approaches. Light scattering and trapping inside the cell structure is a possibility to increase the path length of incoming light. Such trapping schemes for instance can be realized by using textured transparent conductive oxides [71] or textured glass substrates [72]. These technologies are mainly investigated for silicon solar cells, but can be used

for any PV technology. Another way to increase the overall amount of sunlight which strikes the solar cell is to use reflective backsheets, which redirect the sunlight that is not absorbed by the solar cell in the first place, to strike the photoactive layer for a second time. On the other side, specific frontsheets can be applied, which reduce the reflection, and therefore increase the amount of photons that pass the top of the cell.

## 1.2 Exciton Generation

In an organic semiconductor, an incident photon leads to the excitation of an electron. This electron energetically “moves” from the highest occupied molecule orbital (HOMO) to the lowest unoccupied molecule orbital (LUMO) and the respective hole remains in the LUMO. Nevertheless, electron and hole are coulombically bound. The force of this coulomb attraction is proportional to  $1/\epsilon_r$  (relative permittivity) [66]. Compared to silicon or other typical inorganic semiconducting materials, organic semiconductors have a rather low relative permittivity ( $\epsilon_r = \sim 3$ ) [57,58]. This means that in an organic semiconductor a still quite strongly, coulombically bound electron-hole pair, a so called “exciton”, is formed, whereas in an inorganic semiconductor coulomb attraction can be neglected [66].

## 1.3 Exciton Diffusion

To generate free charges out of an exciton, it is necessary to break the excitonic binding by transferring the electron to a second compound, named acceptor. This process, named charge separation, takes place at the donor-acceptor (D-A) interface and is explained in more detail in the following section of this chapter. Therefore, the exciton has to diffuse from

any place within the polymer matrix, where it might have been generated, through the polymer phase towards the donor-acceptor (D-A) interface, first. The exciton diffusion in conjugated polymers is limited to a length of about 10 nm [73–75]. That means that the exciton generation has to happen within the range of 10 nm from any point of the D-A interface, to get separated free charges. If an exciton is generated too far from the D-A interface, the diffusion would take too much time and therefore exciton annihilation processes appear to happen. The exciton will either decay via thermalization or its charges will recombine [66]. Thus it is necessary to realize a photoactive layer structure, where polymer regions, which are out of the exciton diffusion range, occur as little as possible. This can be achieved, by using a bulk heterojunction (BHJ) architecture, which is explained in more detail in section 2 of this chapter.

#### 1.4 Charge Separation

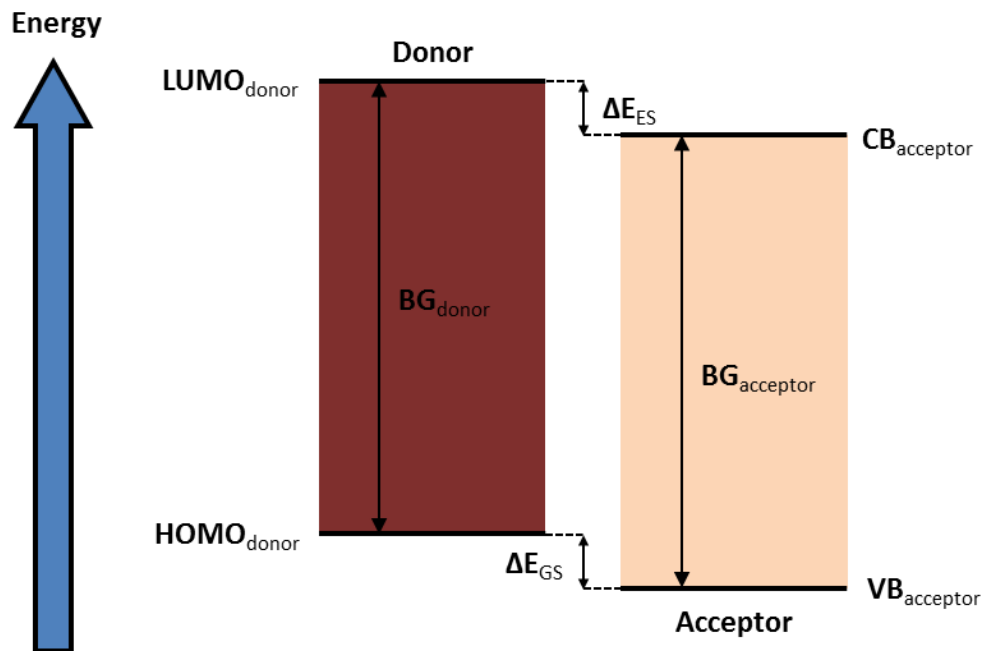


**Figure 13: General energy band diagram of a hybrid solar cell [53].**

The electron-hole binding of an exciton has an energy of about 0.4 eV [57,66,76]. The force to overcome the exciton binding energy and separate the charges is provided by the energy level offset of the LUMO of the donor and the conduction band edge of the acceptor material. In Figure 13, which shows a simplified general band diagram of a hybrid solar cell, this energy gap is named  $\Delta E_{ES}$ , as it is the excited state energy offset. To dissociate the excitons, which are formed in the inorganic acceptor phase, an energy level offset between the HOMO of the donor and the valence band edge of the acceptor, the energy offset of the ground state ( $\Delta E_{GS}$ ), is required. The energy level offsets  $\Delta E_{ES}$  and  $\Delta E_{GS}$  must be higher than the exciton binding energy; otherwise the respective charge-transfer reaction is energetically unfavorable.

Charge separation is a process that happens within about 45 fs [77], which is much faster than the competing processes of luminescence (ns) and recombination ( $\mu$ s) [66]. Thus the charge separation is a high efficient step of the energy conversion process as long as the used donor and acceptor materials fulfil the energy level alignment requirements.

## 1.5 Charge Transport

The intrinsic characteristic of polymer molecules, high trap density and dead ends in the transport net are the main limiting factors of charge carrier mobility in hybrid solar cells [78]. Because of the relatively low hole mobility in conjugated polymers, the charge transport is strongly related to the active layer thickness. If the layers get too thick, the layer mobility is the most critical material property affecting charge transport and leading to a drop in short-circuit current [68].

In addition, a morphology that offers continuous pathways for electrons and holes towards the respective electrode is necessary for efficient charge transport in hybrid cells. Isolated regions, as they appear in bulk heterojunction solar cells must be avoided or reduced to a minimum.

## 1.6 Charge Collection

The charge collection at the respective electrodes is a crucial step for the overall efficiency. The charge collection yield ( $\eta_{cc}$ ) is a function of the energy levels of the photoactive materials and the electrodes [37,79]. High efficient charge collection requires the fulfilment of the following conditions:

$$E_{F, cathode} > E_{HOMO, donor} \quad (2)$$

$$E_{F, anode} < E_{LUMO, acceptor} \quad (3)$$

In words, the fermi level of the anode ( $E_{F, anode}$ ) should be greater than the energy level of the donor's HOMO ( $E_{HOMO, donor}$ ) and the fermi level of the cathode ( $E_{F, cathode}$ ) should be lower than the energy level of the LUMO of the acceptor ( $E_{LUMO, acceptor}$ ) (Figure 11) [79]. If base metals, such as aluminum are used as electrode material, they tend to form thin oxide layers at the interface between the electrode and the photoactive layer. These oxide layers represent a potential barrier, which must be overcome by the charge carriers to get extracted.

## 1.7 The Entire Energy Conversion Process

Every single step of the energy conversion process in a hybrid solar cell is crucial. Even though some steps run nearly perfect, every single



subprocess entails losses. It is tried to keep those losses as little as possible and hence convert as much incident sunlight as possible to usable energy. The total efficiency of a hybrid solar cell is the product of the efficiencies of every single sub-step of its energy conversion process (Figure 14).

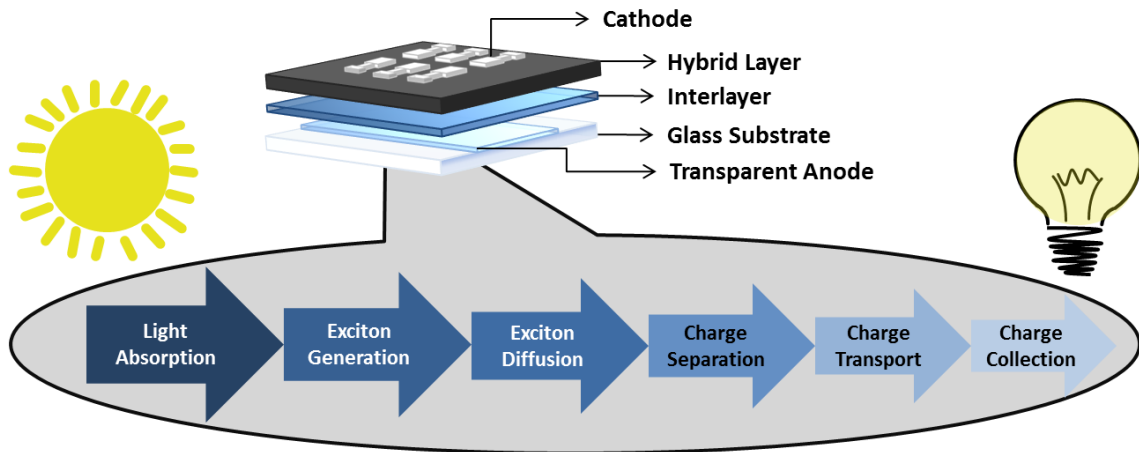


**Figure 14: Schematic depiction of the energy conversion process**

If only one of the energy conversion subprocesses in a hybrid solar cell is inefficient, its total yield will not be satisfying. Therefore a hybrid solar cells total efficiency can be described as follows:

$$\eta_{tot} = \eta_A \eta_{eg} \eta_{diff} \eta_{diss} \eta_{tr} \eta_{cc} \quad (4)$$

$\eta_{tot}$ ..... total efficiency

$\eta_A$  ..... photon absorption efficiency

$\eta_{eg}$  ..... exciton generation efficiency

$\eta_{diff}$  ..... exciton diffusion efficiency

$\eta_{diss}$ ..... exciton dissociation efficiency

$\eta_{tr}$ ..... charge carrier transport efficiency

$\eta_{cc}$ ..... charge collection efficiency

## 2 Architectures in Hybrid Solar Cells

### 2.1 Bilayer vs. Bulk Heterojunction

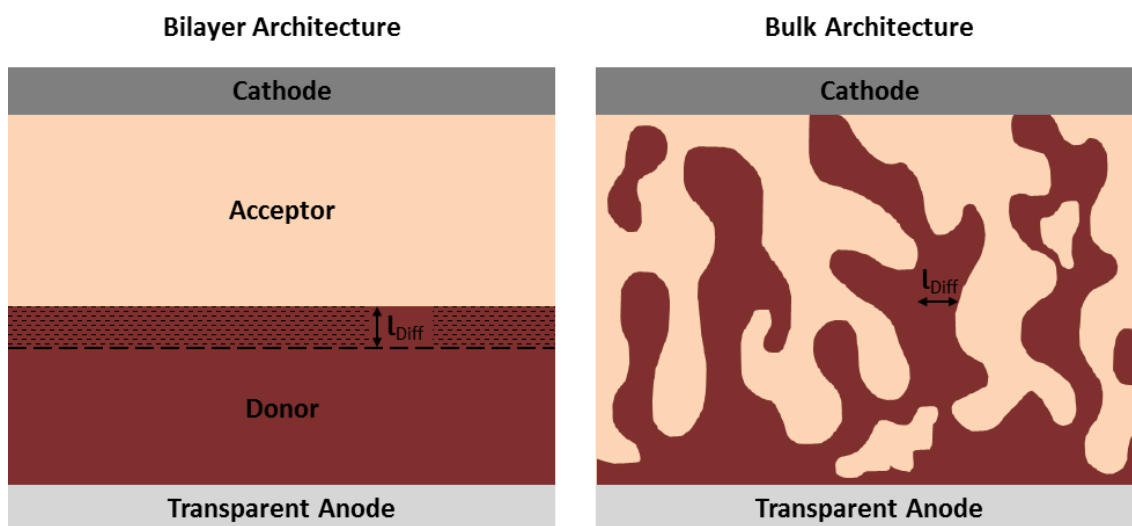


**Figure 15: Schematic depiction of a bilayer heterojunction architecture and a bulk heterojunction architecture.**

As in a bilayer solar cell the polymer film and the acceptor layer are successively applied separate from each other, the interface between these two compounds is very small in this kind of architecture. In this case only a minor part of the polymer is located within its diffusion length ( $l_{Diff}$ ). Therefore the most of the generated excitons will be annihilated before they would reach the D-A interface.

A dispersed interface, which is much larger, can be produced by mixing donor and acceptor material to a bulk solution which is subsequently applied on top of the transparent anode. The scheme in Figure 15 shows clearly that by using this method a much bigger part of the polymer phase is located within the range of the diffusion length. One issue you have to deal with in dispersed heterojunction is that of solid-state miscibility [27].

Normally conjugated polymers are not miscible and the interaction between polymer and nanocrystals is repulsive [37]. This means that the equilibrium morphology of a polymer/nanocrystals layer is a completely phase separated structure, which is equal to a bilayer structure [37]. Thus the deposition of the bulk solution should be carried out in a fast way in order to avoid that equilibration takes place. Therefore solvents with low boiling temperatures and deposition techniques, which accelerate evaporation (spin coating, doctor blading on a heated plate) are favorable [27].

Another problem to solve is the limited solubility of the acceptor phase precursors in organic solvents. Fullerene derivatives with increased solubility were synthesized, to get rid of this problem in organic PVs [80,81]. The development of the *in situ* formation route for hybrid polymer/copper indium sulfide (CIS) solar cells was also accompanied by solubility problems of the respective precursor materials. Therefore, it was necessary to adjust the side chains of the CIS precursor in order to reach a satisfying solubility [56].

If these two problems are solved, the bulk heterojunction architecture still involves the danger to create isolated regions within the photoactive layer. If an area of polymer is not connected to the anode, the separated holes cannot be extracted. Vice versa, electrons, which remain in an acceptor region that is completely surrounded by polymer phase, are lost as they cannot be transferred to the cathode. For bulk heterojunction devices, there exists a trade-off between increasing interfacial area via the intimate dispersion of phases and the creation of efficient conductive pathways through which free electrons and holes may be transported [53]. Thus, the arrangement of donor and acceptor phase is crucial to the solar cell performance [53].

Nevertheless, bulk heterojunction solar cells show much higher efficiencies than bilayer cells and thus are state of the art.

## 2.2 Nanostructured Architecture

Another interesting architecture for hybrid solar cells is based on the possibility to synthesize highly ordered vertically aligned nanostructures of the inorganic semiconducting material. Such a geometry can be infiltrated by a conjugated polymer and thus lead to a photoactive hybrid layer with a structured architecture (Figure 16). This structure can also be realized in organic PVs, but mainly by nanoimprint lithography (NIL) of the polymer, which is then infiltrated by PCBM [82,83]. Inorganic nanostructures are typically prepared by (template assisted) nanorod or nanotube growth, etching, or selected area epitaxy processes [84]. In chapter IV of this thesis the reader will be introduced to extreme UV-lithography, which represents a novel method of structuring inorganic semiconductors for photovoltaic applications.

Structuring the acceptor phase and then infiltrating it with the donor leads to a twisted, so called inverted architecture of the hybrid cell, which consists of a transparent cathode at the bottom and a hole collecting metal as anode on top (Figure 16). The inverted architecture is intensively discussed in chapter V of this thesis.

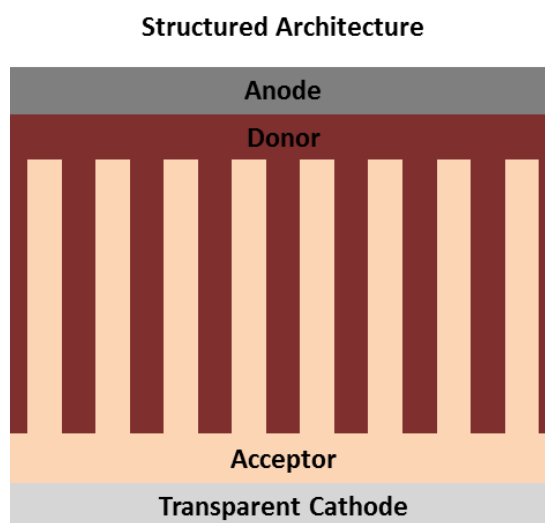


**Figure 16: Schematic depiction of a structured heterojunction architecture.**

As it can be seen from Figure 16, the D-A interface in nanostructured devices is very large, while there do not occur any isolated regions of any of the two photoactive phases. Therefore it can be denoted as an optimization of the bulk heterojunction architecture. If the structuring happens to be good and narrow, this architecture allows every exciton, wherever in the polymer matrix it might have been generated, to reach the D-A interface within the polymers diffusion length and thus recombination can be eliminated. As the diffusion length of polymers is about 10 nm [73–75] and the optimized layer thickness for hybrid cells is mostly in the range of 100 nm [69,70], the nearly ideal nanostructure would consist of rods with a length of 80 nm and gaps of 20 nm (Figure 17). This structure allows simultaneously efficient excitonic dissociation and electron transporting pathways [53].

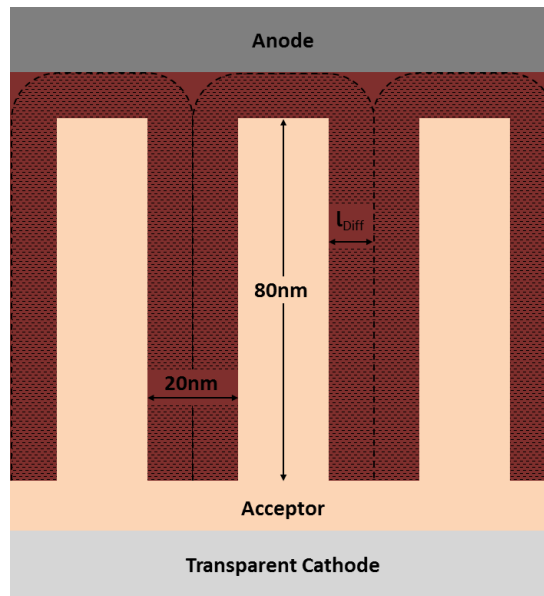


**Figure 17: Depiction of an idealized nanostructured architecture in hybrid solar cells.**

As the charge mobility of the inorganic acceptor material is much higher than the hole mobility of the donor, it is not compulsory that the width of the inorganic rods is not more than 20 nm. Nevertheless, in terms of interpenetration of the two phases a rod width of 20 nm or at least not much more would be favorable. However, the realization of nanostructures with geometries as depicted is tricky, due to the fact that such long and thin rods tend to break. Structures showing aspect ratios above 1 are difficult to synthesize.

### 3 Characteristic Photovoltaic Parameters

The electrical performance of a solar cell is determined by current-voltage ( $I$ - $V$ ) measurements under illumination, where the current of the connected solar cell is detected, while voltage runs through a certain range. The area

adjusted current density  $J$  is received by dividing the current  $I$  through the active area of the solar cell  $A$ .

$$J = \frac{I}{A} \quad (5)$$

For working solar cells the resulting graph shows a diode characteristic (Figure 18).

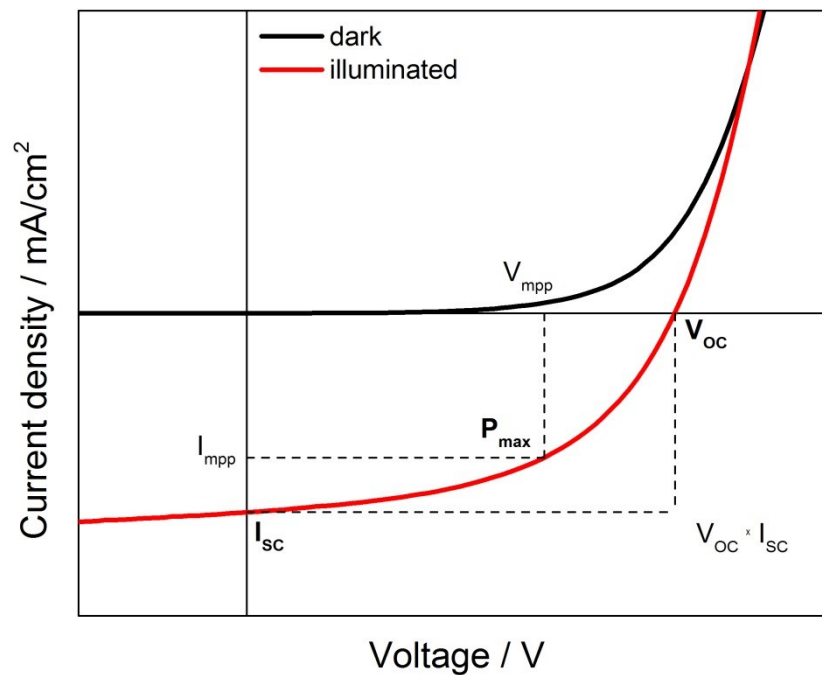


**Figure 18: Scheme of a typical J-V curve of a hybrid solar cell, with its characteristic parameters.**

The fourth quadrant of the  $J$ - $V$  curve is the part of interest, as it represents the solar cells operating zone.  $I_{sc}$  stands for the short circuit current, which is the measured current, when there is no potential applied to the cell. Vice versa  $V_{oc}$ , the open circuit voltage, is the voltage, when no current flows through the cell.

The product of voltage and the respective measured current represents the electric power of the cell ( $P$ ), which can be described as the area of the rectangle bordered by the two axes and the  $J$ - $V$  curve.

$$P = I \times V \quad (6)$$

The maximum power point ( $P_{max}$ ) should be the solar cells operating point with the respective current and voltage values named  $I_{mpp}$  and  $V_{mpp}$ . The maximum power point changes with solar radiation and temperature. Thus it is necessary to constantly adjust the operating point of an installed photovoltaic panel by a PV inverter.

The fill factor ( $FF$ ) describes the relation between the actual and the theoretical maximum power outputs and can be calculated as follows.

$$FF = \frac{I_{mpp} \times V_{mpp}}{I_{SC} \times V_{OC}} \quad (7)$$

The most significant parameter and the one by which solar cells are primarily judged is the power conversion efficiency (PCE). The PCE puts the power generated by the solar cell in relation to the incident light power ( $P_{in}$ ).

$$PCE = \frac{P_{max}}{P_{in}} \times 100\% = \frac{I_{mpp} \times V_{mpp}}{P_{in}} \times 100\% = \frac{V_{OC} \times I_{SC} \times FF}{P_{in}} \times 100\% \quad (8)$$

The external quantum efficiency (EQE), often also named incident photon to current efficiency (IPCE), is a further important value, which is experimental accessible. EQE measurements, like all quantum efficiency measurements, are executed over a range of different wavelengths to characterize the solar cells efficiency at each photon energy level. It describes the ratio of generated electrons ( $El$ ) per incident photons ( $\#Ph_{in}$ ) and is defined in the following way:



$$EQE = \frac{\#El}{\#Ph_{in}} \times 100\% = \frac{h \times c}{e} \times \frac{I_{sc}}{\lambda \times P_{in}} \times 100\% \quad (9)$$

The external quantum efficiency (EQE) is nothing but the overall conversion yield of a solar cell. Therefore it can also be described as the product of the yields of the specific steps of the light-to-power-conversion process, as mentioned already in section 1 of this chapter.

$$EQE = \eta_{tot} = \eta_A \eta_{eg} \eta_{diff} \eta_{diss} \eta_{tr} \eta_{cc} \quad (10)$$

It is important not to confuse the EQE with the internal quantum efficiency (IQE), which provides information about the ability of the respective hybrid solar cell to convert already absorbed photons to energy. More in detail it describes the ratio between generated electrons and absorbed photons ( $\#Ph_{abs}$ ).

$$IQE = \frac{\#El}{\#Ph_{abs}} = \frac{EQE}{\eta_A} = \eta_{eg} \eta_{diff} \eta_{diss} \eta_{tr} \eta_{cc} \quad (11)$$

## **CHAPTER III**

### **FLEXIBLE HYBRID SOLAR CELLS AND MODULES**

This chapter is a submission to *Solar Energy Materials & Solar Cells*, which was accepted and is currently in print [85]:

**Flexible Polymer/Copper Indium Sulfide Hybrid Solar Cells and Modules Based on the Metal Xanthate Route and Low Temperature Annealing**

Christopher Fradler, Thomas Rath, Sebastian Dunst, Ilse Letofsky-Papst, Robert Saf, Birgit Kunert, Ferdinand Hofer, Roland Resel, and Gregor Trimmel

Reproduced by permission of Elsevier

## 1 Introduction

Polymer/nanoparticle hybrid solar cells are intensively investigated because of their promising perspective of combining advantages of the polymer component such as high absorption coefficient and easy solution based processability [86] with those of the inorganic nanoparticulate semiconductors such as adjustable shape (nanodot, nanorod, tetrapod) [87], tunable absorption properties (quantum confinement effect) [88], and high conductivity [89]. Various polymer/nanoparticle material combinations have been reported as absorber layers of bulk heterojunction hybrid solar cells, for recent reviews see e.g. Ref. [53,86,88,90–96]. Most prominent examples are combinations of conjugated polymers such as polythiophenes, poly-para-phenylenevinylenes, or various low bandgap polymers with nanoparticles of, for example, CdSe [97], CdS [52], CdTe [98], CuInS<sub>2</sub> (CIS) [56], PbS [99] or ZnO [100]. Currently, the best polymer/nanoparticle hybrid solar cells exhibit maximum power conversion efficiencies (PCEs) between 4 and 5.5% [52,98,101,102].

Different synthesis approaches have been introduced for the preparation of organic-inorganic hybrid solar cells, which follow mainly three synthesis strategies: i) the classical approach, ii) the infiltration approach and iii) the *in situ* preparation [38]. The most applied route is the classical approach (i). In this case, the nanoparticles are prepared via colloidal synthesis routes. After a purification step and/or ligand exchange process the nanocrystals are subsequently mixed with a conjugated polymer to form the active layer of the hybrid solar cell. Recently, a modification of this method was introduced, in which the ligand exchange was done in the solid state after the coating of the polymer/nanoparticle solution. This has the advantage that smaller ligands can be used, which positively influences

electron transport through the layer as well as the charge separation at the polymer/nanoparticle interface [101]. In the infiltration approach (ii) inorganic nanostructures are created on one electrode and are afterwards filled with the polymer phase. In the *in situ* approach (iii), the nanoparticles are directly prepared in the polymer matrix and are consequently ligand-free. The major advantage of this route, is that thereby the intrinsic challenges of ligand exchange are avoided [95]. Amongst the *in situ* routes metal xanthates turned out to be well suited precursors for the preparation of polymer/metal sulfide nanocomposites due to the fact that their solubility in organic solvents can be tailored by variation of the organic side groups. Usually they show good stability (also in solution) and the thermal conversion step to the corresponding metal sulfide proceeds at moderate temperatures (well below 200 °C), whereby only volatile byproducts are formed, which evolve from the hybrid layer at the applied temperatures [56]. Following this route, hybrid solar cells with different material combinations (polymer/CdS [55,103], polymer/CIS [56,104,105], small molecule/CIS [50], polymer/Sb<sub>2</sub>S<sub>3</sub> [106]) were already investigated and recently their application in hybrid tandem solar cells was also explored [107].

An important issue in organic and hybrid photovoltaics is also the processability of the solar cells on flexible polymer substrates, in particular on cheap and readily available poly(ethylene terephthalate) (PET) substrates. Only on flexible substrates all advantages of this emerging solar cell technology can be exploited, especially cheap production via high throughput roll-to-roll coating and printing technologies leading to unique light weight solar cell modules with a high flexibility in design, which will be important for many upcoming applications.

So far, the xanthate method uses conversion temperatures for the formation of the polymer/CIS layers typically of about 200 °C, e.g. polymer/CIS hybrid solar cells with PCEs up to 2.8% have been prepared using conversion temperatures of 195 to 210 °C [56,105]. This temperature range is far too high for processing on PET/ITO foil. For polymer/CdS systems, lower temperatures of approximately 160 °C have been used [103] but also 160 °C turned out to be problematic for PET/ITO. However, by applying lower annealing temperatures, a significant drop in PCE was observed in both cases. Also by applying higher temperatures the PCE decreased in a previous study using *in situ* prepared CIS nanoparticles [50]. The optimum annealing temperature for the respective hybrid material system seems to be a compromise between temperatures as high as possible to obtain well crystallized nanoparticles and temperatures as low as possible to avoid temperature induced degradation of the polymer phase, which would reduce the charge carrier mobility as well as the absorption properties of the polymer.

Bansal et al. [108] recently showed that the crystallinity of CdS can be improved by the addition of a small amount of n-hexylamine to the coating solution. In the case of P3HT/CdS nanocomposite films this improved crystallinity resulted in more efficient solar cells due to significantly higher short circuit currents in hybrid solar cells annealed at 160 °C.

As we assumed that in layers prepared at low annealing temperatures the crystallinity of the inorganic phase is most likely the limiting factor regarding charge generation in the absorber layers, we extend this method to polymer/CIS hybrids in order to reduce the processing temperature to a level which allows us to use PET foils as substrates. In addition, we explore the xanthate route toward the preparation of hybrid solar cell modules by demonstrating that polymer/metal xanthate precursor solutions can be

coated over larger areas using doctor blading as coating technique. The fulfillment of both issues, low temperature processing on PET substrates as well as the possibility of convenient large area coating, are crucial prerequisites for continuous roll-to-roll coating and processing on cheap and light-weight flexible substrates. A first assessment of the stability of the polymer/CIS hybrid solar cells is finally addressed by testing glass-glass encapsulated devices.

## 2 Experimental

### 2.1 Sample Preparation

PEDOT:PSS (Clevios P VP.AI 4083, Heraeus) was coated on glass/ITO substrates (Xin Yang Technology Ltd.,  $R_s = 10 \Omega/\text{sq}$ ), cleaned by sonication in isopropanol and  $\text{O}_2$  plasma etching (FEMTO, Diener electronic, 3 min) and thermally dried under nitrogen (150 °C, 15 min), or on PET/ITO sheets (Sigma-Aldrich, Co.,  $100 \Omega/\text{sq}$ , cleaning procedure as above) and dried at room temperature under nitrogen for 2 hours. Afterwards nanocomposite films were prepared by doctor blading of a chlorobenzene solution containing copper xanthates, indium xanthates (copper and indium O-2,2-dimethylpentan-3-yl dithiocarbonate; purchased from Aglycon, Austria; the chemical structures are depicted in the supporting information of this chapter, page 63, Figure 28) and PCDTBT (Poly[[9-(1-octylnonyl)-9H-carbazole-2,7-diyl]-2,5-thiophenediyl-2,1,3-benzothiadiazole-4,7-diyl-2,5-thiophenediyl], 1-Material, Chemscitech Inc., St. Laurent, Canada) at 40 °C. The concentration of PCDTBT in the precursor solution was 5 mg/mL, the weight ratio PCDTBT:CIS was 1:9 and the Cu:In molar ratio 1:1.7. For n-hexylamine (HA) modified samples, 4 wt% of HA were added to

the precursor solution. Subsequently, the precursor films were annealed for 30 minutes (except for the annealing duration test (Figure 29 on 64 - supporting information)) on a programmable heating plate (MCS 66, CAT Ingenieurbüro M. Zipperer GmbH). The heating temperature was varied as mentioned in the following and the heating rate was 11 °C/min. The thicknesses of the polymer/CIS absorber layers of the prepared solar cells were between 70 and 100 nm.

200 nm thick aluminum electrodes with a 2 nm (nominally) silver interlayer were deposited using a thermal evaporation chamber mounted inside a glovebox system (LABmaster dp, MBRAUN Glovebox Technology, Germany) at a base pressure of  $5 \times 10^{-6}$  to  $1 \times 10^{-5}$  mbar (nitrogen atmosphere) as reported elsewhere [104]. The substrates were not cooled during evaporation.

## 2.2 Characterization

I-V curves were recorded using a Keithley 2400 SourceMeter and custom-made LabVIEW software. The solar cells were illuminated using a Dedolight DLH400D (used in conjunction with Dedolight DEB400D electronic ballast). To obtain long term stability measurements the illumination was carried out by using a K.H. Steuernagel (KHS) SolarConstant 1200 solar simulation system. The intensity of the incoming light was set to  $100 \text{ mW cm}^{-2}$  providing a spectrum quite similar to AM1.5G (determined using a KippZonen-CMP-11 pyranometer, no spectral mismatch was considered) in both cases. The effective device area ( $0.04 \text{ cm}^2$ ) was defined by shadow masks applied to the solar cells. The aperture areas of the modules on glass were  $56.0 \text{ cm}^2$  (active area  $33.6 \text{ cm}^2$ ) and on polymer substrate  $12 \text{ cm}^2$  (active area  $7.2 \text{ cm}^2$ ).



External quantum efficiency (EQE) spectra were recorded using a monochromator MuLTImode4 equipped with a Xenon lamp provided by AMKO and a Keithley 2400 source meter.

The X-ray powder diffraction profiles were obtained on a Siemens D 501 diffractometer in Bragg-Brentano geometry operated at 40 kV and 30 mA, using Cu K<sub>α</sub> radiation ( $\lambda = 1.54178 \text{ \AA}$ ) and a graphite monochromator at the secondary side. The experimental line width was determined to be  $0.12^\circ$  at this  $2\theta$  position by measuring a Si reference standard (NIST 640c). TEM-BF and high resolution (HR)-TEM-BF analyses were conducted on a Tecnai F 20 microscope (FEI Company, 200 kV, Schottky emitter) equipped with an UltraScanCCD camera and an energy dispersive X-ray spectrometer.

UV-vis spectra were acquired using a Perkin Elmer Lambda 35 UV/Vis System. Layer thicknesses were specified on a DekTak XT surface profiler (Bruker).

High resolution mass spectra were recorded on a Waters GCT Premier equipped with electron impact ionisation (EI, 70 eV; pion source  $\approx 1.05 \times 10^{-6}$  mbar) and a direct insertion probe (DI). Powder from a freshly prepared precursor layer - which was obtained from a chlorobenzene solution of the metal xanthates, the polymer, and 4 wt% n-hexylamine - was placed into the direct insertion probe and rapidly transferred into vacuum. The acquisition of mass spectra (mass range: 50–800 Da; 1 spectrum/s) was started immediately after the transfer. Spectra were continuously acquired while the sample was heated from room temperature to  $250^\circ\text{C}$  (heating rate:  $10^\circ\text{C}/\text{min}$ ).

### 3 Results and Discussion

At low annealing temperatures the crystallinity of the inorganic phase is most likely the limiting factor regarding charge generation in the absorber layers. Inspired by the work of Bansal et al. [108] showing that by adding hexylamine the crystallinity of CdS nanoparticles were significantly improved using annealing temperatures of 160 °C, we investigated the influence of adding n-hexylamine (4 wt%) to the precursor solution on the characteristic parameters of the resulting PCDTBT/CIS hybrid solar cells annealed at different temperatures, namely 195 °C, 180 °C, 160 °C and 140 °C. The lowest temperature (140°C) is just about the onset temperature of the decomposition of a mixture of the metal xanthates [56] and therefore should be high enough to form CIS nanoparticles. However, it is rather unlikely that at this temperature a similar crystallinity as in the case of annealing at 195 °C is obtained. As it can be seen in Table 1, in the absence of n-hexylamine PCDTBT/CIS solar cells reach their best efficiencies at an annealing temperature of 195 °C, which corresponds to the results of previous studies [50,56].

However, in the presence of n-hexylamine the maximum is shifted to 180 °C. Also at 140 °C and 160 °C the performance of the n-hexylamine-modified solar cells is significantly higher than of solar cells prepared at any temperature without the addition of n-hexylamine.

All the solar cells prepared at the different temperatures were annealed for 30 min (heating rate: 11 °C/min), an annealing procedure which turned out to be best for the preparation of hybrid polymer/CIS solar cells at a temperature of 195 °C in earlier studies [56]. To verify the influence of the duration at low temperature annealing (140 °C) on hybrid solar cells prepared with n-hexylamine, the annealing time was varied from 30 to 75

minutes. This turned out to be not crucial for the solar cell performance as there was no significant difference detected (detailed results can be found in the supporting information of this chapter, page 64, Figure 29). Keeping in mind, that a shorter annealing time is more suitable for an industrial process and of course energy saving, all the cells were annealed for 30 minutes.

<b>Composition</b>	<b>V<sub>oc</sub> / mV</b>	<b>I<sub>sc</sub> / mA/cm<sup>2</sup></b>	<b>FF / %</b>	<b>PCE / %</b>
<b>At 140 °C</b>				
PCDTBT/CIS	344 ± 9	9.60 ± 0.26	41.6 ± 0.4	1.37 ± 0.01
PCDTBT/CIS:HA	515 ± 22	9.40 ± 0.33	48.8 ± 2.0	2.36 ± 0.02
<b>At 160 °C</b>				
PCDTBT/CIS	332 ± 12	9.46 ± 0.24	41.4 ± 1.0	1.30 ± 0.01
PCDTBT/CIS:HA	487 ± 16	9.53 ± 0.43	47.9 ± 0.8	2.22 ± 0.02
<b>At 180 °C</b>				
PCDTBT/CIS	419 ± 8	10.07 ± 0.44	44.2 ± 0.8	1.86 ± 0.04
PCDTBT/CIS:HA	501 ± 8	9.71 ± 0.09	50.5 ± 0.6	2.45 ± 0.05
<b>At 195 °C</b>				
PCDTBT/CIS	447 ± 27	9.58 ± 0.52	46.8 ± 0.9	2.00 ± 0.02
PCDTBT/CIS:HA	479 ± 23	9.18 ± 0.88	48.1 ± 2.5	2.10 ± 0.03

**Table 1: Influence of n-hexylamine on the performance of PCDTBT/CIS solar cells at different annealing temperatures (mean values of each best ten cells are given).**

At 195 °C the devices prepared with and without n-hexylamine do not show a significant difference in the PCE (2.00% and 2.10% respectively).

However, these values are significantly lower than those of devices prepared with n-hexylamine at 180 °C (2.45%). Figure 19 shows the impact of the addition of n-hexylamine on the I-V curves of PCDTBT/CIS solar cells, which were annealed at 140 °C and at 195 °C.

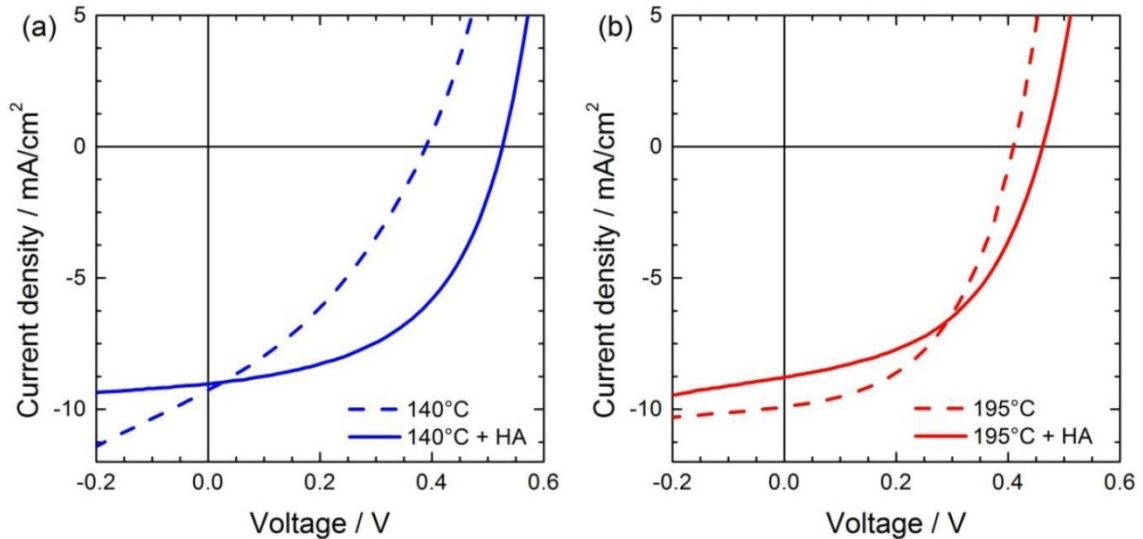
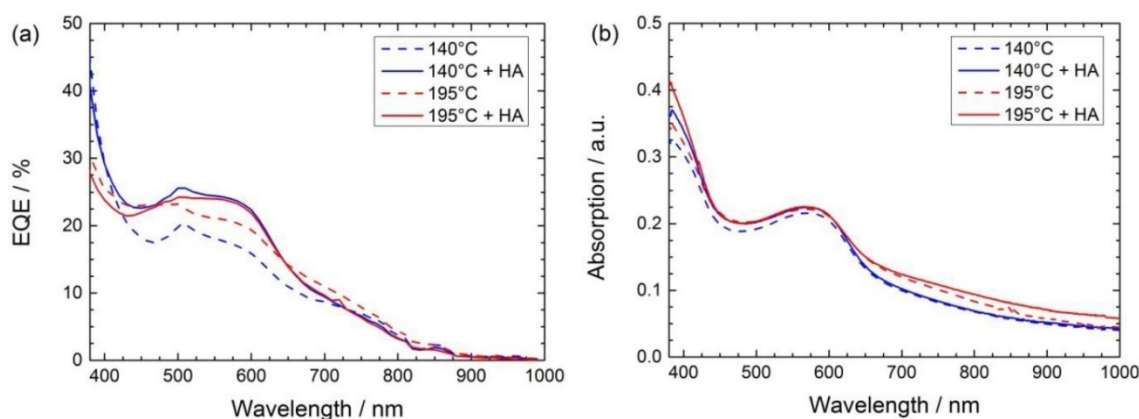


**Figure 19: I-V curves under illumination (100 mW/cm<sup>2</sup>) of PCDTBT/CIS solar cells prepared at annealing temperatures of (a) 140 °C and (b) 195 °C with and without hexylamine (Ref. [85]).**

As we can see from Figure 19 and, in particular, from Table 1, the presence of n-hexylamine significantly improves the open circuit voltage and the fill factor at any temperature. At 140 °C the  $V_{oc}$  is increased by more than 170 mV and the fill factor rises from 41.6% to 48.8%, whereas the short circuit current nearly stays the same. At 195 °C the hybrid solar cell prepared with n-hexylamine shows only a slight improvement in fill factor (+1.3%) and  $V_{oc}$  (+30 mV); an advantage which is nearly canceled by a lower  $I_{sc}$  (-0.4 mA/cm<sup>2</sup>). The short circuit current, in general, tends to be slightly lower for the samples containing n-hexylamine, which we would not have expected based on the study by Bansal et al. [108] where primarily the  $I_{sc}$  was improved in the P3HT/CdS hybrid solar cells

prepared upon addition of n-hexylamine to the precursor solution. These different observations could stem from the fact that the material combinations PCDTBT/CIS and P3HT/CdS are quite diverse. In particular, the morphology of the absorber layer of both systems is quite different. In the case of P3HT/CdS the CdS nanocrystals in the P3HT matrix tend to agglomerate to bigger units [109], while usually in polymer/CIS layers agglomeration is not that pronounced and the nanoparticles seem to be more homogeneously distributed in the polymer matrix [56,110], which could lead to the fact that the addition of n-hexylamine is influencing different parameters.

For further studies of the influence of n-hexylamine on the PCDTBT/CIS absorber layer, the solar cells and absorber layers prepared at 140 and 195 °C were investigated in more detail.



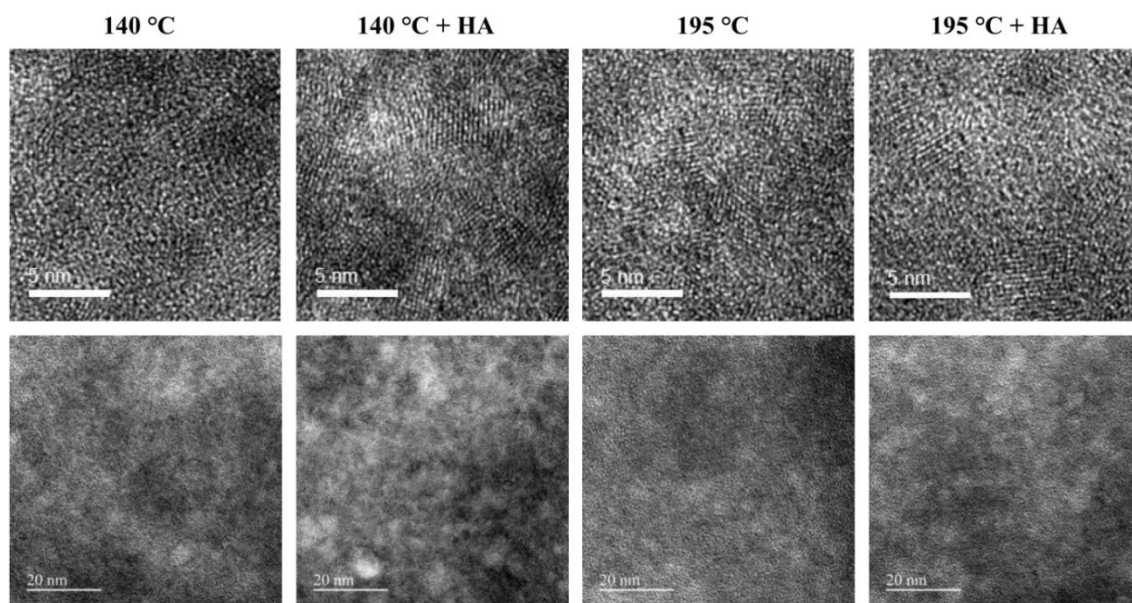
**Figure 20: (a) EQE spectra of the hybrid solar cells prepared in presence and absence of n-hexylamine at 140 °C and 195 °C in comparison to (b) the absorption spectra of the respective nanocomposite layer (Ref. [85]).**

Figure 20 shows the external quantum efficiencies of the PCDTBT/CIS hybrid solar cells and the absorption of the respective nanocomposite layers. In the regions of the spectra, where the nanocomposite layers show

maximum absorption, the respective solar cells show the highest EQE values. The only significant difference in the EQE, which should be mentioned, can be found in the wavelength range between 500 and 600 nm, at the main absorption maximum of the polymer PCDTBT. The charge generation in the devices prepared with n-hexylamine is slightly improved in this region compared to the devices without n-hexylamine. However, the differences in the absorption spectra are negligible and the higher charge generation efficiency is unlikely from a higher crystallinity of the polymer phase.

The phase separation, morphology, particle size, and size distribution of PCDTBT/CIS films were investigated by TEM-BF. The TEM-BF micrographs are depicted in Figure 21. The images show quite even distributed nanoparticles (dark regions) and polymer phases. In contrast to our earlier work with PCDTBT (Ref. [105]), we have not observed agglomerates of the polymer phase which can be explained by the higher molecular mass and therewith lower mobility/viscosity of the used PCDTBT in this study. A lower viscosity of the polymer phase during the conversion at the lower temperature probably prevents or at least retards larger phase separation. In the TEM-BF images, the single nanoparticles and thus their size and size distribution are not determinable because of the high nanoparticle loading in the films (neither in the HR-TEM-BF images in the first row, nor in the TEM-BF images in the second row). Furthermore, also no other differences in phase separation are visible. However, paying attention on the lattice fringes of the CIS nanoparticles in the HR-TEM-BF images, the n-hexylamine containing sample prepared at 140 °C is more similar to both samples prepared at 195 °C, where the lattice fringes of the CIS nanoparticles are more clearly visible as in the sample prepared without n-hexylamine at 140 °C. This observation

indicates that the addition of n-hexylamine leads to higher crystallinity of the nanoparticles, in particular at lower temperatures.



**Figure 21: Transmission electron microscopy images of PCDTBT/CIS nanocomposite layers prepared at 140 °C and 195 °C (Ref. [85]).**

To exclude an influence of varying Cu/In ratio on the performance of the devices prepared with and without addition of n-hexylamine, EDX analyses were made of these films. The measurements revealed that the CIS nanoparticles in all 4 samples have the same Cu/In ratio, which is approximately 1/1.8. This is, keeping the uncertainties of EDX measurements in mind, in line with the Cu/In ratio of 1:1.7 in the precursor solutions. This excess of indium has been shown to be beneficial for the efficiency of this type of solar cells [51,56].

Additionally, X-ray diffraction investigations were carried out on PCDTBT/CIS samples (for sample preparation see experimental section). In Figure 22 the diffraction patterns of the samples with/without n-hexylamine annealed at 140 °C and 195 °C, respectively, are presented. The main diffraction peaks at 27.9°, 46.3° and 55.0° 2 $\theta$  as well as the

smaller peak at  $74.6^\circ 2\theta$  of all samples match well with the reference data for CIS. Although, the reference data include a small peak at  $17.9^\circ 2\theta$ , the peak detected in this  $2\theta$  range cannot be unambiguously attributed to CIS, as PCDTBT also exhibits a diffraction peak at that angle [105]. Whereas the primary crystallite size in the samples at  $195^\circ\text{C}$  is approximately 2.5 nm for both samples as estimated by the Scherrer equation, a distinct difference in the primary crystallite size is observed in the materials prepared at  $140^\circ\text{C}$ . The broadening of the reflexes is much more pronounced for the sample prepared without n-hexylamine indicating a smaller crystallite size or a lower crystallinity of the material. The value for the sample prepared with n-hexylamine is approx. 2.4 nm and, thus, almost the same as in the samples annealed at higher temperatures but much higher than the primary crystallite size of the sample without n-hexylamine having an estimated value of 2.0 nm. The results of the X-ray diffraction experiments corroborates the assumption that n-hexylamine increases the crystallinity of the CIS nanoparticles at lower temperatures.



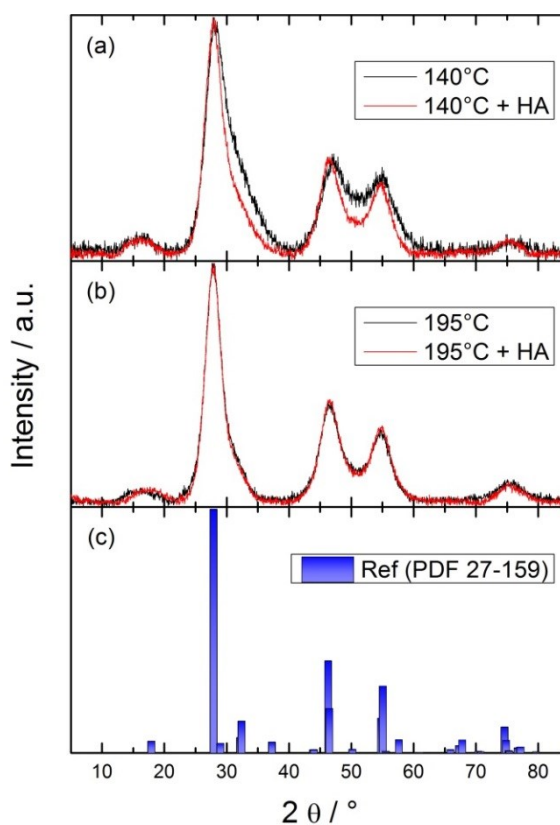


**Figure 22: X-ray diffraction measurements showing the influence of n-hexylamine during the thin film preparation on the crystallinity of the nanocomposite films as a function of the annealing temperature; (a) 140 °C, (b) 195 °C; (c) reference pattern for CuInS<sub>2</sub> (PDF-27-159) (Ref. [85]).**

To investigate the influence of n-hexylamine on the CIS formation process a thermogravimetric analysis was done. Figure 23 shows the mass loss of the precursor material (metal xanthate and PCDTBT) with and without n-hexylamine.

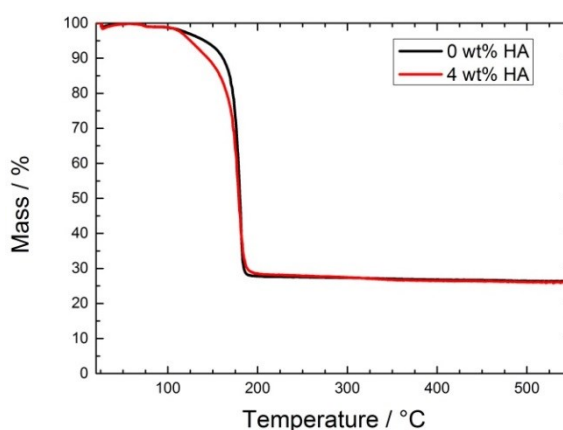


**Figure 23: Thermogravimetric analysis of PCDTBT/CIS precursor material with and without n-hexylamine (Ref. [85]).**

Both samples showed rather comparable mass loss. Keeping the typical accuracy of the used equipment in mind (approx. 1-3%), it is practically not possible to answer, whether n-hexylamine already evaporates during the drying process, if it remains in the films without any reaction, or if it participates in a chemical reaction. Nevertheless, the precursor mixture without n-hexylamine exhibits a single step conversion of the metal xanthates to CIS, having its onset (mass loss of 5 wt%) at 141 °C, whereas the n-hexylamine modified sample shows a slightly earlier onset at already 125 °C. The presence of n-hexylamine obviously reduces the onset temperature of the decomposition of the metal xanthates, what finally might be the reason of enhanced formation and thus crystallization of CIS at lower temperatures.

The thermal decomposition of the xanthates in the presence of n-hexylamine was also investigated by means of high resolution mass spectrometry (HRMS) on an instrument equipped with DI-EI. During this investigation, a powder taken from a freshly prepared precursor layer (copper/indium xanthates, PCDTBT, 4 wt% n-hexylamine) was heated from

room temperature to 250 °C. Products evaporating from the DI were continuously monitored by acquisition of EI mass spectra.

First of all, it is important to note, that no residual n-hexylamine was observed. Loss due to evaporation during transfer of the sample into the vacuum is excluded, since comparable amounts of the amine were detectable without any problems in the course of analogous experiments with pure n-hexylamine.

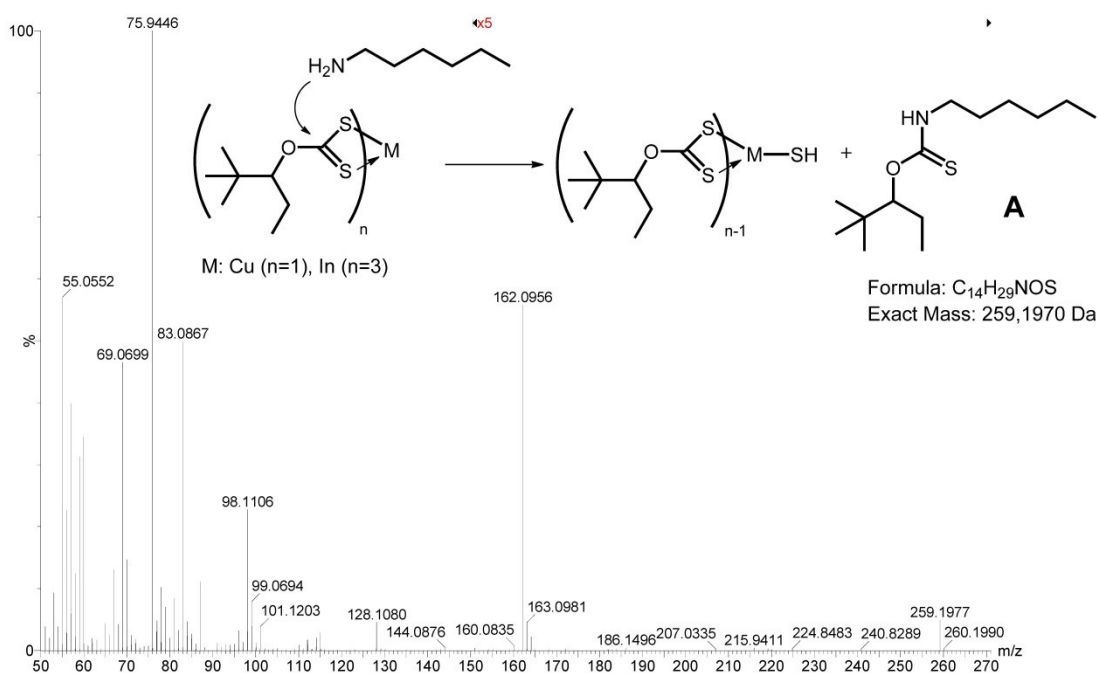


**Figure 24: High resolution mass spectrum (EI-DI) acquired during the thermal decomposition of the precursor material with n-hexylamine at a temperature of the DI probe of approx. 115 °C (Ref. [85]).**

The most important result of the investigation by MS is reproduced in Figure 24 which shows the spectrum obtained at a temperature of the DI probe of approximately 115 °C. In comparison to data obtained for samples prepared without n-hexylamine, significant additional peaks were observed at  $m/z = 259.1977$ , 162.0956 Da, and 128.1080 Da, respectively. The first peak corresponds well to the exact mass calculated for the monoisotopic

peak of the molecular ion of O-2,2-dimethylpentan-3-yl-N-hexylthiocarbamate A (compare Figure 6). The other signals are assigned to corresponding fragment ions with the formula  $C_7H_{16}NOS$  ( $m/z_{calc} = 162.0953$  Da), and  $C_7H_{14}NO$  ( $m/z_{calc} = 128.1075$  Da), respectively. EI reference spectra of thiocarbamate A are yet not available. But it is important to note, that the observed fragmentation is in line with the fragmentation observed for other dialkylthiocarbamates (e.g. NIST EI spectrum of O-isopropyl N-ethylthiocarbamate). Thus, both the exact mass data as well as the fragmentation indicates the formation of thiocarbamate A. A possible mechanism is the reaction of the metal xanthates with n-hexylamine as illustrated in Figure 24. Since no residual amine was detected by HRMS, it is suggested that i) the reaction occurs already in solution and/or during the drying step, and that ii) unreacted amine evaporates together with the chlorobenzene. To our knowledge, these are the first results indicating the formation of dialkylthiocarbamates by reaction of metal xanthates with amines. But it has to be mentioned that analogous reactions of dialkylxanthates with amines are well known [111]. Consequently, it is suggested, that the addition of n-hexylamine enables alternative routes for the thermal decomposition with reduced onset temperatures due to the reaction discussed above. However, within this work only a deficit of n-hexylamine was used, since higher amounts of n-hexylamine did not lead to enhanced performances of the solar cells up to now. Thus, a large part of the metal xanthate groups still has to react via the Chugaev elimination. This was also confirmed by HRMS, corresponding reaction products (i.e. COS, 4,4-dimethyl-2-pentene) were monitored at increased temperature of the DI probe. Note, that these results can be used to explain the differences observed during thermogravimetric analysis (Figure 23).

Additionally, these findings also strongly suggest that similar chemical reactions could take place in the work of Bansal et al. using cadmium ethyl xanthate and n-hexylamine [108] and in the work of Kharkwal et al. using a mixture of copper indium ethylxanthates and n-butylamine [112].

### 3.1 Flexible Hybrid Solar Cells

As shown in Table 1, by using n-hexylamine as additive, the annealing temperature can be decreased to 140 °C without having losses in PCE compared to a device prepared at 195 °C without n-hexylamine. Even more astonishing, the PCE is even about 18% higher. This is a good precondition to produce efficient hybrid solar cells also on flexible substrates, due to the fact that a process temperature of 140 °C is compatible with the use of flexible PET/ITO substrates. Therefore, hybrid solar cells on a PET/ITO foil were prepared using the same coating methods as for the glass/ITO substrates (spin coating for the PEDOT:PSS layer; doctor blading for the PCDTBT/CIS absorber layer).

A photograph of a flexible hybrid polymer/CIS solar cell as well as the I-V curves measured in the dark and under illumination (100 mW/cm<sup>2</sup>) is presented in Figure 25. The flexible device exhibits a PCE of about 1.6%, which is a bit lower than for the similarly processed device on glass substrates and may be attributed to the higher sheet resistance of the PET/ITO substrate (100 ohm/sq) compared to the glass/ITO substrates (10 ohm/sq). In any case, this example demonstrates the good suitability of the n-hexylamine modified xanthate route for the fabrication of flexible hybrid solar cells.

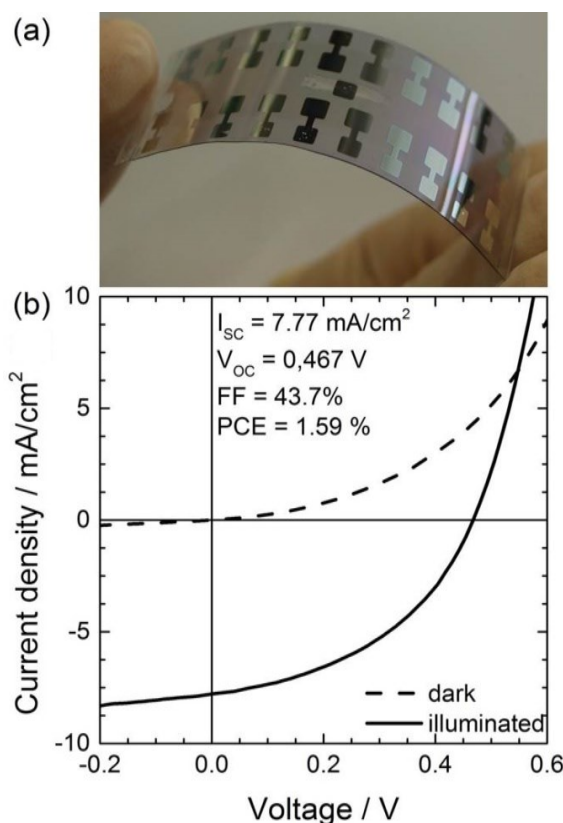


**Figure 25: I-V curves of a flexible PCDTBT/CIS:HA hybrid solar cell (Ref. [85]).**

### 3.2 Hybrid Solar Cell Modules

The xanthate route leads to smooth, non-porous and homogeneous polymer/CIS layers over larger areas using doctor blading, despite the fact that a large quantity of organic compounds evaporates during the decomposition process of the metal xanthate. Thus, in the next step we demonstrated the suitability of this process for homogeneous coating of larger areas (8 x 8 cm<sup>2</sup>) and the series connection of several stripe-shaped (7 x 0.6 cm<sup>2</sup>) solar cells to a hybrid solar cell module (Figure 26(a)). The size of the module is thereby limited by the size of our laboratory coating systems. The doctor blading of the PCDTBT/metal xanthate solution can be done without problems on a glass/ITO substrate also in larger area and the prepared films of about 8 x 8 cm<sup>2</sup> showed a high homogeneity and

smoothness. Thus, it was possible to realize a hybrid solar cell module consisting of eight single cells, 4.2 cm<sup>2</sup> each, leading to an overall active area of 33.6 cm<sup>2</sup> by an aperture area of 56.0 cm<sup>2</sup> (details on the geometry of the module are given in the supporting information, page 65, Figure 30). The conversion of the precursor layer to the polymer/metal sulfide absorber layer was also in this case done at 140 °C and in the presence of n-hexylamine. The I-V characteristics of such a hybrid solar cell module are shown in Figure 26(b). The module has an I<sub>SC</sub> of 26.9 mA and a V<sub>OC</sub> of 3.6 V. Considering the 8-fold series connection. This corresponds to a V<sub>OC</sub> of 450 mV per single cell. The FF of the module is about 34%. This leads to a power conversion efficiency of 1% considering only the active area and to an efficiency of 0.6% taking the total aperture area into account. This rather large difference is mainly because of the fact that the focus was not set on keeping the dead areas as small as possible but in demonstrating that hybrid solar cell modules with reasonably big areas can be prepared via the xanthate route.

Homogeneous coating of larger areas of thin PET/ITO foils by the available doctor blading set-up (without vacuum plate) was challenging as it is difficult to place the foil completely flat, which is essential to obtain a homogeneous layer thickness. However, we were able to fabricate a small flexible hybrid solar cell module with an overall active area of 7.2 cm<sup>2</sup> (aperture area 12 cm<sup>2</sup>), which consists of eight single cells, 0.9 cm<sup>2</sup> each (Figure 26(c), for details concerning module geometry see supporting information, page 65, Figure 30). The conversion of the n-hexylamine doped PCDTBT/metal xanthate precursor solution was carried out at 140 °C. The I-V characteristics of the flexible hybrid solar cell module (Figure 26(d)) exhibit an I<sub>SC</sub> of 2.7 mA and a V<sub>OC</sub> of 3.15 V. The FF of the module is about 27% giving an overall power conversion efficiency of 0.32%

for the active area (0.2% for the aperture area). This lower values can be explained by the higher sheet resistance of the PET/ITO foils (vide supra) but mainly with the not optimum coating process of the flexible foil with the used laboratory doctor blading setup. Thus, we are convinced that a more homogeneous coating of PET/ITO foils is achievable with more suited techniques such as slot die coating in a roll-to-roll equipment, which would lead to not only larger but also more efficient flexible hybrid solar cell modules produced via the xanthate route.

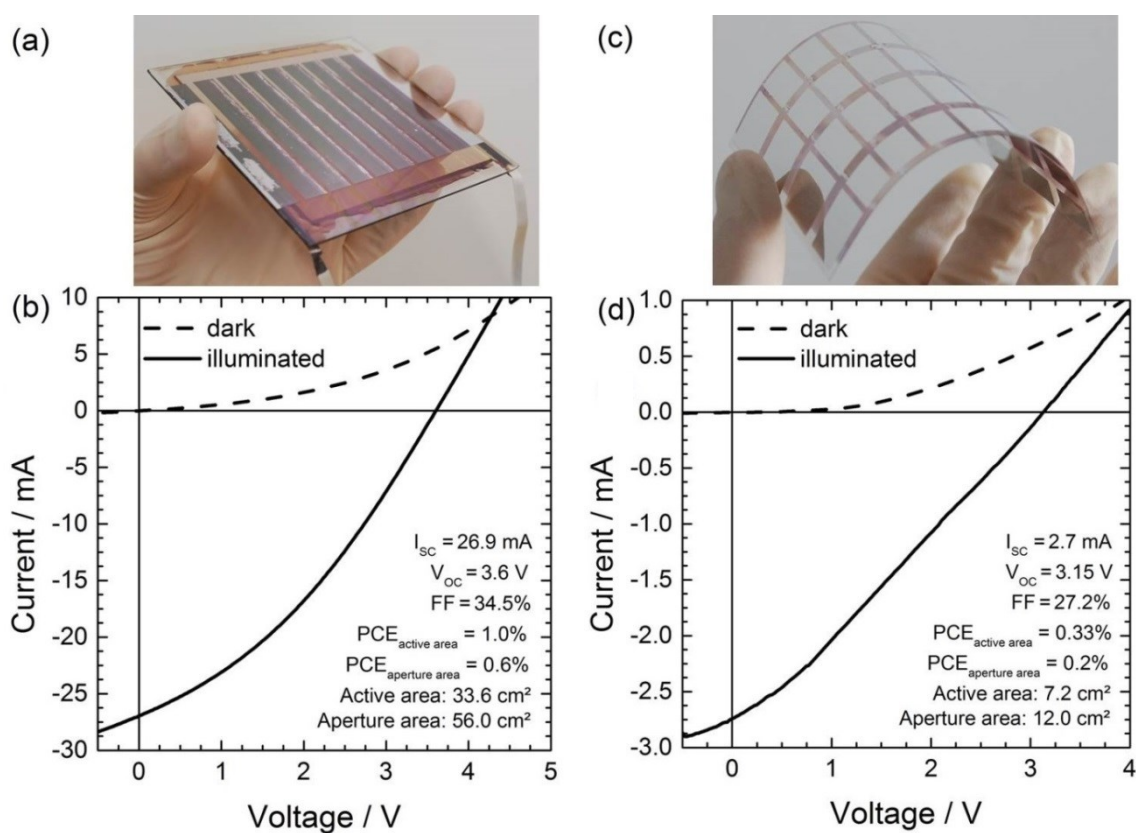


**Figure 26:** (a) Picture of a PCDTBT/CIS:HA hybrid solar cell module on a glass/ITO substrate and (b) the corresponding I-V curves. (c) Picture of a flexible PCDTBT/CIS:HA hybrid solar cell module on a PET/ITO substrate and (d) the corresponding I-V curves (Ref. [85]).



### 3.3 Stability

A first investigation of the stability of the prepared solar cells was started, as besides PCE this is a further very important property of solar cells, which is often not addressed in publications concerning hybrid solar cells and only a few studies contain detailed stability data (see for examples refs. [51,113–117]). As in all other polymer-based PV technologies the hybrid solar cells have to be protected towards moisture and oxygen using suitable encapsulation materials [113,118]. However, if so, such devices reveal already promising life time [119]. In our first tests, n-hexylamine containing PCDTBT/CIS solar cells were encapsulated with glass using epoxy glue. Figure 27 summarizes the characteristic parameters of two devices (prepared at 140 °C and 195 °C) measured every 30 min over 1000 hours under continuous illumination by a KHS SolarConstant 1200 solar simulator using an automated measuring setup. After encapsulation, both samples had a PCE of around 2% at the beginning of the measurements.

The results of this long term stability study show that the sample, which was annealed at 195 °C exhibits a very heavy burn in phase which drops its PCE down to 50% of the starting value within the very first hours. In the following, the degradation slowed down but still was quite strong, which led to a decrease of 80% in PCE after 400 hours and to a total degradation of the solar cell after 1000 hours.

In contrast to that, the PCDTBT/CIS hybrid solar cell annealed at 140 °C is much more stable. After a continuous illumination of 1000 hours the solar cell exhibits still more than 60% of the initial PCE. At the beginning of the stability test, the drop in efficiency is mainly due to the decrease of the  $I_{SC}$  in the first 50 hours. After a burn in phase the  $I_{SC}$  stays constant for the whole study. For the  $V_{OC}$  barely any loss can be detected, while the fill factor even increases slightly in the first 100 hours before a slight decrease

can be observed. Nevertheless, even after 400 hours the FF retains 96% of its initial value. From then on the FF is the main parameter causing the further moderate but steady loss in PCE. These tests are still ongoing.

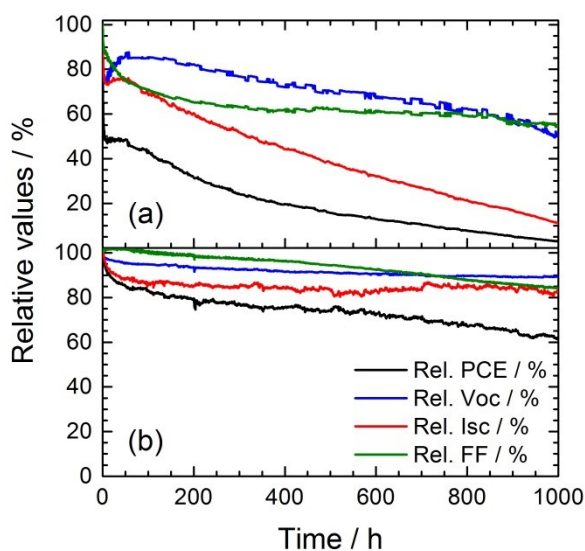


**Figure 27: Comparison of the stability of PCDTBT/CIS nanocomposite solar cells prepared with n-hexylamine annealed at (a) 195 °C and at (b) 140 °C (Ref. [85]).**

## 4 Conclusions

The addition of a small amount of n-hexylamine to the polymer/metal xanthate precursor solution, increases the crystallinity of the CIS nanoparticles at low annealing temperatures (140 °C), while at higher temperatures (195 °C) no significant further improvement of the crystallinity of the CIS phase can be detected. This effect is also reflected in the performance of the prepared hybrid solar cells. For devices annealed at 195 °C, hardly any difference is observable regarding PCE. However, by lowering the annealing temperature for the absorber layer of the devices to 180, 160 and 140 °C the difference becomes more and more significant and at 140 °C the PCE of the devices is almost doubled by the modification with

n-hexylamine. N-hexylamine thereby initiates the decomposition of the metal xanthates at lower temperatures by reacting with them to give the corresponding dialkylcarbamate and thus facilitates the nucleation and crystallization at lower temperatures. However, the major part of the metal xanthates still decomposes via the Chugaev elimination as only a sub-stoichiometric amount of n-hexylamine was used.

By using this low temperature method, we were able to prepare hybrid solar cells on flexible PET foils, which show typical PCEs of 1.6%. Moreover, we showed that the precursor solutions used in the metal xanthate route can be coated very homogeneously also over larger substrate areas. After the thermal conversion of the precursors to the polymer/CIS hybrid layer, the film still retains homogeneous and smooth. This enabled us to fabricate first hybrid solar cell modules on glass and also on flexible substrates with aperture areas up to 56 cm<sup>2</sup>.

Also the lifetime of the devices prepared at low temperatures is very promising. Even though, using aluminum electrodes, glass-glass encapsulated devices prepared at 140 °C show good stability during continuous illumination over 1000 hours. In the hybrid solar cells prepared at 140 °C, after 1000 hours testing, more than 60% of their initial PCE is retained, while the solar cells prepared at 195°C are completely degraded after this testing period. By using metal oxide interlayers or, e.g. silver electrodes, the lifetime of the hybrid solar cells might be further improved.

## 5 Acknowledgement

Financial support by the Christian Doppler Research Association, the Austrian Federal Ministry of Economy, Family and Youth (BMWFJ), and

ISOVOLTAIC AG is gratefully acknowledged. Furthermore, we would like to thank Christine Bandl, Josefine Hobisch and Lukas Troi for their contributions to this work.

## 6 Supporting Information

### 6.1 Structures of the Used Materials

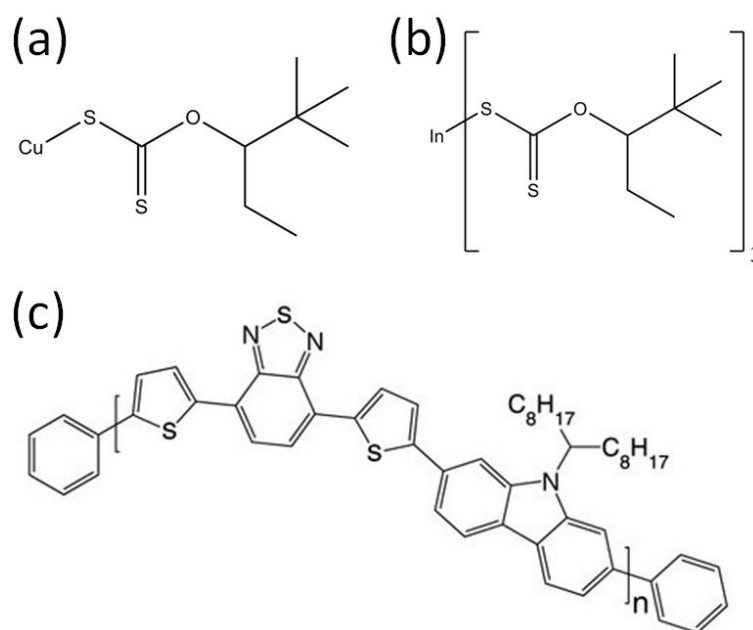


**Figure 28: Chemical structures of**

- (a) copper O-2,2-dimethylpentan-3-yl dithiocarbonate,**
- (b) indium O-2,2-dimethylpentan-3-yl dithiocarbonate and**
- (c) PCDTBT (Ref. [85]).**

## 6.2 Variation of the Annealing Duration

The influence of the annealing time on low temperature annealed (140 °C) PCDTBT/CIS:HA solar cells was verified.

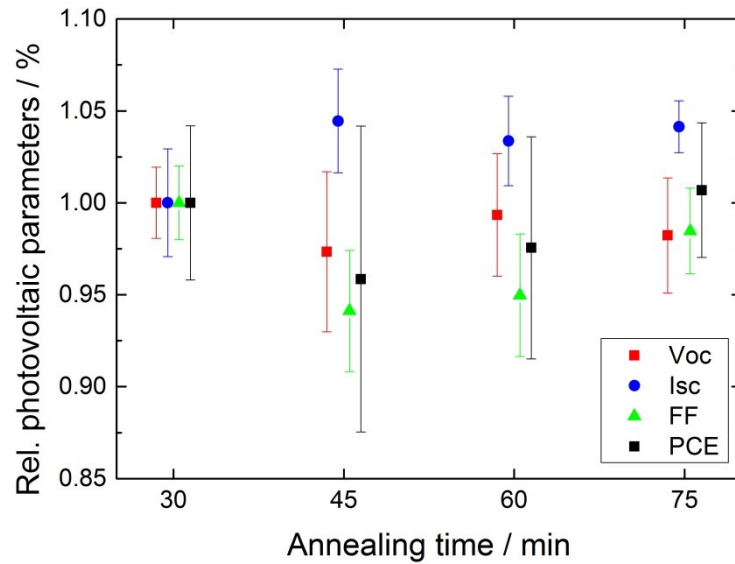


**Figure 29: Dependency of the characteristic solar cell parameters of low temperature annealed (140 °C) PCDTBT/CIS:HA solar cells on the annealing time. The average values of 10 cells are depicted. No significant difference could be detected (Ref. [85]).**

### 6.3 Geometries of the Hybrid Solar Cell Modules

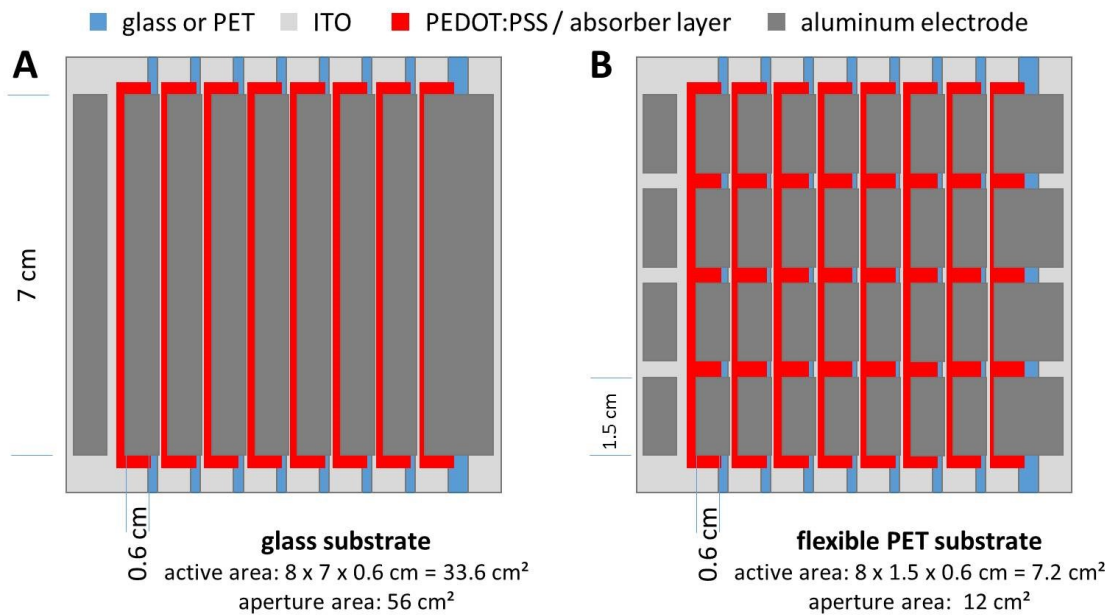


**Figure 30: Geometries of the prepared hybrid solar cell modules on glass (A) and on flexible PET substrates (B) (Ref. [85]).**

## **CHAPTER IV**

### **FURTHER INVESTIGATIONS ON THE INFLUENCE OF N-HEXYLAMINE**

## 1 Introduction

The results that are presented in this section give further information on the effect of the addition of n-hexylamine, but were not included in the scientific article, which is reproduced in chapter III of this thesis [85]. These further investigations give a deeper insight into the chemical processes, which appear to happen by adding n-hexylamine to the copper indium sulfide precursor solution. The results have not yet been published.

## 2 Influence on the System PSiF-DBT/CIS

The best efficiencies for hybrid polymer/CIS solar cells synthesized via the xanthate route were achieved by using poly[(2,7-silafluorene)-alt-(4,7-di-2-thienyl-2,1,3-benzothiadiazole)] (PSiF-DBT, chemical structure is depicted in Figure 31) as organic donor [56].

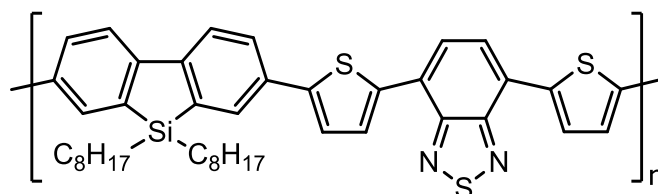


**Figure 31: Chemical structure of the conjugated Polymer PSiF-DBT**

Therefore, the effect of n-hexylamine on the performance of PSiF-DBT/CIS solar cells at different temperatures was also investigated (Table 2). These experiments confirm that n-hexylamine has a positive impact, although the results exhibit a trend, which is slightly different to the results for PCDTBT/CIS.



<b>Composition</b>	<b>V<sub>oc</sub> / mV</b>	<b>I<sub>sc</sub> / mA/cm<sup>2</sup></b>	<b>FF / %</b>	<b>PCE / %</b>
<b>At 140 °C</b>				
PSiF-DBT/CIS	481 ± 11	6.06 ± 0.14	39.1 ± 0.5	1.12 ± 0.02
PSiF-DBT /CIS:HA	533 ± 10	6.68 ± 0.23	41.5 ± 0.7	1.46 ± 0.04
<b>At 160 °C</b>				
PSiF-DBT /CIS	456 ± 18	6.50 ± 0.20	44.2 ± 0.7	1.30 ± 0.03
PSiF-DBT /CIS:HA	546 ± 20	7.41 ± 0.11	44.5 ± 1.7	1.80 ± 0.06
<b>At 180 °C</b>				
PSiF-DBT /CIS	443 ± 16	7.91 ± 0.33	41.3 ± 0.8	1.43 ± 0.04
PSiF-DBT /CIS:HA	506 ± 8	7.80 ± 0.27	38.7 ± 0.8	1.51 ± 0.03
<b>At 195 °C</b>				
PSiF-DBT /CIS	462 ± 10	8.32 ± 0.32	43.8 ± 0.7	1.66 ± 0.06
PSiF-DBT /CIS:HA	520 ± 10	8.76 ± 0.37	49.3 ± 0.5	2.22 ± 0.15

**Table 2: Influence of n-hexylamine on the performance of PSiFDBT/CIS solar cells at different annealing temperatures (mean values of each best ten cells are given).**

Analogical to the presented results for PCDTBT/CIS solar cells, the addition of n-hexylamine led to significantly higher  $V_{oc}$  values (+11% to +20%) at all temperatures. At 140 °C, 160 °C and 195 °C the n-hexylamine doped solar cells show an increase in fill factor and surprisingly also a slight improvement of  $I_{sc}$ , which was not the case for PCDTBT/CIS, where the current density even dropped a bit. However, the increase in fill factor was weaker in the case of PSiF-DBT/CIS, except for 195 °C, where also the efficiency increase is surprisingly high (+34%). This might be attributed to

the performance of the sample without n-hexylamine at this temperature, which was not as good as expected. 195 °C and no additive represent standard preparation conditions for this system at our working group for already quite some time. Naturally, the performance is not always the same and somewhat fluctuating, but in general for these conditions values in the range of 2% represent the mean efficiencies of all solar cells that were fabricated during the 3-year period of this thesis. At this stage, it also has to be noted that the slight differences between the two hybrid systems might have occurred due to the differing scope of work. These experiments were executed just once to prove the effect for this system, while the primary experiments for PCDTBT/CIS were much more comprehensive. This might also be the reason that the samples at 180 °C somehow not in line with the other data. It is believed, that further experiments at this temperature would confirm the effect of n-hexylamine. Typical I-V curves of low- and standard-temperature annealed (140 °C and 195 °C) hybrid PSiF-DBT/CIS solar cells in the presence and in the absence of n-hexylamine are depicted in Figure 32.

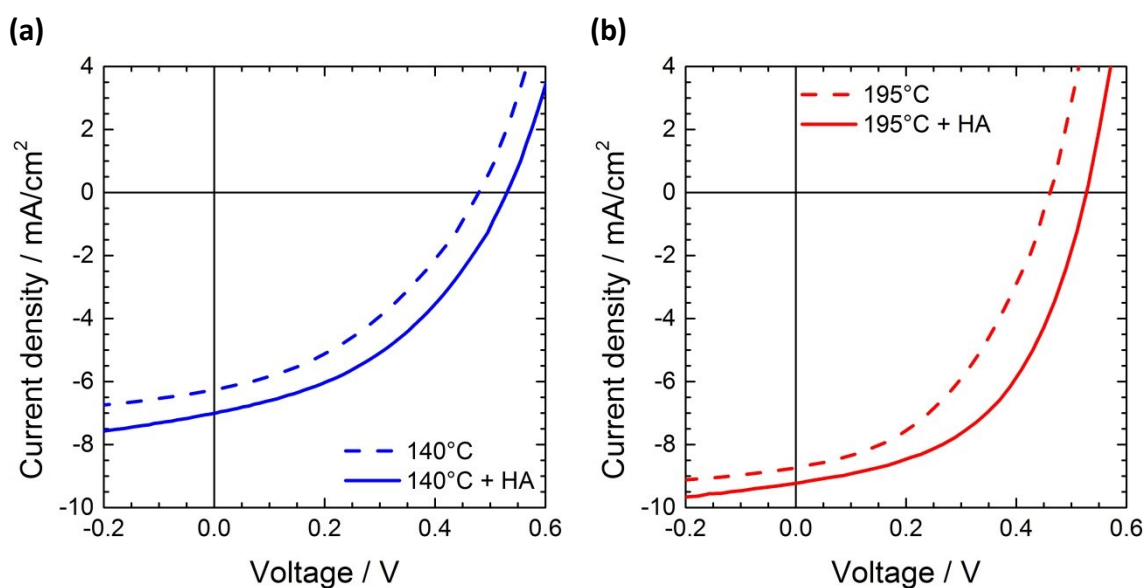


**Figure 32: I-V curves of PSiF-DBT/CIS solar cells prepared at (a) 140 °C and (b) 195 °C with and without hexylamine.**

To sum up, at 140 °C, 160 °C and 195 °C the presence of n-hexylamine resulted in a significant performance improvement of 30%, 38% and 34%. These results definitely corroborate the positive influence of n-hexylamine on the crystallinity of the copper indium sulfide nanocrystals in polymer/CIS hybrid solar cells, which has been extensively discussed and investigated above. It was decided to forego further layer investigations like they were done for PCDTBT/CIS. The fact that the addition of n-hexylamine had the same effect on a second hybrid system, using a different polymer, confirms that it influences thermal composition of the inorganic part.

### 3 Vanadium Oxide as Anode Buffer Layer

Poly(3,4-ethylenedioxythiophene) (PEDOT) is commonly used as anode buffer layer in organic and hybrid photovoltaics. It is a high conductive ( $\sim 300$  S/cm) polymer, which is positively charged but unfortunately hardly soluble in any common solvent [120]. This problem is solved by using poly(styrene sulfonic acid) (PSS), which is a negatively charged water-soluble polyelectrolyte, as charge-balancing dopant [120]. The combination PEDOT:PSS (for the chemical structure see Figure 33) is a still highly conductive (10 S/cm), water-soluble polyelectrolyte system, which exhibits good layer forming properties, good stability and a high visible light transmittance [120]. It is usually applied on top of the ITO electrode and thereby also improves the surface roughness [121].

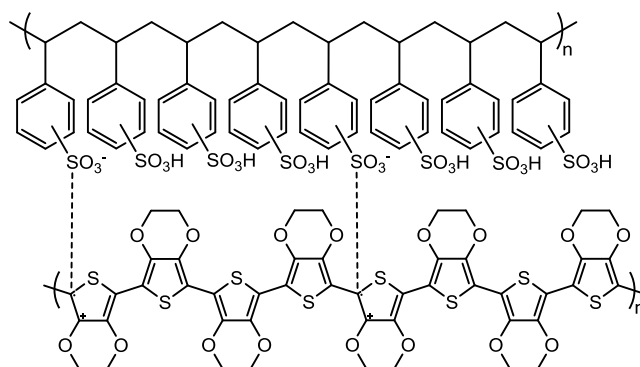


**Figure 33: Chemical Structure of PEDOT:PSS**

So far PEDOT:PSS was used as interlayer in all hybrid polymer/CIS solar cells, which were fabricated to investigate the effect of n-hexylamine. To exclude the possibility that the reason for the shown effect is any interaction between the amino group of the additive and the poly(styrene sulfonic acid), PEDOT:PSS was replaced. Beside PEDOT:PSS, inorganic materials, particularly vanadium oxide ( $\text{V}_2\text{O}_5$ ), are extensively used as anode buffer layers (ABL), due to their hole extraction properties

[122–125]. Thus  $V_2O_5$  was used as ABL for one experiment. The results are given in Table 3.

<b>Composition</b>	<b><math>V_{oc}</math> / mV</b>	<b><math>I_{sc}</math> / mA/cm<sup>2</sup></b>	<b>FF / %</b>	<b>PCE / %</b>
<b>At 140 °C</b>				
PCDTBT/CIS	276 ± 19	6,15 ± 0,19	30,6 ± 0,9	0,52 ± 0,05
PCDTBT/CIS:HA	419 ± 21	5,35 ± 0,46	42,8 ± 1,7	0,96 ± 0,17

**Table 3: Influence of n-hexylamine on the performance of PCDTBT/CIS solar cells at 140 °C (mean values of each best ten cells are given);  $V_2O_5$  was used as ABL.**

Again the presence of n-hexylamine leads to a significant performance improvement of the hybrid solar cells, which is caused by a tremendous increase in fill factor and  $V_{oc}$ . The efficiency values were not as good as they were when PEDOT:PSS was used, which was expected, as the  $V_2O_5$  interlayer was not optimized at all. Nevertheless, the effect of n-hexylamine is completely the same in the case of  $V_2O_5$ , even more significant, and therefore absolutely independent from the use of PEDOT:PSS as anode buffer layer. A comparison between the I-V curves of a sample with and without n-hexylamine is depicted in Figure 34.

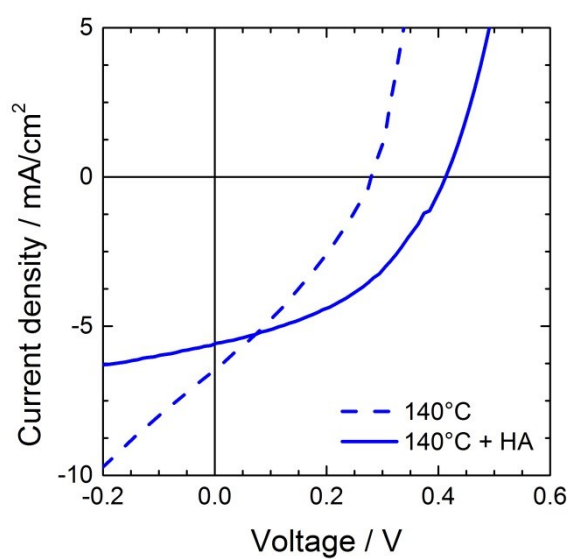


**Figure 34: I-V curves of PCDTBT/CIS solar cells prepared at 140 °C with and without hexylamine; V<sub>2</sub>O<sub>5</sub> was used as ABL.**

# **CHAPTER V**

## **INVERTED HYBRID SOLAR CELLS**

## 1 Introduction

This chapter is dealing with the introduction of the inverted architecture for *in situ* synthesized hybrid polymer/CIS solar cells. In an inverted solar cell, the charge flow is reversed. Thus the electrons are transported towards the ITO electrode at the bottom, which consequently acts as cathode (Figure 35). Vice versa the holes travel through the cell towards the top of it, where they are collected by an appropriate metal, which acts as anode in this case. To realize this geometry the top electrode has to have a work function higher than the one of ITO in order to reach an inversion of the internal electrical field. A way to support the reverse of the charge flow is to insert an electron blocking layer above or a hole blocking layer below the hybrid layer (Figure 35).

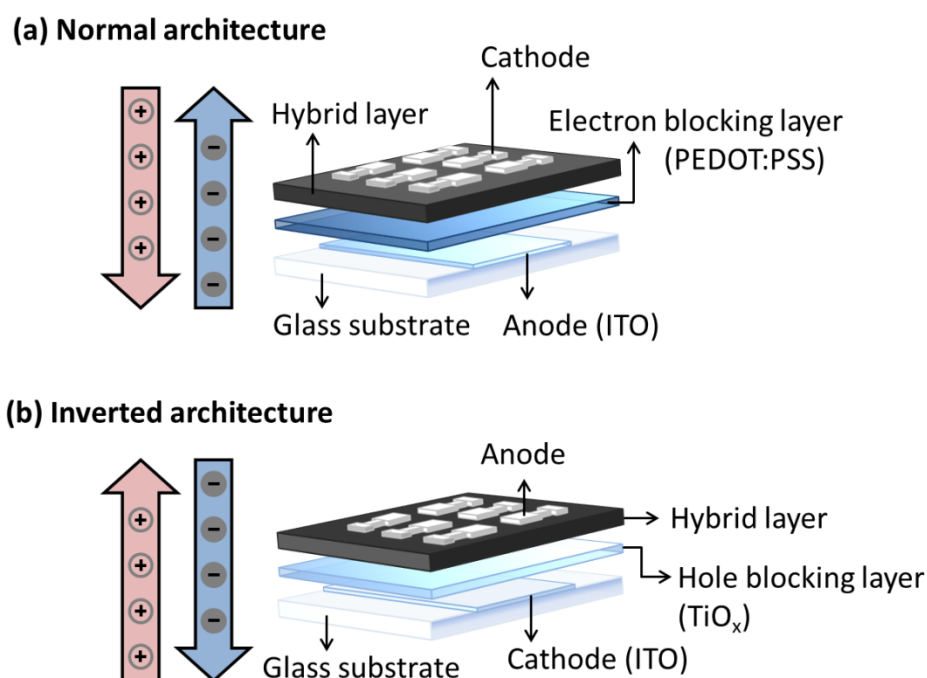


**Figure 35: Schematic comparison of the architecture and the electrical cycle in (a) a normal hybrid solar cell and (b) an inverted hybrid solar cell.**



The inverted architecture was already successfully used in hybrid polymer/CdS solar cells, which were synthesized via a quite similar *in situ* route [55]. Using this architecture offers the possibility to introduce a crystalline titanium oxide ( $\text{TiO}_x$ ) interlayer, which is reported to have a positive effect on the solar cells performance.  $\text{TiO}_x$  is used in organic and hybrid solar cells as cathode buffer layer (CBL), as it is a good electron transporting material. Additionally the use of a  $\text{TiO}_x$  interlayer reduces the sensitivity of the solar cell to oxygen and humidity and thus enhances the solar cells lifetime and stability [126,127]. The positive effect of the inverted approach with a  $\text{TiO}_x$  interlayer on the air-stability of organic P3HT/PCBM solar cells has already been shown [128]. This factor is of high interest, as most of the organic and hybrid solar cells are insufficient in terms of long term stability.

As mentioned above,  $\text{TiO}_x$  is a CBL and therefore has to be applied on top of the photoactive layer, if the normal solar cell architecture is used. There is one way to apply a titanium oxide layer using only a mild heating step (80 °C) published in literature [129,130]. Nevertheless, in experiments this method turned out to be not suitable for polymer/CIS solar cells, as no beneficial effect could be detected. Other ways to apply titanium oxide require a high-temperature annealing step at temperatures high above the decomposition temperature of the photoactive polymer. Therefore, they are not applicable for normal arranged polymer based solar cells. In contrast to that the  $\text{TiO}_x$  layer formation is the first step of the solar cell fabrication process, if the inverted architecture is used, which offers the possibility to use a high temperature annealing step (see experimental section, page 77).

## 2 Experimental Section

### 2.1 Sample preparation

#### 2.1.1 Pre-Treatment of the Substrates

The patterned glass/ITO substrates (Xin Yang Technology Ltd.,  $R_s = 10 \Omega/\text{sq}$ ) were cleaned with acetone, ultra-sonicated in isopropyl alcohol for 30 minutes and exposed to a  $\text{O}_2$  plasma etching process (FEMTO, Diener electronic, 3 min).

#### 2.1.2 Titanium Oxide Interlayer

##### 2.1.2.1 Formation via Spray Pyrolysis

Cleaned substrates were heated to  $450 \text{ }^\circ\text{C}$  (ceramic glass heating plate) and subjected to spray pyrolysis deposition of titanium oxide from a 0.1M solution of di-isopropoxytitanium bis(acetylacetonate). 600 mL of the titanium oxide precursor solution were used for the deposition. The devices were kept on a ceramic glass heating plate for 15 minutes.

##### 2.1.2.2 Formation via Doctor Blading

For the formation of the  $\text{TiO}_x$  layer, a 0.1M di-isopropoxytitanium bis(acetylacetonate) solution in isopropanol was deposited on an ITO-substrate by doctor blading, which was subsequently heated to  $350 \text{ }^\circ\text{C}$  if not another temperature is mentioned. Precursor solution deposition and annealing, which was done on a ceramic glass heating plate for 15 minutes, were carried out in ambient conditions.

### 2.1.3 Cadmium Sulfide Interlayer

The CdS interlayer was formed out of a 0.1M cadmium-2,2-dimethylpentan-3-yl xanthate precursor solution in chlorobenzene, which was applied by doctor blading at 40 °C. The thermal conversion was carried out on a heating plate at 150 °C for 10 minutes. The whole process was done under inert conditions.

### 2.1.4 Hybrid Layer

The photoactive hybrid films were prepared by doctor blading of a chlorobenzene solution containing copper xanthates, indium xanthates (copper and indium O-2,2-dimethylpentan-3-yl dithiocarbonate; purchased from Aglycon, Austria; the chemical structures are depicted on page 63, Figure 28) and PSiF-DBT (poly[(2,7-silafluorene)-alt-(4,7-di-2-thienyl-2,1,3-benzothiadiazole)], purchased from 1-Material, Chemscitech Inc., St. Laurent, Canada, chemical structure see Figure 31 on page 67) at 40 °C. The concentration of PSiF-DBT in the precursor solution was 5 mg/mL, the weight ratio PSiF-DBT:CIS was 1:9 and the Cu:In molar ratio 1:1.7. Subsequently the samples were heated from room temperature to 195 °C if not another target temperature is mentioned in the text. The annealing step was carried out on a programmable heating plate (MCS 66, CAT Ingenieurbüro M. Zipperer GmbH), for 30 minutes with a heating rate of 11 °C/min.

### 2.1.5 PEDOT:PSS Layer

PEDOT:PSS (Clevios P VP.AI 4083, purchased from Heraeus) was diluted with isopropanol (ratio (PEDOT:PSS):isopropanol = 1:5) and 0.13 vol% 2,5,8,11-Tetramethyl-6-dodecyn-5,8-diol ethoxylate (Dynol 604 Surfactant,

purchased from Air Products Chemicals Europe, chemical structure is depicted in Figure 36) was added for better wetting properties. This solution was applied by doctor blading at 60 °C under ambient conditions.

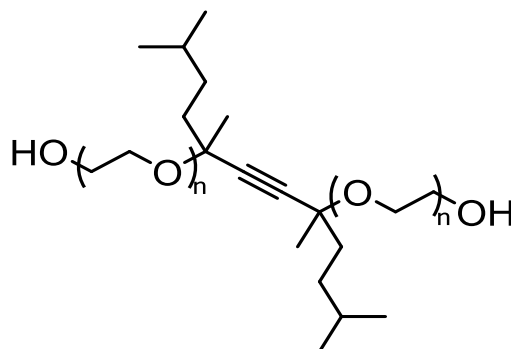


**Figure 36: Chemical structure of Dynol 604 Surfactant**

### 2.1.6 Metal Electrode

200 nm thick silver or gold electrodes were deposited using a thermal evaporation chamber mounted inside a glovebox system (LABmaster dp, MBRAUN Glovebox Technology, Germany) at a base pressure of  $5 \times 10^{-6}$  to  $1 \times 10^{-5}$  mbar (nitrogen atmosphere). The substrates were not cooled during evaporation.

## 2.2 Characterization

The layer thicknesses of the titanium oxide layers were determined by scanning electron microscopy (SEM). The SEM images were obtained from a Zeiss Ultra 55 using an energy selective backscattered electron (EsB) detector at 2 kV. To obtain a planar cross section ion beam polishing (argon) was executed by using the Gatan Ilion+ (model 693, 4 kV, -50 °C, 1 hour, both ion guns were at an angle of 0 °). The thicknesses of all other layers were characterized on a Bruker DekTak XT surface profiler.

I-V curves were recorded using a Keithley 2400 SourceMeter and custom-made LabVIEW software. The solar cells were illuminated using a Dedolight DLH400D (used in conjunction with Dedolight DEB400D electronic ballast). The intensity of the incoming light was set to  $100 \text{ mW cm}^{-2}$  providing a spectrum quite similar to AM1.5G (determined using a KippZonen-CMP-11 pyranometer, no spectral mismatch was considered). The effective device area ( $0.04 \text{ cm}^2$ ) was defined by shadow masks applied to the solar cells.

### 3 Results and Discussion

#### 3.1 Formation of the Titanium Oxide Layer

##### 3.1.1 Layer Thickness

At first the formation of the titanium oxide layer was executed by spray pyrolysis of di-isopropoxytitanium bis(acetylacetonate) (chemical structure see Figure 37), as described in the experimental section. The resulting titanium oxide layers were investigated by scanning electron microscopy with a backscattered electron detector (SEM-BSE).

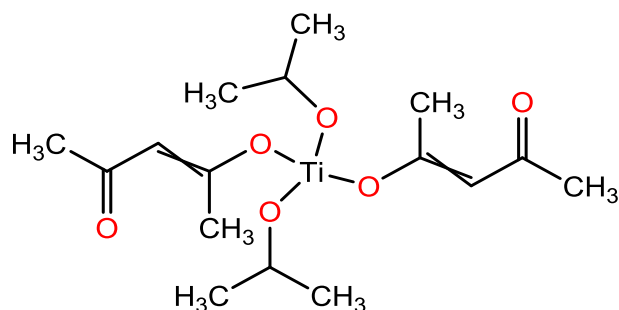


**Figure 37: Chemical structure of di-isopropoxytitanium bis(acetylacetonate).**

These measurements exhibit a layer thickness of about  $1.4\ \mu\text{m}$  with thinner parts down to approximately  $800\ \text{nm}$  and thicker positions up to about  $2\ \mu\text{m}$  (Figure 38). Such a structure implies two main problems. First of all the thickness is too high, as the ideal thickness is reported to be in the range of  $20\text{-}50\ \text{nm}$  [128,131,132]. The thickness, which was obtained by spray pyrolysis, might cause a decrease in electron extraction, as a thick titanium oxide layer might not show adequate electron mobility. However, the titanium oxide layer thickness could be reduced by reducing the amount of precursor solution, which is used for the spray pyrolysis. A bigger problem is the inhomogeneity of the layer surface. Such a rough layer (maximum surface roughness ( $R_{\text{max}}$ )  $\approx 1.2\ \mu\text{m}$ ) cannot be completely covered by the photoactive layer, which has a typical layer thickness of approximately  $60\text{-}80\ \text{nm}$ . Therefore, the required solar cell architecture cannot be obtained, and the solar cell might be shorted.

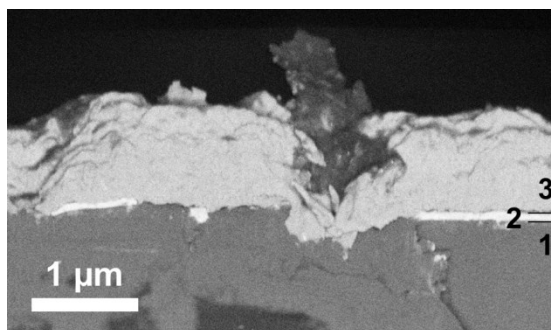


**Figure 38: SEM-BSE cross section image of a titanium oxide layer on glass/ITO substrates prepared via spray pyrolysis. 1: glass, 2: ITO, 3: TiO<sub>x</sub> layer**

As a consequence of these results the titanium oxide precursor solution was applied to the glass/ITO substrate by doctor blading and subsequently annealed in order to form a thinner and especially smoother titanium oxide layer. Figure 39 is a cross-section image of titanium oxide layer formed by

doctor blading, which exhibits that the layer is very smooth and about 20-25 nm thick.

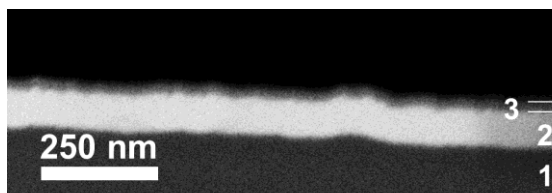


**Figure 39: SEM-BSE cross section image of a titanium oxide layer on glass/ITO substrates prepared via doctor blading and subsequent annealing. 1: glass, 2: ITO, 3: TiO<sub>x</sub> layer**

Therefore the titanium oxide layer was formed by this method for all further experiments.

## 3.2 Inverted Solar Cells

### 3.2.1 Optimization of the Electron Extraction

In the first experiments on the inverted architecture, solar cells consisting of titanium oxide as hole blocking layer, PSiF-DBT/CIS as hybrid layer and gold as anode material on top were prepared (Figure 40(b)). PSiF-DBT and CIS as compounds of a hybrid layer as well as the signification of titanium oxide interlayers have been discussed in detail in previous sections of this work. Gold was chosen as anode material, because it has a work function in the range of 5.3-5.5 eV [133,134], which is well above the values that are specified for ITO. The work function of ITO is reported to be in a range of 4.3-4.7 eV, as long as it is not objected to any special treatment, but O<sub>2</sub> plasma etching [135–137].

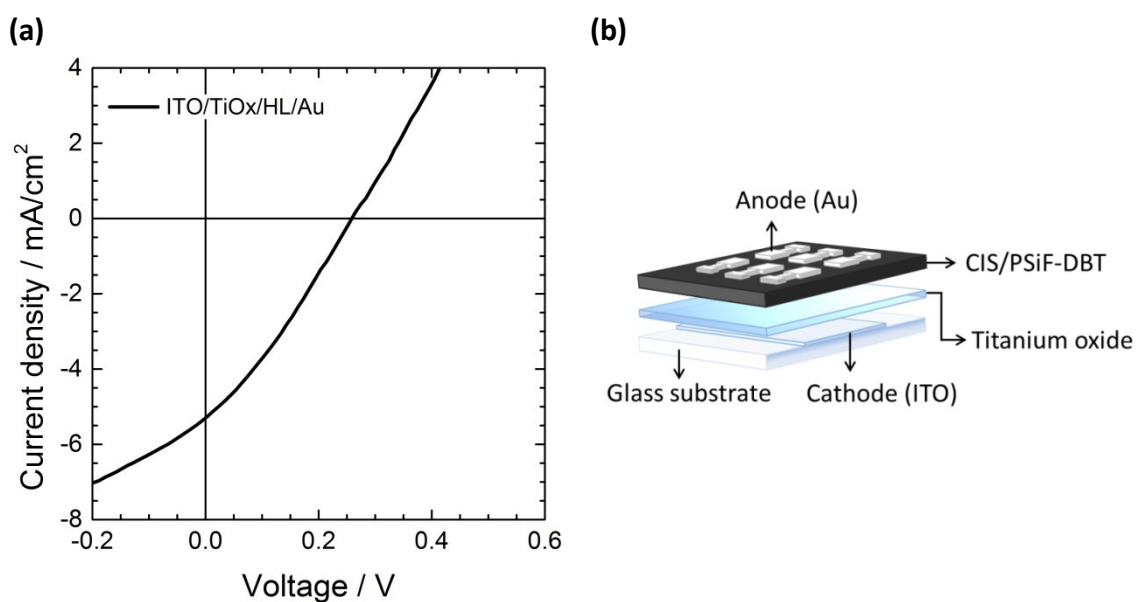


**Figure 40: (a) I-V curve and (b) a schematic depiction of a simple inverted hybrid solar cell. The I-V data was obtained after a photo-annealing step, which is explained in detail on page 88 et seq.**

These inverted cells showed rather poor efficiencies of up to 0.40%. The  $I_{sc}$  showed low average values up to 5.5 mA/cm<sup>2</sup>. Nevertheless, the bad performance of these cells can be primarily attributed to their low open circuit voltages, which stayed constantly below 250 mV, and their fill factors, which did not reach more than 30%. The respective I-V curve is depicted in Figure 40(a).

Therefore, a CIS layer was introduced between the titanium oxide and the hybrid layer (Figure 41(b)) in order to improve the efficiency, as it was shown for a similar hybrid system by Dowland et al. (Ref. [55]), who reached an improvement in PCE of 50%. The effect, this acceptor phase interlayer might or should have on the solar cell is not completely clear [55]. Again it might have an influence on the electron transport from the hybrid layer towards the cathode. However, in this case the insertion of a CIS interlayer did not have any positive effect on the solar cell performance as you can see from the I-V curve in Figure 41(a).



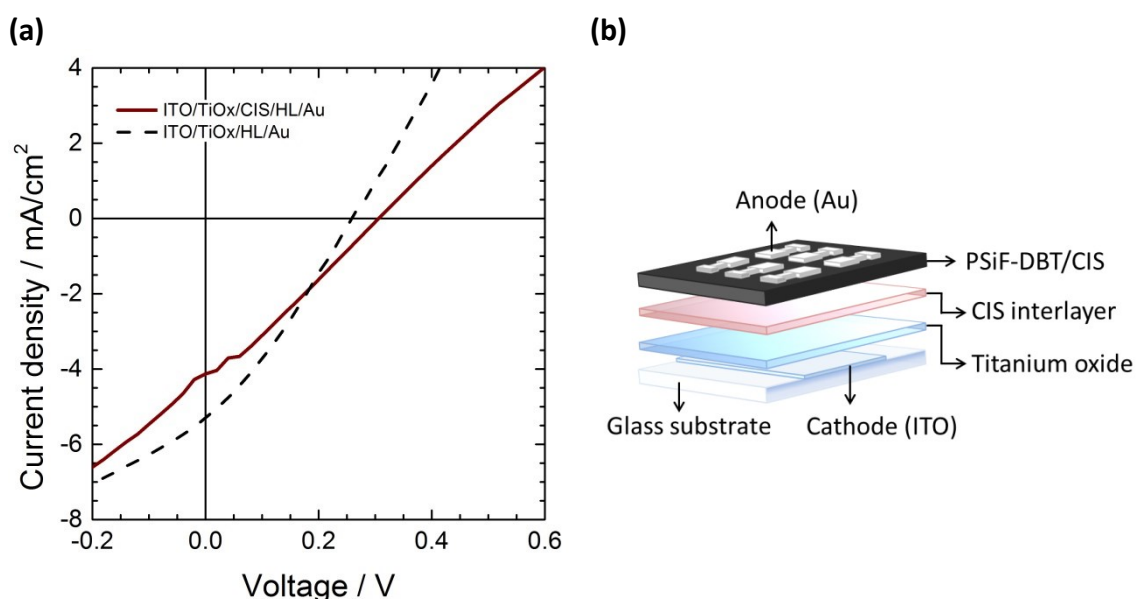


**Figure 41: (a) I-V curve comparison to show the effect of a CIS interlayer and (b) a schematic depiction of an inverted hybrid solar cell with a CIS interlayer. The I-V data was obtained after a photo-annealing step, which is explained in detail on page 88 et seq.**

Compared to the inverted hybrid solar cells without a CIS interlayer, this construction exhibited a slightly higher  $V_{OC}$  of up to 300 mV, which is still a low value though. The other two parameters dropped, as the  $I_{SC}$  was limited to a maximum of 4 mA/cm<sup>2</sup> and the FF was in the range of 25%. As it can be seen from Figure 41(a), the I-V curve of the inverted hybrid solar cell containing a CIS interlayer does not show a characteristic diode curve, but a nearly linear gradient. Thus PCEs of only 0.36% could be obtained for this construction. The CIS layer thickness ( $d_L$ ) was 20-30 nm.

Because of the bad performance of these hybrid solar cells, the CIS interlayer was replaced by a cadmium sulfide interlayer ( $d_L \approx 20$  nm) in the next step (Figure 42).

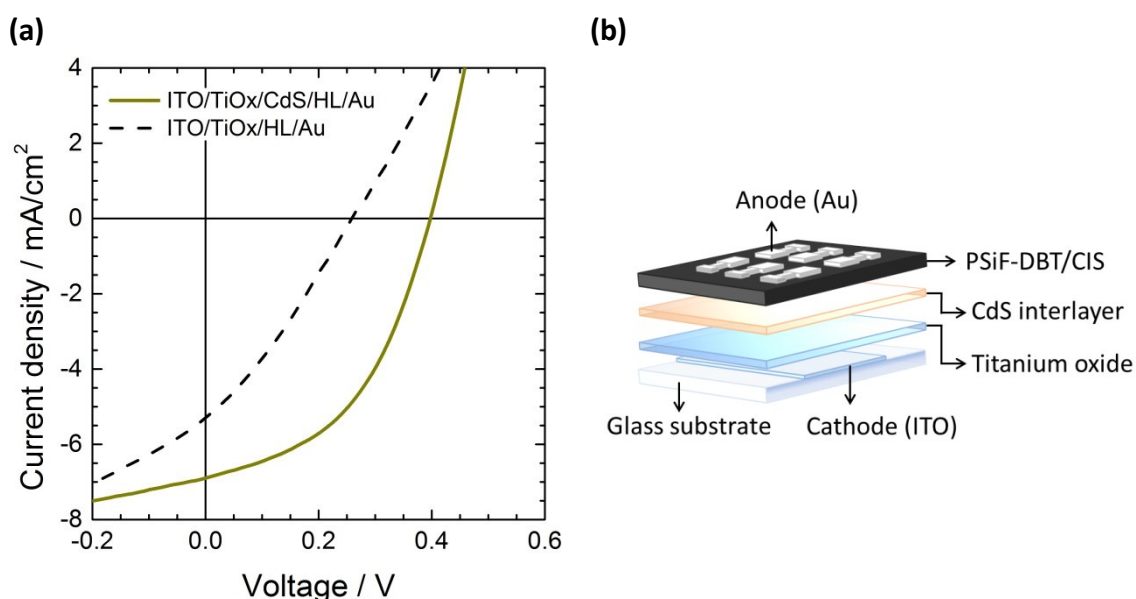


**Figure 42: (a) I-V curve comparison to show the effect of a CdS interlayer and (b) a schematic depiction of an inverted hybrid solar cell with a CdS interlayer. The I-V data was obtained after a photo-annealing step, which is explained in detail on page 88 et seq.**

The CdS interlayer lead to an improvement of all characteristic photovoltaic parameters and thus to a tremendous increase of the power conversion efficiency. The open circuit voltage increased up to nearly 400 mV and the highest  $I_{SC}$  values were just below 7 mA/cm<sup>2</sup>. Especially the fill factor exhibited very satisfying values of up to 47.6% and thus power conversion efficiencies up to 1.25% could be reached with this construction. The results of all different inverted structures are summarized and compared in Table 4 on page 87.

The type of influence of the CdS interlayer and its difference in mode of action compared to a CIS interlayer were not investigated in this work. Nevertheless, its effect on the solar cell performance is that impressive that the implementation of a CdS interlayer became obligatory for all further experiments on inverted hybrid solar.

### 3.2.2 Optimization of the Hole Extraction

As mentioned before, PEDOT:PSS is often used as interlayer to improve the hole transport from the photoactive layer towards the anode. Therefore, the insertion of PEDOT:PSS was investigated. In this case gold was replaced by silver ( $WA \approx 4,3-4,7$ ) as top electrode, as the internal electrical field is already inverted aligned by the arrangement of the selective interlayers. In some control experiments no differences between gold and silver electrodes could be detected for this solar cell construction.

The insertion of a PEDOT:PSS layer lead to a further improvement of the  $V_{OC}$ , which reached high values of up to nearly 600 mV. The  $I_{SC}$  increased in a similar way as more than 8 mA/cm<sup>2</sup> were detected. Therefore, power conversion efficiencies of up to 1.6% could be achieved with this construction, although the fill factor decreased to values in the range of 34%. A comparison of the I-V characteristics is given in Figure 43(a) beside a schematic depiction of the most effective inverted hybrid polymer/CIS solar cell construction.

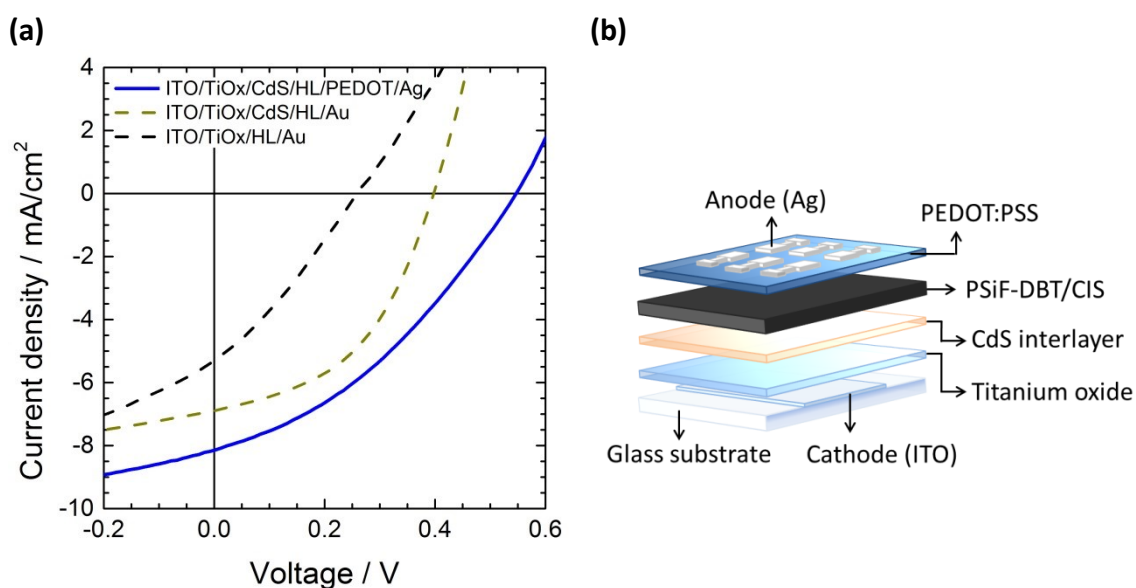


**Figure 43: (a) I-V curve comparison to show the effect of a PEDOT:PSS interlayer and (b) a schematic depiction of the most effective inverted hybrid solar cell construction. The I-V data was obtained after a photo-annealing step, which is explained in detail on page 88 et seq.**

Composition	V <sub>oc</sub> / mV	I <sub>sc</sub> / mA/cm <sup>2</sup>	FF / %	PCE / %
ITO/TiO <sub>x</sub> /HL/Au	236 ± 18	5,30 ± 0,27	29,5 ± 0,9	0,36 ± 0,04
ITO/TiO <sub>x</sub> /CIS/HL/Au	292 ± 20	3,94 ± 0,32	25,7 ± 2,4	0,30 ± 0,04
ITO/TiO <sub>x</sub> /CdS/HL/Au	386 ± 8	6,39 ± 0,49	46,3 ± 1,3	1,13 ± 0,07
ITO/TiO <sub>x</sub> /CdS/HL/PEDOT:PSS/Ag	549 ± 45	7,95 ± 0,23	33,3 ± 2,1	1,45 ± 0,11

**Table 4: Summary and comparison of the characteristic photovoltaic parameters of the investigated types of inverted hybrid solar cell construction (mean values of each best ten cells are given).**

### 3.2.3 Light Soaking Effect

At this stage it has to be noted that all the I-V curves, which are depicted in this chapter were recorded after a light soaking period. The light soaking effect is well studied for devices containing electron selective metal oxide interlayers such as ZnO [138] and TiO<sub>2</sub> [129,139–141]. This effect is often also called photo-annealing effect. Solar cells containing metal oxide layers often exhibit lower efficiencies immediately after the fabrication as they do after a post-processing illumination period.

For the solar cells that were fabricated within the experiments described in this chapter, an improvement in PCE was already reached after 12 hours of storage at inert conditions, were the cells were exposed to no special illumination but the normal light in the laboratory. However, the direct illumination (100 mW/cm<sup>2</sup>) for 30 minutes leads to a further increase. Interestingly the solar cells containing a PEDOT:PSS interlayer showed much lower PCEs immediately after their fabrication than the ones without, but exhibited a much higher increase due to the light soaking process. Solar cells with a PEDOT:PSS interlayer reached an increase in PCE of up to 360% after 12 hours of storage and 30 minutes of direct illumination, whereas solar cells without PEDOT:PSS reached a PCE improvement of not more than 30% compared to their initial values. A comparison of the data is given in Figure 44 and the influence of the light soaking process on the respective I-V curves is depicted in Figure 45.

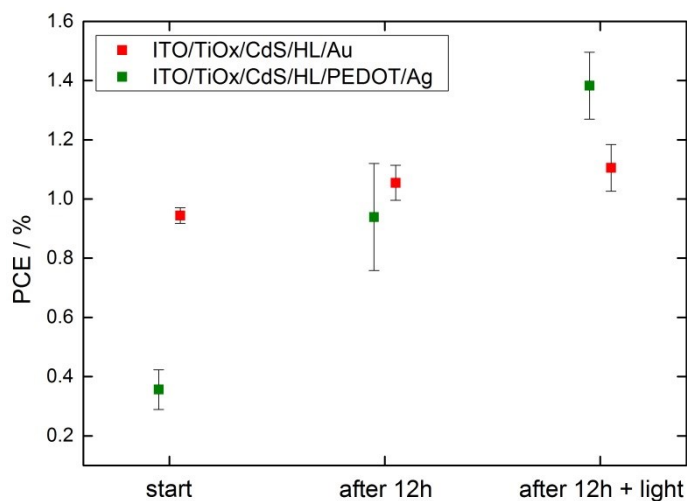


**Figure 44: Light soaking effect on the PCE of inverted hybrid polymer/CIS solar cells with and without a PEDOT:PSS interlayer.**

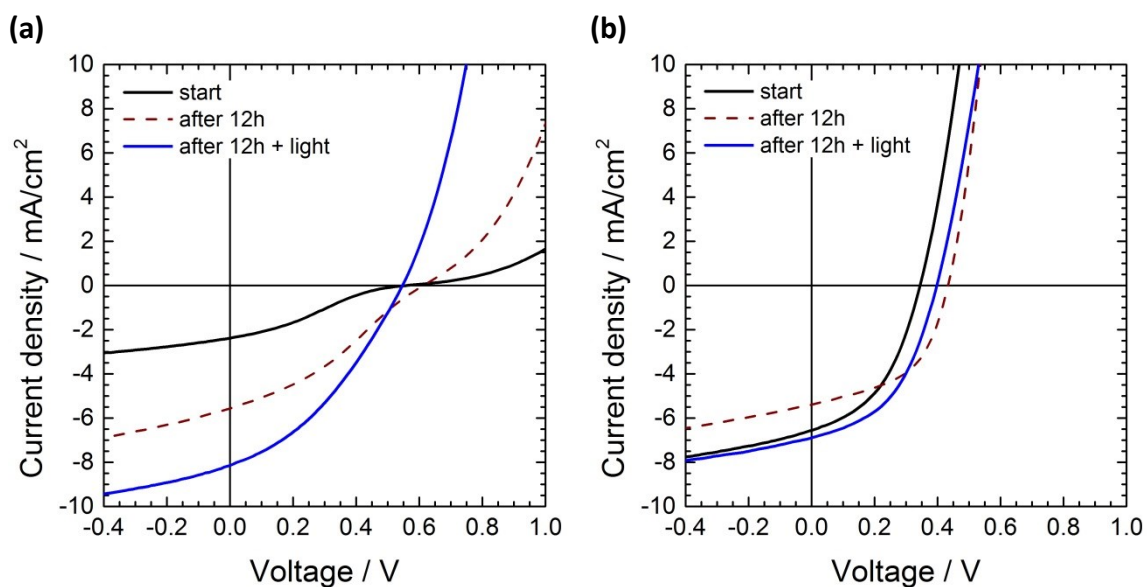


**Figure 45: Light soaking effect on inverted hybrid polymer/CIS solar cells (a) with a PEDOT:PSS interlayer (fabricated at ambient conditions) and (b) without a PEDOT:PSS interlayer (fabricated at inert conditions).**

The different intensity of the photo-annealing effect on these solar cells is strongly assumed to be not related to the presence of the PEDOT:PSS layer, but to the fact, that the PEDOT:PSS coating was executed at ambient

conditions. This had to be done due to the fact that the PEDOT:PSS solution is water-based and thus would be harmful to the inert conditions in the glove box system, were all the other solar cell production steps take place. This means that the PEDOT:PSS containing solar cells were exposed to oxygen and water during the fabrication, whereas the other cells were completely fabricated and stored under inert conditions. Therefore the cells without PEDOT:PSS do not show the typical inflection point behavior and the resulting tremendous increase after illumination. The weaker but still significant improvement of these cells might be attributed to the improved conductivity of titanium oxide under UV-illumination [139] or be a result of a thermal effect [142]. This assumption also goes along with the fact that especially the cells, which contain a PEDOT:PSS layer and thus were exposed to oxygen and humidity showed an increase in PCE of up to 220% just by storing them in the glove box for half a day. By storing them under inert conditions with constant gas purification, the oxygen ratio in the whole cell and especially the humidity in the not tempered PEDOT:PSS layer (see experimental section, page 78) might be reduced already significantly.

As it can be seen from Figure 45(a), primarily responsible for the poor performance of the PEDOT:PSS containing solar cells immediately after their fabrication, is a low fill factor. The I-V curves are “S-shaped”, which means that they have an inflection point in the 4<sup>th</sup> quadrant. The inflection is often attributed to an energy barrier within the solar cell, which is caused by a poor carrier transport in one of the layers or at one of the interfaces which prevents charge extraction [142]. The photo-annealing process that leads to the removal of the inflection point is attributed to photoconductivity of the metal oxide layer, and an oxygen redistribution process within the cell [142]. The illumination might also be advantageous

for the degradation of impurities in the metal oxide layer [142]. It was also shown that the temperature increase, which goes along with the illumination, is beneficial for a fast removal of the inflection point [142]. This effect was expected, as higher temperatures will enhance the rate of most chemical and transport processes [142]. Nevertheless, photo-annealing is not a merely thermal but a photoactive process. This is confirmed by investigations, which showed that the solar cell performance rises faster with increasing illumination intensity and that the absence of UV light at the post-processing illumination leads to a significant slower performance increase [142]. The UV-depending behavior was observed for different metal oxides [143,144]. In the case of titanium oxide it is assumed that the UV-light illumination leads to a high density surface state, which may result in improved electron transport [143]. The origin of these surface states could be an oxygen vacancy [145] or  $Ti^{3+}$  states induced by the photoreaction under light soaking [146].

#### 3.2.3.1 Reappearance of the Inflection Point

The performance of the PEDOT:PSS containing inverted hybrid polymer/CIS cells stayed nearly constant but after some time of storage at inert condition without illumination, the inflection point started to come back. However, the execution of a further photo-annealing step of just 5 minutes led to a normal kink-free diode curve again (Figure 46). These results are in agreement with literature, as the appearance of the inflection point is reported to be partially reversible. The inflection point can re-appear after a storage in the dark but also can be removed again by a light soaking step [142].



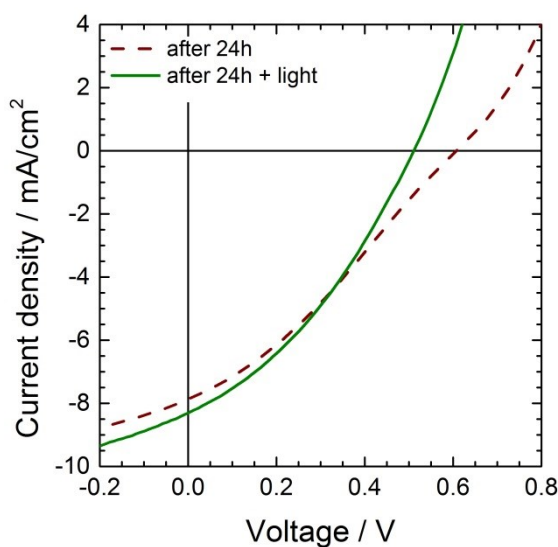


**Figure 46: Re-appearance and repeated removal of the inflection point. Solar cell construction: ITO/TiO<sub>x</sub>/CdS/HL/PEDOT:PSS/Ag**

## 4 Conclusion

Different constructions of inverted hybrid polymer/CIS solar cells were fabricated and investigated. The titanium oxide layer formation was optimized for its use as electron selective interlayer. Further, it has been found that the presence of a cadmium sulfide interlayer, although its mode of action is not totally clarified yet, is crucial for the solar cell performance as well as a PEDOT:PSS electron blocking layer. The appearance of an inflection point immediately after the preparation of the inverted hybrid solar cells was shown to correlate with the presence of oxygen and humidity during the fabrication process. The inflection point behavior was removed by a post-process photo-annealing step for solar cells stored at inert conditions. A reappearance of the inflection point can again be easily removed by illumination. Overall the inverted structure was successfully introduced to *in situ* synthesized hybrid polymer/CIS solar cells and efficiencies up to 1.6% were achieved. Nevertheless, there is still room for

improvement as the efficiencies obtained for the normal architecture [56] could not be reached for the inverted architecture. Thus this approach should be the point of interest for further investigations as its applicability was proven and it offers advantages concerning the use of electron selective interlayers.

# **CHAPTER VI**

## **EXTREME UV-LITHOGRAPHIC CONVERSION OF METAL XANTHATES**

This chapter was originally published in *The Journal of Materials Chemistry A (RSC)* [84]:

**Direct Extreme UV-lithographic conversion of metal xanthates into nanostructured metal sulfide layers for hybrid photovoltaics**

Thomas Rath, Celestino Padeste, Michaela Vockenhuber, Christopher Fradler, Mathias Edler, Angelika Reichmann, Ilse Letofsky-Papst, Ferdinand Hofer, Yasin Ekinci, Thomas Griesser

*Journal of Materials Chemistry A*, 2013, 1, 11135-11140  
(doi: 10.1039/c3ta12592k).

Reproduced by permission of The Royal Society of Chemistry

## 1 Introduction

Organic-inorganic hybrid solar cells based on conjugated polymers and inorganic semiconducting nanostructures are currently a field of intensive research because of their promising properties due to combining advantages of both organic and inorganic semiconductors. A large variety of organic-inorganic material combinations may be blended to form bulk heterojunction absorber layers for hybrid solar cells [90,91]. Most prominent examples are combinations of a conjugated polymer with CdSe [97], CdS [52], CuInS<sub>2</sub> [56], PbS [99], or ZnO [100]. Up to now, maximum power conversion efficiencies (PCEs) between 4 and 5% are reported for organic-inorganic hybrid solar cells [52,98]. One very promising strategy to further improve the PCE of hybrid solar cells is to modify the bulk heterojunction toward a more ordered morphology. Ordered heterojunction structures of the organic and the inorganic component, which are vertically bicontinuous and interdigitized, can significantly improve charge transport properties, while maintaining a high interfacial area [83].

In fully organic polymer/[6,6]-Phenyl C<sub>61</sub> butyric acid methyl ester (PCBM) solar cells, such ordered bulk heterojunctions are mainly prepared using nanoimprint lithography (NIL) to pattern the polymer layer, which is infiltrated by PCBM [82,83]. In the case of hybrid material systems, mainly the inorganic semiconductor is patterned and infiltrated with the organic donor material [82]. Nanostructured hybrid solar cells were realized so far with several material classes including mostly metal oxides [82,147] but as well also e.g. silicon [148–150] or gallium arsenide [151]. The nanostructures were typically prepared by (template assisted) nanorod or nanotube growth, etching, or selected area epitaxy processes.

To date, ordered polymer/metal sulfide heterojunctions have not been explored at all. This may originate in the fact that only a very limited number of methods for the preparation of nanostructured metal sulfide layers exist, even though semiconducting metal sulfides are a very important class of materials which are widely used in hybrid as well as in inorganic thin film solar cells. Furthermore, they are important in a wide range of further applications like waveguides, sensors, photodetectors, electroluminescent devices or photocatalysts, where nanostructured layers can be beneficial [152–155]. While, in particular in hybrid solar cells, structured metal sulfide layers can find prospective application for the formation of a well-defined ordered heterojunction in the absorber layer to enhance device performance [82], in inorganic thin film solar cells, nanostructured layers can be used as light trapping layers to optimize absorption properties [156], or to improve carrier collection [157].

So far, structured metal sulfide layers were mainly prepared by lithographic patterning of functional surface molecule layers or self-assembled monolayers on the substrate followed by selective growth or deposition of the metal sulfide [152,153,158–160], via electron-beam lithography (EBL) [161,162] or by molecular printing techniques [163,164]. Following the first method, the organic layer remains between metal sulfide layer and substrate after structuring, which may limit possible applications of the nanostructured layers. With the latter mentioned methods only very small areas can be structured in reasonable time.

## **2 Results and Discussion**

In this work, we introduce an exciting strategy for the fabrication of column structures as well as comb structures showing periodicities of

140 nm with the potential to reach periodicities far below 100 nm. The fabrication process is the direct patterning of the functional nanostructures and does not involve pattern transfer such as lift-off or etching. In this route metal xanthates are used as precursors, which can be thermally converted to metal sulfides [56,165], but also by UV-light [166]. This offers the possibility for the formation of structured metal sulfide layers via a photochemically induced solid state reaction. The used metal xanthates show strong absorption at wavelengths below 300 nm leading to their decomposition and subsequent formation of the corresponding metal sulfides upon UV- or extreme UV (EUV)-illumination under reduced pressure. We demonstrate the potential of this method with the semiconducting metal sulfide copper indium sulfide (CIS), a well-known absorber material in thin film photovoltaics, and also already successfully incorporated in organic-inorganic hybrid solar cells [56].

Figure 47 shows FT-IR spectra of a layer containing a mixture of copper and indium xanthates before and after UV-illumination (mercury medium pressure lamp). The characteristic peaks of the xanthates (for a detailed assignment see Table 5 on page 109 in the supplementary information of this chapter) vanished completely after 20 min of UV-illumination. The concerted formation of the copper indium sulfide is proved by the selected area electron diffraction (SAED) pattern of a sample after UV-illumination. The SAED pattern shows diffraction rings, indicating that the sample is nanocrystalline and that the crystals have no preferential order. The positions of the main diffraction rings (112,  $r = 3.19 \text{ nm}^{-1}$ ; 200,  $r = 3.70 \text{ nm}^{-1}$ ; 204/220,  $r = 5.21 \text{ nm}^{-1}$ ; 116/312,  $r = 6.11 \text{ nm}^{-1}$ ) are in good agreement with reference data for chalcopyrite CIS (PDF 27-159). The principle possibility of a formation of nanocrystalline  $\text{CuInS}_2$  solely by UV-treatment of precursors is in agreement with a report by Nairn et al. [167]

who prepared CuInS<sub>2</sub> nanocrystals in an organic solvent by photochemical decomposition of a single-source metal-thiolate precursor.

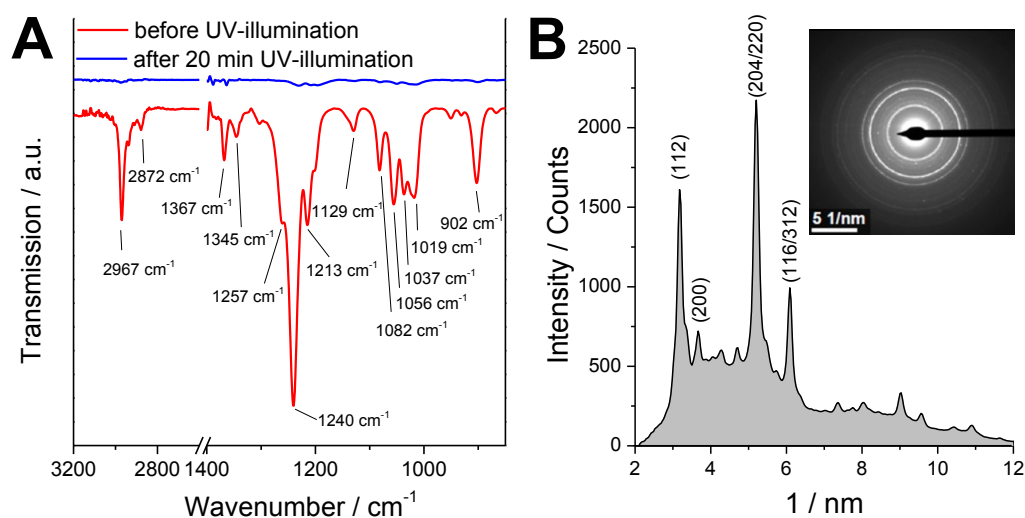


**Figure 47: A) FT-IR spectra of a metal xanthate precursor layer before and after 20 min UV-illumination under reduced pressure; B) SAED image and the corresponding radial intensity profile of the UV-illuminated sample (Ref. [84]).**

Furthermore, scanning electron microscopy - energy dispersive X-ray (SEM-EDX) measurements were conducted to analyze the chemical composition of the nanocrystalline CIS layer formed by photolysis of the metal xanthates. The EDX spectrum reveals a copper/indium molar ratio of about 1/1.6, which is close to the copper/indium ratio of the precursor layer (1/1.7). A surplus of indium is necessary as this leads to n-type CIS [168], which is essential for an application of this material in hybrid solar cells, as only n-type CIS leads to well performing polymer/CIS hybrid solar cells [51,56].

The formation of copper indium sulfide is additionally confirmed by X-ray photoelectron spectroscopy (XPS). The corresponding spectra of the metal xanthate precursor film, of the film after UV-illumination and after thermal



treatment are presented in Figure 48. The XPS signals of the photochemically prepared CIS layer match well with a thermally (195 °C) converted reference sample and for all elements shifts in binding energy between precursor layer and CIS layer are observed. For the elements Cu and In, the binding energies between the precursor layer and the UV-treated sample are shifted about 1 eV to higher energy, for S, the peak is shifted about 0.5 eV to the lower energy region. In the photochemically prepared sample, the binding energies of Cu2p<sub>1/2</sub> and Cu2p<sub>3/2</sub> are 952.6 and 932.9 eV, these of In3d<sub>3/2</sub> and In3d<sub>5/2</sub> are 452.6 and 445.1 eV and the binding energy of S2p corresponds to 162.1 eV. The found binding energies match very well to reference data for CIS from literature [169].

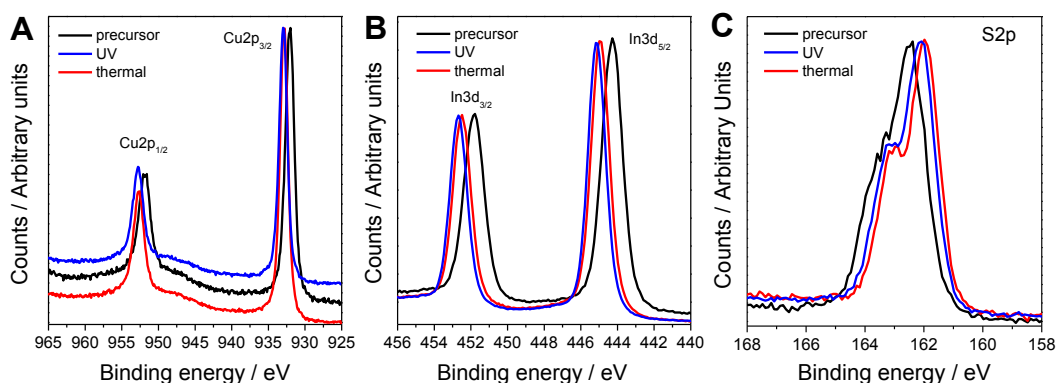


**Figure 48: XPS spectra of the elements Cu (A), In (B) and S (C) in the precursor film (black), after thermal annealing (red) and after UV-treatment (blue) (Ref. [84]).**

The presented data show that it is possible to produce crystalline copper indium sulfide thin films in a solid state reaction by UV-treatment of a precursor layer. This opens the unique possibility for photolithographic structuring of metal sulfide layers. In this structuring process, the metal xanthate precursor can be viewed as negative resist. UV-illuminated areas are cured and become insoluble due to the formation of the metal sulfide,

while the non-illuminated areas remain readily soluble in organic solvents. The principle of the photolithographic structuring process using metal xanthate precursor layers is schematically shown in Figure 49.

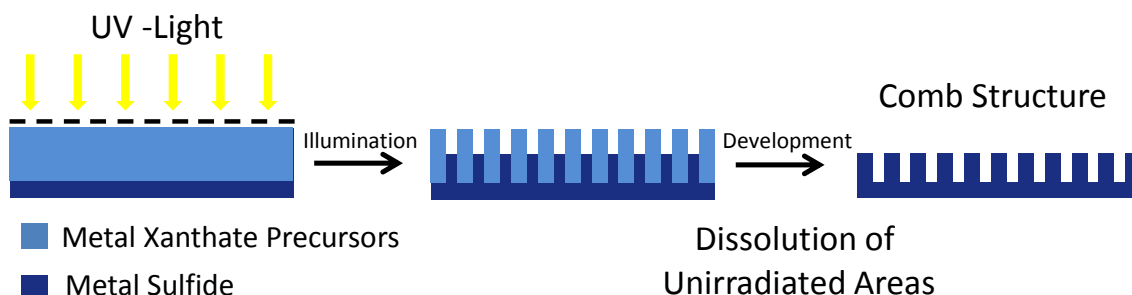


**Figure 49: Schematic illustration of the photolithographic process for the preparation of metal sulfide comb structures from metal xanthates (Ref. [84]).**

To realize a comb structure as shown in Figure 49, in a first step, a thin and continuous CIS layer is prepared by thermal or UV-conversion from metal xanthates on a suitable substrate. Subsequently, a metal xanthate precursor layer, which is coated from solution onto the first CIS layer, is UV-illuminated through a shadow mask. Thus, CIS is formed in the illuminated areas, which leads to shrinkage in volume due to the evaporation of the volatile decomposition products of the metal xanthates [56] and an increase in density in the material. Finally, the structure is developed by short dipping of the substrate into an organic solvent like chloroform or toluene leading to dissolution of the unexposed xanthate.

Using standard UV-photolithography, we could realize comb structures with periodicities down to 5  $\mu\text{m}$  using contact masks. However, for many applications including also the application in absorber layers of organic/inorganic hybrid solar cells, much smaller structures (periodicities of 20-200 nm) are desired. To achieve structures far below 1  $\mu\text{m}$ , we identified extreme ultraviolet interference lithography (EUV-IL) to be an

ideally suited method for this purpose. Also laser interference lithography (LIL), as well as EBL [162] were considered as generally suitable techniques. However, compared to LIL, EUV-IL has the advantage that resolutions far below 100 nm can be achieved. Resolutions in this range would be also possible with EBL; however, using this method, the throughput is limited due to the serial nature of EBL.

In contrast to this, EUV-lithography is currently considered to be the next-generation technique for high-volume semiconductor chip production with feature sizes down to the sub- 10 nm region [170,171]. Interference lithography using EUV radiation gained increasing attention in academic as well as industrial research as a powerful tool providing high resolution, high throughput, and large-area patterning [172,173], which makes this technique also considerably interesting for our application.

In initial series of EUV-IL experiments, we used a “multi-pattern mask” which offered the possibility to create various structures (dots, lines) and periodicities during one exposure using two- and four-beam interference schemes. Besides exposure times, also the thickness of the precursor layer had to be optimized before impressively homogeneous column-like structures with periodicities of 283 nm as well as 141 nm could be achieved. AFM and SEM-SE images of the prepared nanostructures are shown in Figure 50. The height of the nano-columns is about 29-35 nm (corresponding height profiles are included in the supplementary information of this chapter, page 110, Figure 53).

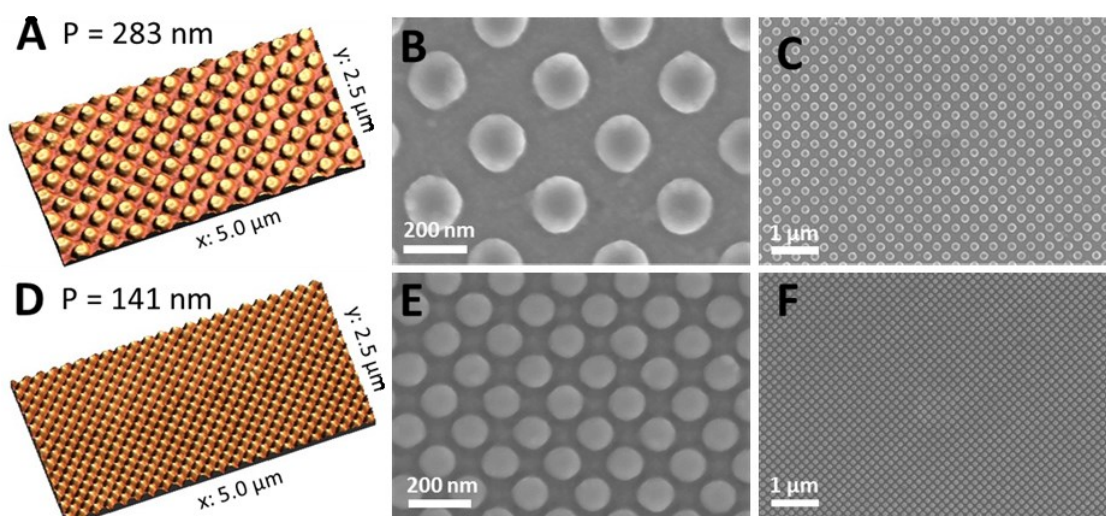


**Figure 50: AFM images (A, D) and SEM-SE micrographs (B, C, E, F) with different magnifications of copper indium sulfide column structures with periodicities of 283 nm (A-C) and 141 nm (D-F) prepared via four-beam interference. The height of the structures is about 29-35 nm (Ref. [84]).**

Regarding a future application of these nanostructured layers in absorber layers of hybrid solar cells, the column structures were not fabricated on silicon substrates, which would be the standard substrates for EUV-IL, but they are already prepared on the layer structure glass/ITO/TiO<sub>x</sub>/CdS (see methods section) which can be directly implemented in hybrid solar cells with inverse device architecture [55]. Prior to the lithographic preparation of the structured CIS layer from the Cu- and In-xanthate precursor layer, a 5 nm thin continuous CIS layer was applied on the glass/ITO/TiO<sub>x</sub>/CdS layer stack. By the introduction of this thin CIS layer, it is provided that the conjugated polymer, with which the nanostructured CIS layer is infiltrated to form an interdigitized network of donor and acceptor in the absorber layer, does not have direct contact to the subjacent layer. This would adversely influence the electronic properties of the final device. After the infiltration with a conjugated polymer, the preparation of hybrid solar

cells can be finished by applying a PEDOT:PSS layer and metal electrodes. Keeping in mind that the nanostructured layers are prepared on a stack of multiple solution-processed layers, the achieved nanostructures are impressively well defined and homogeneous (see Figure 50 F).

The smallest gap between two columns in the sample with the periodicity of 141 nm (Figure 50 D-F) is about 35 nm. This is already quite close to an ideal feature size for efficient charge separation in hybrid bulk heterojunctions, which would be approximately 20 nm, the doubled exciton diffusion length in conjugated polymers [82]. The fact that the structures, even with this very small gaps, are clearly separated and well defined, strongly suggests that the realization of even smaller structure sizes should be possible by further optimization. Thus, the pre-conditions for a successful incorporation of EUV-lithographically structured metal sulfide layers, having feature sizes close to the exciton diffusion length, in absorber layers of hybrid solar cells are fulfilled and future research will be directed to this topic.

The discussed column structures were achieved via four-beam interference. Keeping in mind that the metal xanthate resist needs comparably long exposure time for curing, column structures were easier to realize than line structures, which are reached by interference of two beams, leading to lower intensity. Using standard EUV-IL masks, line structures could not be prepared using exposure times of up to 4 minutes (dose  $\sim 8000$  mJ/cm<sup>2</sup>). We note that this value is the dose on mask level and the dose on wafer level is about 5-10% of this value due to the diffraction efficiency of the grating and absorption of the supporting SiN membrane of the masks. To achieve the goal of realizing line structures and to overcome the above mentioned challenges of exposure time, we also worked with ASFM (achromatic spatial frequency multiplication) technique

in further experiments. In this technique, which is based on the achromatic Talbot effect, all transmitted light contributes to image formation leading to much higher efficiency but also to higher background intensity [174]. This means that exposure times are considerably shorter; however, they have to be most accurately adjusted, as overexposure leads to curing of the full area, and underexposure only to a curing in surface near areas of the film, which leads to full removal of the film during the developing step. Fortunately, metal xanthates appear to provide a well suited sensitivity curve and CIS comb structures with a periodicity of 280 nm could be prepared using an exposure dose of less than 5000 mJ/cm<sup>2</sup>.

AFM as well as SEM-SE images of the line-structures are presented in Figure 51. The comb-structure is regular and has a height difference of 25 nm, as measured with AFM (the corresponding height profile can be found in the supplementary information this chapter on page 111, Figure 54). Using the ASFM technique, areas of 1x1 mm<sup>2</sup> were structured in one exposure step and even bigger nanostructured areas can be easily realized by stitching or using scan exposure mode [175].

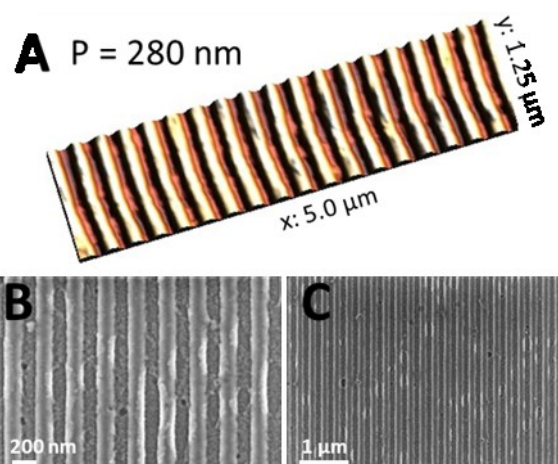


**Figure 51: AFM image (A) and SEM-SE micrographs (B, C) with different magnifications of copper indium sulfide comb structures with a periodicity of 280 nm and a structure height of 25 nm (Ref. [84]).**

In conclusion, we presented a versatile strategy for the preparation of nanostructured metal sulfide layers using metal xanthate precursors. We identified the photosensitivity of metal xanthates as powerful tool for lithographic structuring and successfully realized column as well as comb structures with a periodicity of 140 nm using EUV-IL and we certainly see the potential to achieve nanostructures with resolutions far below 100 nm. To tackle this goal, on the one hand, an optimization of the metal xanthate precursor materials (variation of the alkyl chains) will be necessary in order to reduce the volume shrinkage and to increase their sensitivity to UV-illumination, which will also help to reduce remaining carbon in the nanostructured material. On the other hand, further optimization of the EUV-IL exposures, also including testing of new masks with higher resolution may enable realization of nanostructures with sizes of a few ten nanometers.

### 3 Experimental Details

#### 3.1 Sample preparation and UV-illumination

The used metal xanthates (copper O-2,2-dimethylpentan-3-yl-dithiocarbonate and indium O-2,2-dimethylpentan-3-yl-dithiocarbonate) were synthesized according to a previously published procedure [56]. The precursor layers were prepared via spin coating from chlorobenzene solutions on silicon substrates covered with a thin CIS layer or on glass/ITO substrates covered with TiO<sub>x</sub>, CdS and CIS layers. The TiO<sub>x</sub> layer was prepared by doctor blading a titanium diisopropoxide bis(acetylacetonate)-precursor dissolved in isopropanol and subsequent annealing of the substrate at 450 °C in ambient conditions, the CdS as well as the CIS layer were formed by thermal conversion (160 °C and 195 °C, respectively) of the corresponding metal xanthates. For the photochemical conversion, the metal xanthate layers were illuminated in a quartz glass tube under reduced pressure (approx. 10 mbar) using an Omnicure S1000 lamp (1.1 W/cm<sup>2</sup>, measured with a spectroradiometer, Solatell, Sola Scope 2000TM, spectral range from 230 to 400 nm).

#### 3.2 Extreme UV (EUV) interference lithography

Samples coated with metal xanthate layers were exposed to EUV light at the XIL-II beamline of the Swiss Light Source (SLS). Exposures were performed in vacuum (<5 x 10<sup>-6</sup> mbar). The beamline uses undulator light with a central wavelength of 13.5 nm (92.5 eV photon energy) and 4% spectral bandwidth. The incident EUV power on the mask was about 30 mW/cm<sup>2</sup> and the exposure time in the range of up to 5 minutes was



controlled using a beam shutter. Structure definition was achieved by irradiation through silicon nitride masks with chromium gratings of different periods and arrangements [157] or through gold-plated ASFM masks [174].

### **3.3 Characterization techniques**

The thicknesses of the layers were characterized on a Bruker DekTak XT surface profiler. IR-spectroscopy was performed on a Perkin Elmer Spectrum One. XPS studies were done using a K-Alpha photoelectron spectrometer (Thermo Scientific). AFM measurements were carried out in TappingMode® in air on a Dimension IIIa instrument (Veeco, Germany). The AFM images were analyzed using WSxM software (Nanotec Electronica) [176]. SEM-SE characterizations were done on a Zeiss Ultra 55 equipped with an EDAX Phoenix detector for EDX measurements. SAED was performed on a FEI Tecnai 12 electron microscope.

## **4 Acknowledgement**

Financial support by the Christian Doppler Research Association, the Austrian Federal Ministry of Economy, Family and Youth (BMWFJ), and ISOVOLTAIC AG is gratefully acknowledged. The authors thank Gregor Trimmel and Mario Arar for valuable and helpful discussions and Lukas Troi for technical help. Part of this work was performed at the Swiss Light Source, Paul Scherrer Institute, Villigen, Switzerland.

## 5 Supplementary Information

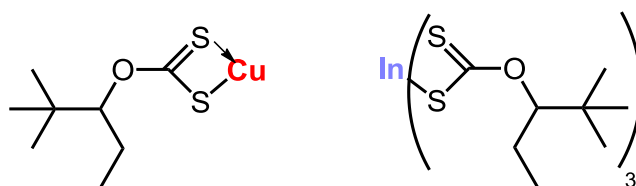


**Figure 52: Chemical structures of the used Cu- and In-xanthates (copper O-2,2-dimethylpentan-3-yl-dithiocarbonate; indium O-2,2-dimethylpentan-3-yl-dithiocarbonate) (Ref. [84]).**

IR frequency / $\text{cm}^{-1}$	Assignments
2967	-CH <sub>2</sub> - str. asym.
2872	-CH <sub>2</sub> - str. sym.
1367	sym. CH <sub>3</sub> bnding
1345	CH wagging
1257	C(CH <sub>3</sub> ) <sub>3</sub>
1240	asym. C-O-C str.
1213	
1129	sym. C-O-C str.
1082	C=S str.
1056	
1037	
1019	
902	CH <sub>3</sub> out of phase rocking

**Table 5: Assignment of the peaks of the Cu- and In-xanthate precursor layer in the FT-IR spectra [177,178] (Ref. [84]).**

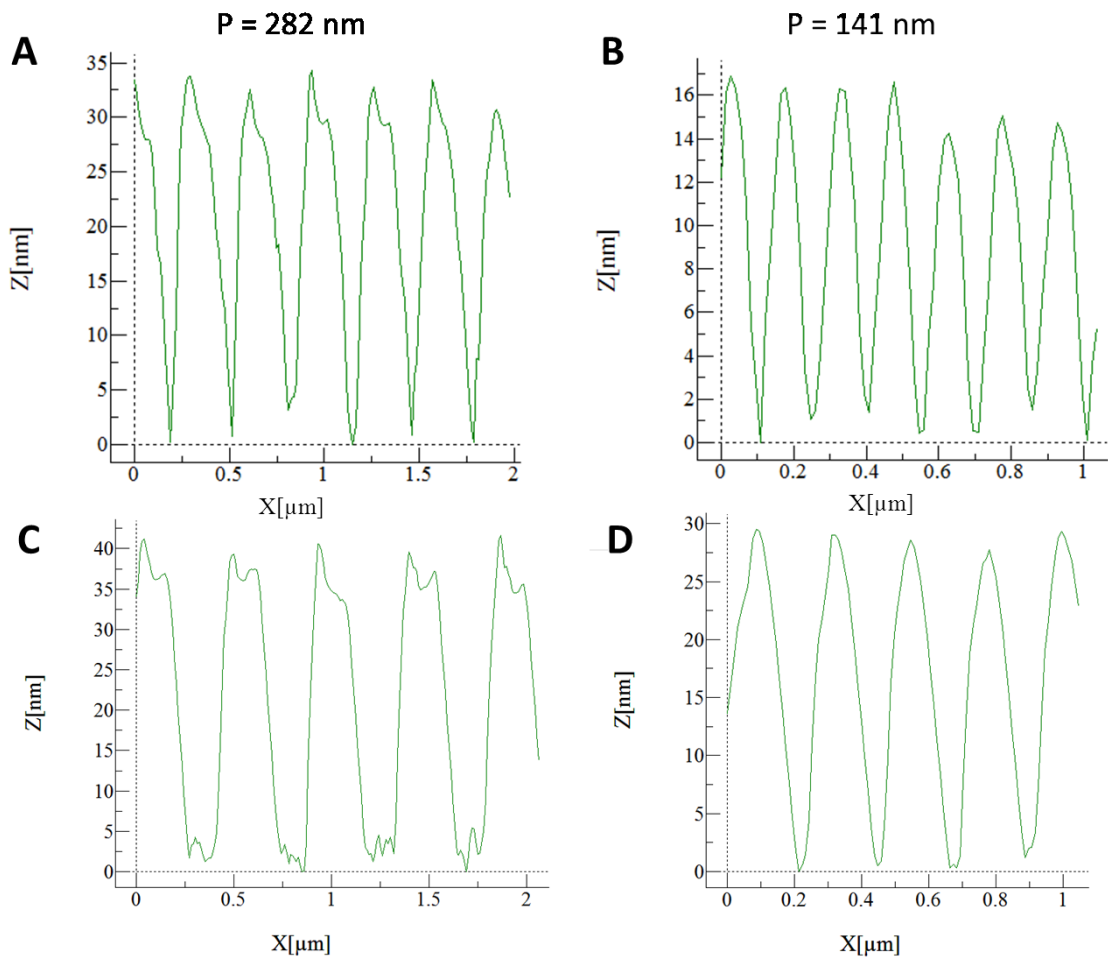


**Figure 53: Height profiles of the column-structures presented in Figure 50 extracted from the AFM images in the diagonal (A, B) and in  $x$ -direction (C, D). For the sample with a periodicity of 282 nm (A, C), the height difference in the structure is about 30-35 nm, for sample  $P = 141 \text{ nm}$  (B, D) it is about 29 nm in  $x$ -direction and about 16 nm in the diagonal (Ref. [84]).**

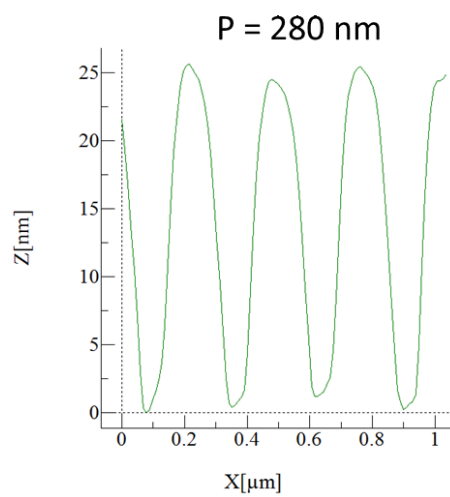


**Figure 54: Height profile of the comb-structures presented in Figure 51 extracted from the AFM image. The height difference in the structure is about 25 nm (Ref. [84]).**

# **CHAPTER VII**

## **CONCLUSION**

*“There must be a beginning of any great matter, but the continuing unto the end until it be thoroughly finished yields the true glory.”*

(Francis Drake, English circumnavigator of the 16<sup>th</sup> century)

## 1 Summary

The topic of this thesis was the investigation of strategies to improve the performance of hybrid polymer/CIS solar cells. The first goal was to reduce the conversion temperature, which was achieved by the addition of a small amount of n-hexylamine to the polymer/metal xanthate precursor solution. Thereby a significant improvement of the crystallinity of the CIS nanoparticles that were annealed at 140 °C could be detected by TEM-BF analyses, whereas the polymer/CIS films prepared at 195 °C showed no difference (Figure 55).

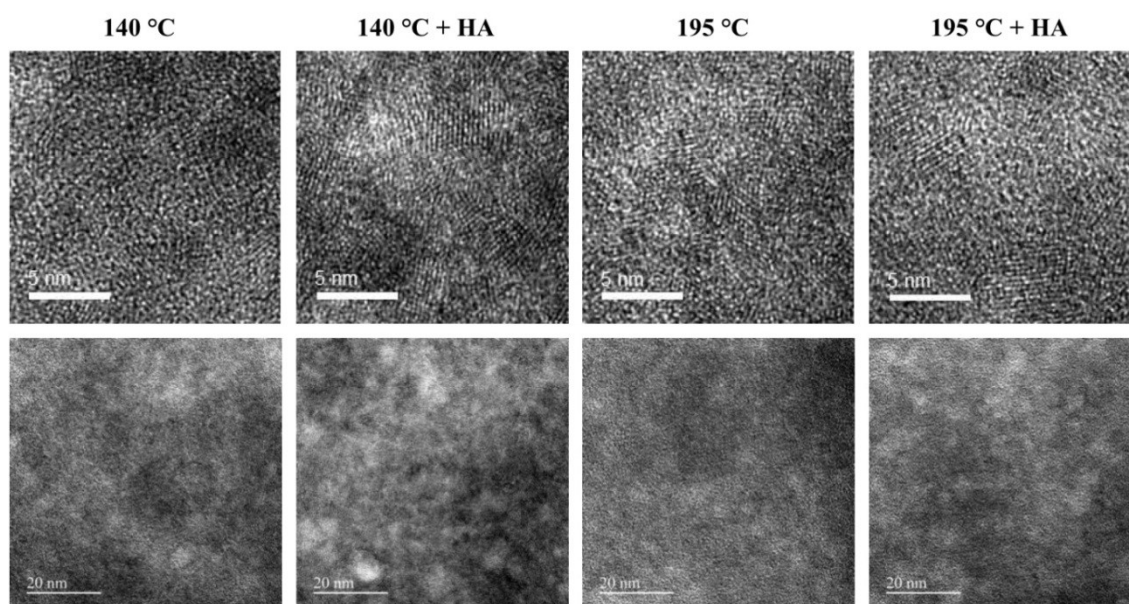


**Figure 55: TEM-BF and HR-TEM-BF images of PCDTBT/CIS nanocomposite layers prepared at 140 °C and 195 °C (Ref. [85]).**

The crystallinity increase for 140 °C was confirmed by XRD-measurements, whereas no dependence on the presence of n-hexylamine was found at 195 °C. This is a consequence of the fact that the decomposition rate of the xanthates is temperature-dependent. If a polymer/metal xanthate

precursor solution is subjected to an annealing step at 140 °C, the decomposition of the xanthates takes much longer than at 195 °C, where the decomposition happens immediately. As it was shown, n-hexylamine reacts with the metal xanthates under formation of the respective thiocarbamate. The reaction scheme is shown in Figure 56.

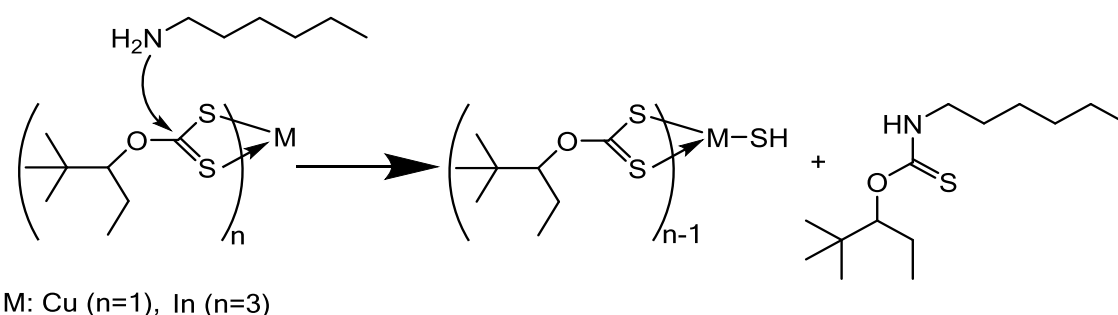


**Figure 56: Schematic depiction of the xanthate decomposition benefitting reaction with n-hexylamine.**

This reaction is beneficial for the decomposition process of the metal xanthates and thus the presence of n-hexylamine catalyzes the formation of CIS nanoparticles in the polymer matrix at lower temperatures. However, at 195 °C the decomposition process happens so fast that the presence of n-hexylamine does not further improve crystallinity.

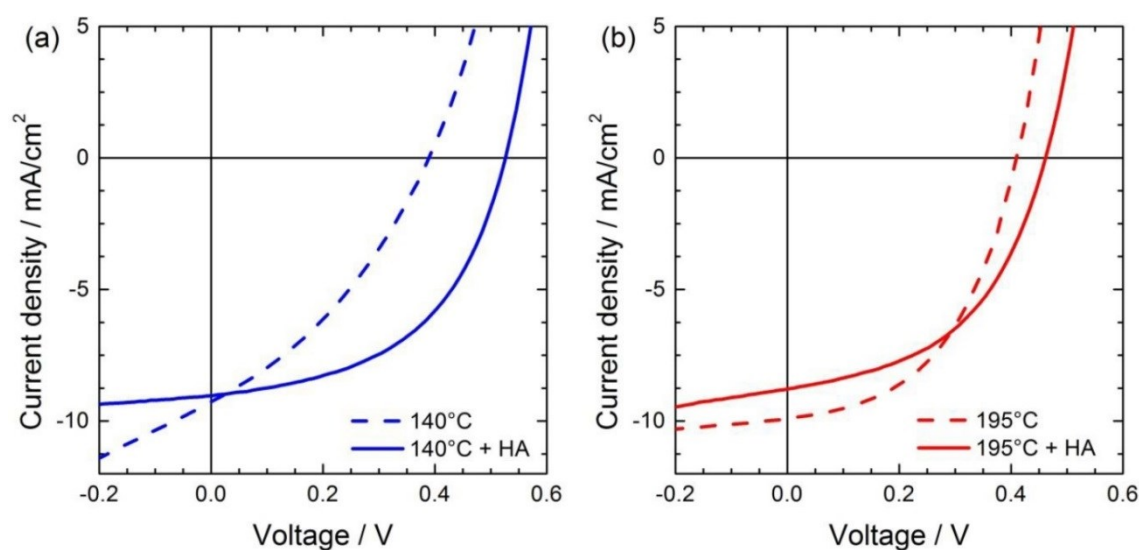


**Figure 57: I-V curves under illumination ( $100 \text{ mW/cm}^2$ ) of PCDTBT/CIS solar cells prepared at annealing temperatures of (a)  $140 \text{ }^\circ\text{C}$  and (b)  $195 \text{ }^\circ\text{C}$  with and without hexylamine (Ref. [85]).**

The Figure above, which shows the I-V curves of solar cells fabricated with and without n-hexylamine at the respective temperatures confirm the investigations on the decomposition process. They show nearly no difference at  $195 \text{ }^\circ\text{C}$ , whereas at  $140 \text{ }^\circ\text{C}$  the efficiency could be almost doubled by the addition of n-hexylamine. The respective I-V curves are depicted in Figure 57. The stability of the devices prepared at low temperatures is also very promising, as glass-glass encapsulated devices prepared at  $140 \text{ }^\circ\text{C}$  show good stability during continuous illumination over 1000 hours.

As it was possible to fabricate efficient hybrid polymer/CIS solar cells at  $140 \text{ }^\circ\text{C}$ , which is an annealing temperature that is also suitable for polymer foil substrates, this method was used to prepare flexible solar cells. These cells exhibited PCEs of up to 1.6%. The drop compared to the solar cells fabricated on glass substrates (2.4%) is mainly attributed to the deposition method that was used. The polymer/CIS precursor solution was applied by



doctor blading. This technique requires the substrate to be completely flat, which is very difficult to realize for foils. This low temperature annealing process, which is schematically illustrated in Figure 58, was also used to fabricate hybrid polymer/CIS solar cell modules on glass and on PET foil. These modules exhibited efficiencies of 1.0% and 0.33% respectively.

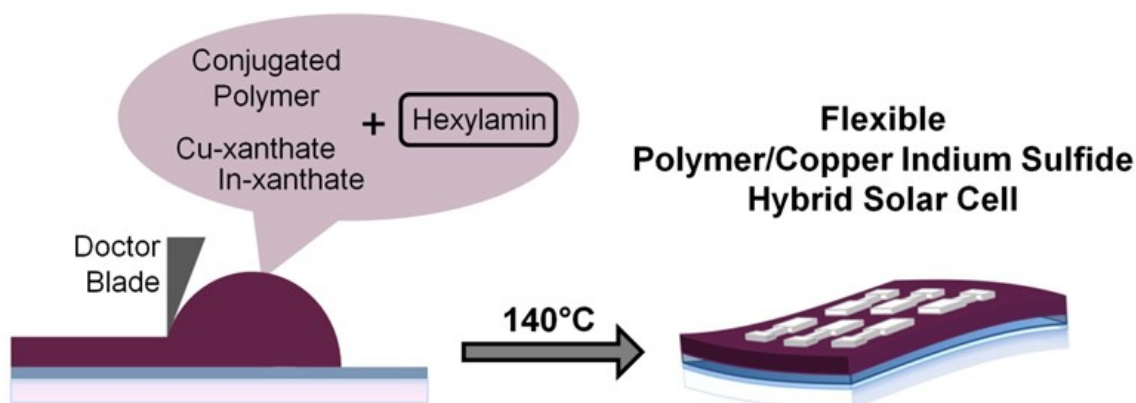


**Figure 58: Schematic depiction of the low-annealing temperature for flexible hybrid polymer/CIS solar cells in the presence of n-hexylamine.**

The second aim was to introduce the inverted architecture to the hybrid polymer/CIS system. This architecture offers the possibility of a high temperature annealing step to form an electron selective interlayer, such titanium oxide, out its precursor material. A suitable method to obtain a smooth titanium oxide interlayer with a suitable layer thickness of about 25 nm was found by doctor blading and a subsequent heating step (Figure 59).

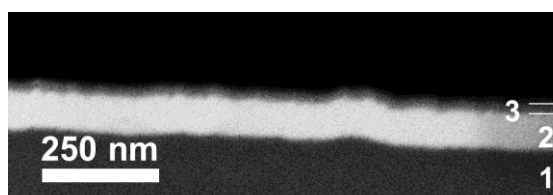


**Figure 59: SEM-BSE cross section image of a titanium oxide layer on glass/ITO substrates prepared via doctor blading and subsequent annealing. 1: glass, 2: ITO, 3: TiO<sub>x</sub> layer**

Based on this titanium oxide layer, inverted hybrid polymer/CIS solar cells of different compositions were fabricated, investigated and compared (Table 6).

<b>Composition</b>	<b>V<sub>oc</sub> / mV</b>	<b>I<sub>sc</sub> / mA/cm<sup>2</sup></b>	<b>FF / %</b>	<b>PCE / %</b>
ITO/TiO <sub>x</sub> /HL/Au	236 ± 18	5,30 ± 0,27	29,5 ± 0,9	0,36 ± 0,04
ITO/TiO <sub>x</sub> /CIS/HL/Au	292 ± 20	3,94 ± 0,32	25,7 ± 2,4	0,30 ± 0,04
ITO/TiO <sub>x</sub> /CdS/HL/Au	386 ± 8	6,39 ± 0,49	46,3 ± 1,3	1,13 ± 0,07
ITO/TiO <sub>x</sub> /CdS/HL/PEDOT:PSS/Ag	549 ± 45	7,95 ± 0,23	33,3 ± 2,1	1,45 ± 0,11

**Table 6: Comparison of the characteristic photovoltaic parameters of the different inverted hybrid solar cell constructions (mean values of each best ten cells are given).**

Concurrent use of a CdS interlayer at the cathode side and a PEDOT:PSS interlayer at the anode side turned out to lead to the best performance. With this construction efficiencies of up to 1.6% were reached.

In the context of these experiments a photo-annealing effect was observed and consequently investigated. The solar cells, which were exposed to oxygen and humidity, exhibited an I-V curve with an inflection point in the

4<sup>th</sup> quadrant immediately after their fabrication. This unfavorable kink could be removed by storage under inert conditions and especially by exposing the cell to a light soaking step. This light soaking effect is illustrated by a comparison of the respective I-V curves, which is given in Figure 60.

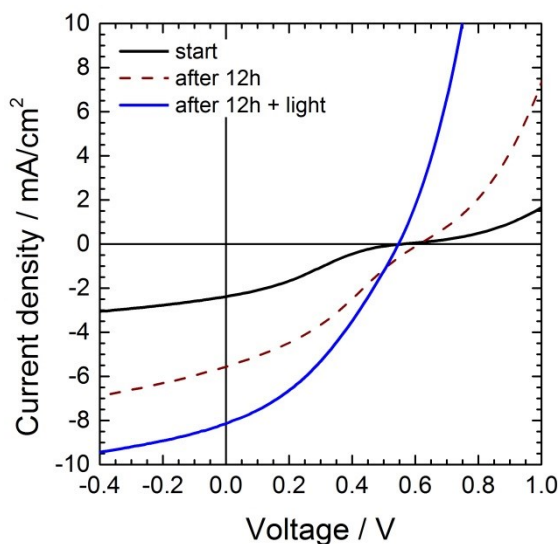


**Figure 60: Light soaking effect on inverted hybrid polymer/CIS solar cells that were fabricated at ambient conditions.**

The inflection point behavior is attributed to an energy barrier resulting from a poor carrier transport in one of the layers or at one of the interfaces. Therefore charge extraction is prevented [142]. The photo-annealing step might then increase the photoconductivity of the titanium oxide interlayer and further support the oxygen redistribution process within the cell. A much weaker but still significant photo-annealing effect was detected for inverted hybrid solar cells of another construction type, which were not objected to oxygen and humidity during their fabrication. This confirms that light soaking has a positive influence on the conductivity of the metal oxide interlayer. This effect is mainly attributed to UV-light [142]. The removal of the inflection point by photo-annealing was observed to be at

least somehow reversible if the solar cell is stored in the dark, but it turned out that the reappeared inflection point can again be removed by a further light soaking step.

The third goal that was covered in this thesis was dealing with fabrication of highly ordered vertically aligned structures of copper indium sulfide. Again copper- and indium-xanthates were used as precursor material for the formation of the CIS structures. However, in this case the conversion process was not thermally induced, but promoted by extreme UV-illumination. More precisely the extreme UV-illumination was done through a shadow mask, whereby only the illuminated areas were cured and became insoluble due to the formation of the metal sulfide. The non-illuminated areas remained soluble and could thus be easily removed by briefly dipping the substrate into an organic solvent.

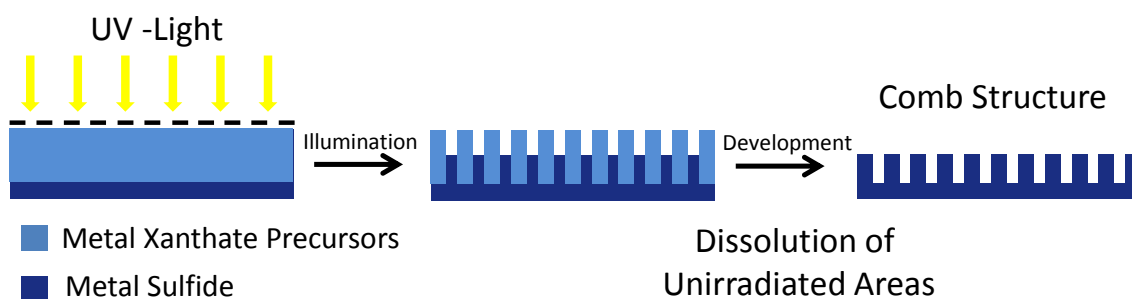


**Figure 61: Schematic illustration of the photolithographic process for the preparation of metal sulfide comb structures from metal xanthates.**

Figure 61 illustrates the principle of this photolithographic structuring process, which offers the possibility for the formation of structured metal sulfide layers via a photochemically induced solid state reaction. In order to obtain a comb structure after the photolithographic structuring process a continuous CIS layer was first applied by thermal conversion of the respective metal xanthates.

To obtain structures at the nanoscale, interference lithography was used. Consequently impressively homogeneous column-like structures with periodicities of 283 nm and 141 nm and a height of about 29-35 nm could be achieved (Figure 62).

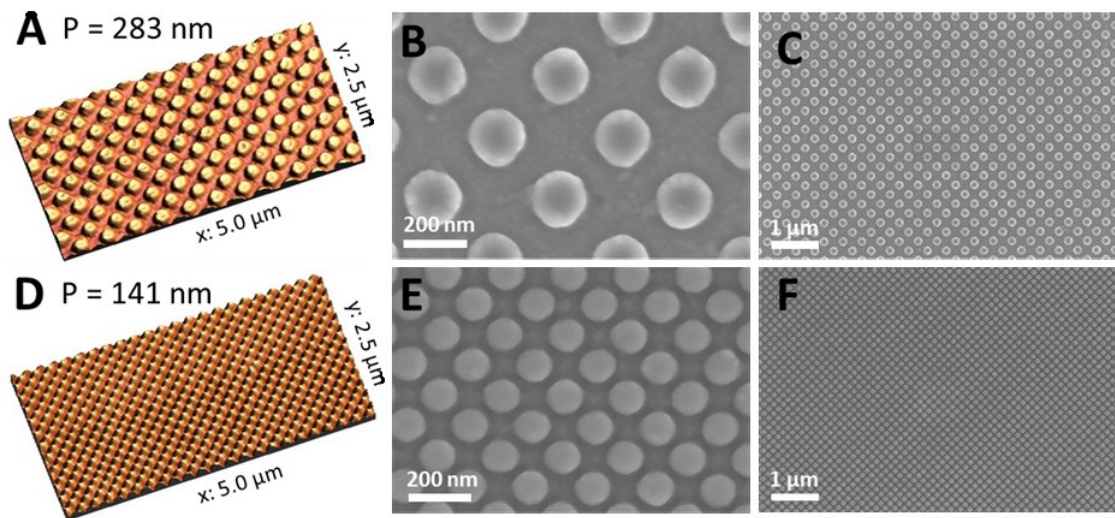


**Figure 62: AFM images (A, D) and SEM-SE micrographs (B, C, E, F) with different magnifications of copper indium sulfide column structures with periodicities of 283 nm (A-C) and 141 nm (D-F) prepared via four-beam interference (Ref. [84]).**

The above shown column structures were obtained via four-beam interference. With two-beam interference, comb structures could be obtained at the cost of having only half the illumination intensity. We avoided very long exposure times by using ASFMs masks, where in contrast to interference masks, all transmitted light contributes to image formation. Thereby CIS comb structures with a periodicity of 280 nm and a height of 25 nm could be successfully prepared (Figure 63).

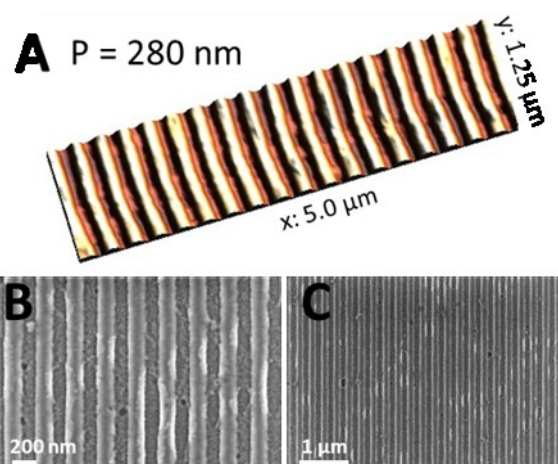


**Figure 63: AFM image (A) and SEM-SE micrographs (B, C) with different magnifications of copper indium sulfide comb structures with a periodicity of 280 nm and a structure height of 25 nm (Ref. [84]).**

## 2 Outlook

The presented highly ordered nanostructures of an acceptor phase material, CIS, are perfectly suited to be infiltrated by an organic polymer in order to form an inverted hybrid layer for photovoltaic applications. The finer these structures are, the bigger the donor-acceptor interface in the respective hybrid PV cell, leading to high efficient charge dissociation and transport. The periodicity of 140 nm that was obtained is already very promising. Further work should concentrate on the application of these structures in inverted hybrid solar cells.

The low-temperature annealing method suddenly offers the possibility to produce flexible hybrid polymer/CIS solar cells with efficiencies which could only be obtained on glass substrates until now, as the performance disadvantage at 140 °C is almost completely compensated by the addition of n-hexylamine. Further investigations could concentrate in more detail on the optimum amount of n-hexylamine, which is added to the

polymer/CIS precursor solution. Within the scope of this work, some tests on different concentrations were done, but there might be still room for improvement if a detailed study is executed. Moreover, knowledge about the mode of operation might be the basis for novel synthesis routes of metal sulfide precursors with the involvement of n-hexylamine in order to reach faster decomposition characteristics at lower temperatures and thus even reach higher efficiencies.

The investigations on the inverted architecture for polymer/CIS solar cells were very extensive already. Nevertheless, a more detailed investigation on the role of the CdS interlayer would be interesting and might give information on the not given applicability of CIS as electron selective interlayer. A further performance improvement of inverted polymer/CIS hybrid solar cells could result from a combination with the experiments on n-hexylamine.

# **CHAPTER VIII**

## **APPENDIX**



## 1 List of Abbreviations

a.u.	arbitrary units
ABL	anode buffer layer
AM	air mass
BHJ	bulk heterojunction
c	speed of light
CB	conduction band
CB	chlorobenzene
CBL	cathode buffer layer
CIS	copper indium sulfide
CIS	copper indium sulfide
$d_L$	layer thickness
e	elementary charge
EQE	external quantum efficiency
$\epsilon_r$	Relative permittivity
FF	fill factor
h	planck constant
HL	hybrid layer
HOMO	highest occupied molecule orbital
$I_{mpp}$	current at the maximum power point
IPCE	incident photon to current efficiency

I <sub>sc</sub>	short circuit current
ITO	indium tin oxide
l <sub>diff</sub>	diffusion length
LUMO	lowest unoccupied molecule orbital
NIL	nanoimprint lithography
OPV	organic photovoltaics
P3HT	Poly(3-hexylthiophene-2,5-diyl)
PCBM	[6,6]-phenyl-C61-butyric acid methyl ester
PCBM(C70)	[6,6]-phenyl-C71-butyric acid methyl ester
PCDTBT	poly[[9-(1-octylnonyl)-9H-carbazole-2,7-diyl]-2,5-thiophenediyl-2,1,3-benzothiadiazole-4,7-diyl-2,5-thiophenediyl]
PCE	power conversion efficiency
PEDOT	poly(3,4-ethylenedioxythiophene)
PEDOT:PSS	Poly(3,4-ethylenedioxythiophene) : poly(styrenesulfonate)
PET	polyethylene terephthalate
P <sub>in</sub>	Incident light power
P <sub>max</sub>	maximum power point
PSiF-DBT	poly[(2,7-silafluorene)-alt-(4,7-di-2-thienyl-2,1,3-benzothiadiazole)]
PSS	poly(styrene sulfonic acid)
PV	photovoltaic(s)
R <sub>max</sub>	maximum surface roughness
SEM	scanning electron microscopy

---

TEM	transmission electron microscopy
VB	valence band
$V_{\text{mpp}}$	voltage at the maximum power point
$V_{\text{oc}}$	open circuit voltage
XRD	x-ray diffraction
$\Delta E_{\text{ES}}$	energy offset of the ground states of donor and acceptor
$\Delta E_{\text{GS}}$	energy offset of the excited states of donor and acceptor
$\eta$	efficiency
$\theta$	angle (x-ray diffraction)
$\lambda$	wavelength
$\sigma$	standard deviation

## 2 List of Tables

Table 1:	Influence of n-hexylamine on the performance of PCDTBT/CIS solar cells at different annealing temperatures (mean values of each best ten cells are given).	46
Table 2:	Influence of n-hexylamine on the performance of PSiFDBT/CIS solar cells at different annealing temperatures (mean values of each best ten cells are given).	68
Table 3:	Influence of n-hexylamine on the performance of PCDTBT/CIS solar cells at 140 °C (mean values of each best ten cells are given); V <sub>2</sub> O <sub>5</sub> was used as ABL.	72
Table 4:	Summary and comparison of the characteristic photovoltaic parameters of the investigated types of inverted hybrid solar cell construction (mean values of each best ten cells are given).	87
Table 5:	Assignment of the peaks of the Cu- and In-xanthate precursor layer in the FT-IR spectra [177,178] (Ref. [84]).	109
Table 6:	Comparison of the characteristic photovoltaic parameters of the different inverted hybrid solar cell constructions (mean values of each best ten cells are given).	117

### 3 List of Figures

- Figure 1: Development of the world population since 1950. Data taken from Ref [2]. 3
- Figure 2: Estimated renewable energy share of global final energy consumption, 2011. Data taken from Ref [4]. 4
- Figure 3: Growth rates of renewable energy technologies in 2012. Data taken from Ref [4]. 5
- Figure 4: Global capacity of solar photovoltaics. Data taken from Ref [4]. 6
- Figure 5: A “World Power Map”, which shows that Europe is leading the way on the PV market at the moment (data from 2012 was used). © by the European Photovoltaic Industry Association (Ref. [11]). 6
- Figure 6: Loss mechanisms in a standard solar cell. 1) thermalization of photons exceeding the bandgap; 2) non-absorption of photons below the bandgap; 3) recombination of the charges; 4) junction loss; 5) contact loss 9
- Figure 7: NREL efficiency chart [33]. Watch the rapid progress of OPV (depicted as red dots) within the last 10 years. 13
- Figure 8: The critical triangle for PV. All types of new generation solar cells have to fulfil the three requirements, lifetime, efficiency and costs, simultaneously; otherwise they will not be able to compete with established PV technologies [36]. 14
- Figure 9: Chemical structures of the used CIS-precursor materials:  
 a) copper O-2,2-dimethylpentan-3-yl dithiocarbonate  
 b) indium O-2,2-dimethylpentan-3-yl dithiocarbonate 17

- Figure 10: Schematic depiction of the hybrid layer formation process via the *in situ* xanthate route. 18
- Figure 11: Scheme of the energy generation process in a hybrid solar cell for photons absorbed by the organic donor phase. Substeps of the energy conversion process: 1) light absorption, 2) exciton generation, 3) exciton diffusion, 4) charge separation, 5) charge transport, 6) charge collection. Photon absorption by the inorganic phase is neglected for clarity. 21
- Figure 12: black: solar spectrum AM 1.5 (global tilt); green: absorption spectrum a typical inorganic semiconductor (CIS); red: absorption spectrum of a typical low bandgap polymer (PSiF-DBT) 23
- Figure 13: General energy band diagram of a hybrid solar cell [53]. 25
- Figure 14: Schematic depiction of the energy conversion process 28
- Figure 15: Schematic depiction of a bilayer heterojunction architecture and a bulk heterojunction architecture. 29
- Figure 16: Schematic depiction of a structured heterojunction architecture. 32
- Figure 17: Depiction of an idealized nanostructured architecture in hybrid solar cells. 33
- Figure 18: Scheme of a typical J-V curve of a hybrid solar cell, with its characteristic parameters. 34
- Figure 19: I-V curves under illumination (100 mW/cm<sup>2</sup>) of PCDTBT/CIS solar cells prepared at annealing temperatures of (a) 140 °C and (b) 195 °C with and without hexylamine (Ref. [85]). 47

- Figure 20: (a) EQE spectra of the hybrid solar cells prepared in presence and absence of n-hexylamine at 140 °C and 195 °C in comparison to (b) the absorption spectra of the respective nanocomposite layer (Ref. [85]). 48
- Figure 21: Transmission electron microscopy images of PCDTBT/CIS nanocomposite layers prepared at 140 °C and 195 °C (Ref. [85]). 50
- Figure 22: X-ray diffraction measurements showing the influence of n-hexylamine during the thin film preparation on the crystallinity of the nanocomposite films as a function of the annealing temperature; (a) 140 °C, (b) 195 °C; (c) reference pattern for CuInS<sub>2</sub> (PDF-27-159) (Ref. [85]). 52
- Figure 23: Thermogravimetric analysis of PCDTBT/CIS precursor material with and without n-hexylamine (Ref. [85]). 53
- Figure 24: High resolution mass spectrum (EI-DI) acquired during the thermal decomposition of the precursor material with n-hexylamine at a temperature of the DI probe of approx. 115 °C (Ref. [85]). 54
- Figure 25: I-V curves of a flexible PCDTBT/CIS:HA hybrid solar cell (Ref. [85]). 57
- Figure 26: (a) Picture of a PCDTBT/CIS:HA hybrid solar cell module on a glass/ITO substrate and (b) the corresponding I-V curves. (c) Picture of a flexible PCDTBT/CIS:HA hybrid solar cell module on a PET/ITO substrate and (d) the corresponding I-V curves (Ref. [85]). 59
- Figure 27: Comparison of the stability of PCDTBT/CIS nanocomposite solar cells prepared with n-hexylamine annealed at (a) 195 °C and at (b) 140 °C (Ref. [85]). 61

- Figure 28: Chemical structures of (a) copper O-2,2-dimethylpentan-3-yl dithiocarbonate, (b) indium O-2,2-dimethylpentan-3-yl dithiocarbonate and (c) PCDTBT (Ref. [85]). 63
- Figure 29: Dependency of the characteristic solar cell parameters of low temperature annealed (140 °C) PCDTBT/CIS:HA solar cells on the annealing time. The average values of 10 cells are depicted. No significant difference could be detected (Ref. [85]). 64
- Figure 30: Geometries of the prepared hybrid solar cell modules on glass (A) and on flexible PET substrates (B) (Ref. [85]). 65
- Figure 31: Chemical structure of the conjugated Polymer PSiF-DBT 67
- Figure 32: I-V curves of PSiF-DBT/CIS solar cells prepared at (a) 140 °C and (b) 195 °C with and without hexylamine. 69
- Figure 33: Chemical Structure of PEDOT:PSS 71
- Figure 34: I-V curves of PCDTBT/CIS solar cells prepared at 140 °C with and without hexylamine; V<sub>2</sub>O<sub>5</sub> was used as ABL. 73
- Figure 35: Schematic comparison of the architecture and the electrical cycle in (a) a normal hybrid solar cell and (b) an inverted hybrid solar cell. 75
- Figure 36: Chemical structure of Dynol 604 Surfactant 79
- Figure 37: Chemical structure of diisopropoxytitanium bis(acetylacetonate). 80
- Figure 38: SEM-BSE cross section image of a titanium oxide layer on glass/ITO substrates prepared via spray pyrolysis. 1: glass, 2: ITO, 3: TiO<sub>x</sub> layer 81
- Figure 39: SEM-BSE cross section image of a titanium oxide layer on glass/ITO substrates prepared via doctor blading and subsequent annealing. 1: glass, 2: ITO, 3: TiO<sub>x</sub> layer 82



- Figure 40: (a) I-V curve and (b) a schematic depiction of a simple inverted hybrid solar cell. The I-V data was obtained after a photo-annealing step, which is explained in detail on page 88 et seq. 83
- Figure 41: (a) I-V curve comparison to show the effect of a CIS interlayer and (b) a schematic depiction of an inverted hybrid solar cell with a CIS interlayer. The I-V data was obtained after a photo-annealing step, which is explained in detail on page 88 et seq. 84
- Figure 42: (a) I-V curve comparison to show the effect of a CdS interlayer and (b) a schematic depiction of an inverted hybrid solar cell with a CdS interlayer. The I-V data was obtained after a photo-annealing step, which is explained in detail on page 88 et seq. 85
- Figure 43: (a) I-V curve comparison to show the effect of a PEDOT:PSS interlayer and (b) a schematic depiction of the most effective inverted hybrid solar cell construction. The I-V data was obtained after a photo-annealing step, which is explained in detail on page 88 et seq. 87
- Figure 44: Light soaking effect on the PCE of inverted hybrid polymer/CIS solar cells with and without a PEDOT:PSS interlayer. 89
- Figure 45: Light soaking effect on inverted hybrid polymer/CIS solar cells (a) with a PEDOT:PSS interlayer (fabricated at ambient conditions) and (b) without a PEDOT:PSS interlayer (fabricated at inert conditions). 89
- Figure 46: Re-appearance and repeated removal of the inflection point. Solar cell construction: ITO/TiO<sub>x</sub>/CdS/HL/PEDOT:PSS/Ag 92

- Figure 47: A) FT-IR spectra of a metal xanthate precursor layer before and after 20 min UV-illumination under reduced pressure; B) SAED image and the corresponding radial intensity profile of the UV-illuminated sample (Ref. [84]). 99
- Figure 48: XPS spectra of the elements Cu (A), In (B) and S (C) in the precursor film (black), after thermal annealing (red) and after UV-treatment (blue) (Ref. [84]). 100
- Figure 49: Schematic illustration of the photolithographic process for the preparation of metal sulfide comb structures from metal xanthates (Ref. [84]). 101
- Figure 50: AFM images (A, D) and SEM-SE micrographs (B, C, E, F) with different magnifications of copper indium sulfide column structures with periodicities of 283 nm (A-C) and 141 nm (D-F) prepared via four-beam interference. The height of the structures is about 29-35 nm (Ref. [84]). 103
- Figure 51: AFM image (A) and SEM-SE micrographs (B, C) with different magnifications of copper indium sulfide comb structures with a periodicity of 280 nm and a structure height of 25 nm (Ref. [84]). 106
- Figure 52: Chemical structures of the used Cu- and In-xanthates (copper O-2,2-dimethylpentan-3-yl-dithiocarbonate; indium O-2,2-dimethylpentan-3-yl-dithiocarbonate) (Ref. [84]). 109
- Figure 53: Height profiles of the column-structures presented in Figure 50 extracted from the AFM images in the diagonal (A, B) and in x-direction (C, D). For the sample with a periodicity of 282 nm (A, C), the height difference in the structure is about 30-35 nm, for sample P = 141 nm (B, D) it is about 29 nm in x-direction and about 16 nm in the diagonal (Ref. [84]). 110

- Figure 54: Height profile of the comb-structures presented in Figure 51 extracted from the AFM image. The height difference in the structure is about 25 nm (Ref. [84]). 111
- Figure 55: TEM-BF and HR-TEM-BF images of PCDTBT/CIS nanocomposite layers prepared at 140 °C and 195 °C (Ref. [85]). 113
- Figure 56: Schematic depiction of the xanthate decomposition benefitting reaction with n-hexylamine. 114
- Figure 57: I-V curves under illumination (100 mW/cm<sup>2</sup>) of PCDTBT/CIS solar cells prepared at annealing temperatures of (a) 140 °C and (b) 195 °C with and without hexylamine (Ref. [85]). 115
- Figure 58: Schematic depiction of the low-annealing temperature for flexible hybrid polymer/CIS solar cells in the presence of n-hexylamine. 116
- Figure 59: SEM-BSE cross section image of a titanium oxide layer on glass/ITO substrates prepared via doctor blading and subsequent annealing. 1: glass, 2: ITO, 3: TiO<sub>x</sub> layer 117
- Figure 60: Light soaking effect on inverted hybrid polymer/CIS solar cells that were fabricated at ambient conditions. 118
- Figure 61: Schematic illustration of the photolithographic process for the preparation of metal sulfide comb structures from metal xanthates. 119
- Figure 62: AFM images (A, D) and SEM-SE micrographs (B, C, E, F) with different magnifications of copper indium sulfide column structures with periodicities of 283 nm (A-C) and 141 nm (D-F) prepared via four-beam interference (Ref. [84]). 120

Figure 63: AFM image (A) and SEM-SE micrographs (B, C) with different magnifications of copper indium sulfide comb structures with a periodicity of 280 nm and a structure height of 25 nm (Ref. [84]).

121

## 4 Bibliography

- [1] L. White, *The Evolution of Culture: The Development of Civilization to the Fall of Rome*, New York: McGraw-Hill Book, **1959**, 56.
- [2] United Nations Department of Economic and Social Affairs/Population Division, "World Population Prospects - The 2012 Revision", New York, **2013**, 1–5.
- [3] M. Golušin, S. Dodić and S. Popov, *Sustainable Energy Management*, Boston: Academic Press, **2013**, 1–6 (doi: 10.1016/B978-0-12-415978-5.00001-1).
- [4] Dennis Mcginn, David Green, Rainer Hinrichs-Rahlwes, Steve Sawyer, Marietta Sander, Richard Taylor, Irene Giner-Reichl, Sven Teske, Harry Lehmann and David Hales, "Renewables 2013 Global Status Report", **2013**.
- [5] International Energy Agency, "World Energy Outlook", Paris, **2012**.
- [6] International Energy Agency, "World Energy Outlook", Paris, **2013**.
- [7] K. E. Trenberth, A. Dai, R. M. Rasmussen and D. B. Parsons, "The Changing Character of Precipitation", *Bulletin of the American Meteorological Society* **2003**, 84, 1205–1217 (doi: 10.1175/BAMS-84-9-1205).
- [8] P. C. D. Milly, R. T. Wetherald, K. a Dunne and T. L. Delworth, "Increasing risk of great floods in a changing climate.", *Nature* **2002**, 415, 514–517 (doi: 10.1038/415514a).

- [9] V. Petoukhov, S. Rahmstorf, S. Petri and H. Joachim, "Quasiresonant amplification of planetary waves and recent Northern Hemisphere weather extremes", *Proceedings of the National Academy of Sciences of the United States of America* **2013**, *110*, 5336–5341 (doi: 10.1073/pnas.1222000110/-/DCSupplemental.www.pnas.org/cgi/doi/10.1073/pnas.1222000110).
- [10] International Energy Agency, "World Energy Outlook", Paris, **2007**, 74.
- [11] European Photovoltaic Industry Association, "Global Market Outlook for Photovoltaics 2013-2017", **2013**.
- [12] European Photovoltaic Industry Association, "Unlocking the Sunbelt Potential of Photovoltaics", **2010**.
- [13] W. Shockley and H. J. Queisser, "Detailed Balance Limit of Efficiency of p-n Junction Solar Cells", *Journal of Applied Physics* **1961**, *32*, 510–519 (doi: 10.1063/1.1736034).
- [14] G. Conibeer, "Third-generation photovoltaics", *Materials Today* **2007**, *10*, 42–50.
- [15] J. Zhao, A. Wang, M. A. Green, F. Ferrazza and V. A. D. Andrea, "19.8% efficient "honeycomb" textured multicrystalline and 24.4% monocrystalline silicon solar cells", *Applied Physics Letters* **1998**, *73*, 1991–1993.
- [16] M. A. Green, K. Emery, Y. Hishikawa, W. Warta and E. D. Dunlop, "Solar cell efficiency tables (version 42)", *Progress in Photovoltaics* **2013**, *21*, 827–837 (doi: 10.1002/pip).

- [17] S. Benagli, D. Borrello, E. Vallat-Sauvain, J. Meier, U. Kroll, J. Hoetzel, J. Bailat, J. Steinhauser, M. Marmelo, G. Monteduro and L. Castens, "High-efficiency amorphous silicon devices on LPCVD-ZNO TCO prepared in industrial KAI™-M R&D reactor", *Preprint of the 24 th European Photovoltaic Solar Energy Conference & Exhibition*, Hamburg, **2009**.
- [18] S. Hänni, G. Bugnon, G. Parascandolo, M. Boccard, J. Escarré, M. Despeisse, F. Meillaud and C. Ballif, "High-efficiency microcrystalline silicon single-junction solar cells", *Progress in Photovoltaics* **2013**, *21*, 821–826 (doi: 10.1002/pip).
- [19] I. Repins, M. A. Contreras, B. Egaas, C. DeHart, J. Scharf, C. L. Perkins, B. To and R. Noufi, "19.9%-efficient ZnO/CdS/CuInGaSe<sub>2</sub> solar cell with 81.2% fill factor", *Progress in Photovoltaics: Research and Applications* **2008**, *16*, 235–239 (doi: 10.1002/pip.822).
- [20] Empa - Swiss Federal Laboratories for Materials Science and Technology, "Flexible C.I.G.S. solar cell reaches 20.4 percent efficiency", <http://www.ecoseed.org/renewables/solar/16007-flexible-c-i-g-s-solar-cell-reaches-20-4-percent-efficiency-empa> (accessed on 01/07/**2014**).
- [21] M. a Green, "Third generation photovoltaics: solar cells for 2020 and beyond", *Physica E: Low-dimensional Systems and Nanostructures* **2002**, *14*, 65–70 (doi: 10.1016/S1386-9477(02)00361-2).

- [22] A. Marti and G. L. Arafijo, "Limiting efficiencies for photovoltaic energy conversion in multigap systems", *Solar Energy Materials & Solar Cells* **1996**, 43, 203–222.
- [23] D.-H. Cho, Y.-D. Chung, K.-S. Lee, K.-H. Kim, J.-H. Kim, S.-J. Park and J. Kim, "Photovoltaic performance of flexible Cu(In,Ga)Se<sub>2</sub> thin-film solar cells with varying Cr impurity barrier thickness", *Current Applied Physics* **2013**, 13, 2033–2037 (doi: 10.1016/j.cap.2013.09.005).
- [24] G. Azzouzi and W. Tazibt, "Improving Silicon Solar Cell Efficiency by Using the Impurity Photovoltaic Effect", *Energy Procedia* **2013**, 41, 40–49 (doi: 10.1016/j.egypro.2013.09.005).
- [25] R. R. King, D. C. Law, K. M. Edmondson, C. M. Fetzer, G. S. Kinsey, H. Yoon, R. a. Sherif and N. H. Karam, "40% efficient metamorphic GaInP/GaInAs/Ge multijunction solar cells", *Applied Physics Letters* **2007**, 90, 183516 (doi: 10.1063/1.2734507).
- [26] P. Würfel, "Solar energy conversion with hot electrons from impact ionisation", *Solar Energy Materials & Solar Cells* **1997**, 46, 43–52.
- [27] H. Spanggaard and F. C. Krebs, "A brief history of the development of organic and polymeric photovoltaics", *Solar Energy Materials and Solar Cells* **2004**, 83, 125–146 (doi: 10.1016/j.solmat.2004.02.021).
- [28] C.-F. Lin, W.-F. Su, C.-I. Wu and I.-C. Cheng, *Organic, Inorganic and Hybrid Solar Cells: Principles and Practice*, Wiley-IEEE Press, **2012**.



- [29] F. C. Krebs, "Fabrication and processing of polymer solar cells: A review of printing and coating techniques", *Solar Energy Materials & Solar Cells* **2009**, 93, 394–412 (doi: 10.1016/j.solmat.2008.10.004).
- [30] G. Li, R. Zhu and Y. Yang, "Polymer solar cells", *Nature Photonics* **2012**, 6, 153–161.
- [31] Heliatek - Press Release, "Heliatek consolidates its technology leadership by establishing a new world record for organic solar technology with a cell efficiency of 12%", [http://www.heliatek.com/newscenter/latest\\_news/neuer-weltrekord-fur-organische-solarzellen-heliatek-behauptet-sich-mit-12-zelleffizienz-als-technologiefuehrer/?lang=en](http://www.heliatek.com/newscenter/latest_news/neuer-weltrekord-fur-organische-solarzellen-heliatek-behauptet-sich-mit-12-zelleffizienz-als-technologiefuehrer/?lang=en) (accessed on 01/07/**2014**).
- [32] M. Jørgensen, J. E. Carlé, R. R. Søndergaard, M. Lauritzen, N. a. Dagnæs-Hansen, S. L. Byskov, T. R. Andersen, T. T. Larsen-Olsen, A. P. L. Böttiger, B. Andreasen, L. Fu, L. Zuo, Y. Liu, E. Bundgaard, X. Zhan, H. Chen and F. C. Krebs, "The state of organic solar cells—A meta analysis", *Solar Energy Materials and Solar Cells* **2013**, 119, 84–93 (doi: 10.1016/j.solmat.2013.05.034).
- [33] NREL, "Best Research-Cell Efficiencies", [http://www.nrel.gov/ncpv/images/efficiency\\_chart.jpg](http://www.nrel.gov/ncpv/images/efficiency_chart.jpg) (accessed on 01/12/**2014**).

- [34] S. A. Gevorgyan, A. J. Medford, E. Bundgaard, S. B. Sapkota, H.-F. Schleiermacher, B. Zimmermann, U. Würfel, A. Chafiq, M. Lira-Cantu, T. Swonke, M. Wagner, C. J. Brabec, O. Haillant, E. Voroshazi, T. Aernouts, R. Steim, J. A. Hauch, A. Elschner, M. Pannone, M. Xiao, A. Langzettel, D. Laird, M. T. Lloyd, T. Rath, E. Maier, G. Trimmel, M. Hermenau, T. Menke, K. Leo, R. Rösch, M. Seeland, H. Hoppe, T. J. Nagle, K. B. Burke, C. J. Fell, D. Vak, T. B. Singh, S. E. Watkins, Y. Galagan, A. Manor, E. A. Katz, T. Kim, K. Kim, P. M. Sommeling, W. J. H. Verhees, S. C. Veenstra, M. Riede, M. Greyson Christoforo, T. Currier, V. Shrotriya, G. Schwartz and F. C. Krebs, "An inter-laboratory stability study of roll-to-roll coated flexible polymer solar modules", *Solar Energy Materials and Solar Cells* **2011**, 95, 1398–1416 (doi: 10.1016/j.solmat.2011.01.010).
- [35] D. M. Tanenbaum, M. Hermenau, E. Voroshazi, M. T. Lloyd, Y. Galagan, B. Zimmermann, M. Hösel, H. F. Dam, M. Jørgensen, S. A. Gevorgyan, S. Kudret, W. Maes, L. Lutsen, D. Vanderzande, U. Würfel, R. Andriessen, R. Rösch, H. Hoppe, G. Teran-Escobar, M. Lira-Cantu, A. Rivaton, G. Y. Uzunoglu, D. Germack, B. Andreasen, M. V. Madsen, K. Norrman and F. C. Krebs, "The ISOS-3 inter-laboratory collaboration focused on the stability of a variety of organic photovoltaic devices", *RSC Advances* **2012**, 2, 882 (doi: 10.1039/c1ra00686j).
- [36] C. J. Brabec, "Organic photovoltaics: technology and market", *Solar Energy Materials and Solar Cells* **2004**, 83, 273–292 (doi: 10.1016/j.solmat.2004.02.030).

- [37] B. R. Saunders and M. L. Turner, "Nanoparticle-polymer photovoltaic cells", *Advances in colloid and interface science* **2008**, *138*, 1–23 (doi: 10.1016/j.cis.2007.09.001).
- [38] T. Rath and G. Trimmel, "In situ syntheses of semiconducting nanoparticles in conjugated polymer matrices and their application in photovoltaics", *Hybrid Materials* **2013**, *1*, 15–36 (doi: 10.2478/hyma-2013-0003).
- [39] Y. Zhou, M. Eck, C. Veit, B. Zimmermann, F. Rauscher, P. Niyamakom, S. Yilmaz, I. Dumsch, S. Allard and U. Scherf, "Efficiency enhancement for bulk-heterojunction hybrid solar cells based on acid treated CdSe quantum dots and low bandgap polymer PCPDTBT", *Solar Energy Materials and Solar Cells* **2011**, *95*, 1232–1237 (doi: 10.1016/j.solmat.2010.12.041).
- [40] D. Celik, M. Krueger, C. Veit, H. F. Schleiermacher, B. Zimmermann, S. Allard, I. Dumsch, U. Scherf, F. Rauscher and P. Niyamakom, "Performance enhancement of CdSe nanorod-polymer based hybrid solar cells utilizing a novel combination of post-synthetic nanoparticle surface treatments", *Solar Energy Materials and Solar Cells* **2012**, *98*, 433–440 (doi: 10.1016/j.solmat.2011.11.049).
- [41] N. C. Nicolaidis, B. S. Routley, J. L. Holdsworth, W. J. Belcher, X. Zhou and P. C. Dastoor, "Fullerene Contribution to Photocurrent Generation in Organic Photovoltaic Cells", *The Journal of Physical Chemistry C* **2011**, *115*, 7801–7805 (doi: 10.1021/jp2007683).

- [42] S. Dayal, N. Kopidakis, D. C. Olson, D. S. Ginley and G. Rumbles, "Photovoltaic devices with a low band gap polymer and CdSe nanostructures exceeding 3% efficiency.", *Nano letters* **2010**, *10*, 239–242 (doi: 10.1021/nl903406s).
- [43] A. Guchhait, A. K. Rath and A. J. Pal, "To make polymer: Quantum dot hybrid solar cells NIR-active by increasing diameter of PbS nanoparticles", *Solar Energy Materials and Solar Cells* **2011**, *95*, 651–656 (doi: 10.1016/j.solmat.2010.09.034).
- [44] T. Takagahara and K. Takeda, "Theory of the quantum confinement effect on excitons in quantum dots of indirect-gap materials", *Physical Review B* **1992**, *46*, 15578–15581.
- [45] S. N. Sharma, U. Kumar, T. Vats, M. Arora, V. N. Singh, B. R. Mehta, K. Jain, R. Kakkar and a. K. Narula, "Hybrid organic-inorganic (MEH-PPV/P3HT:CdSe) nanocomposites: linking film morphology to photostability", *The European Physical Journal Applied Physics* **2010**, *50*, 20602 (doi: 10.1051/epjap/2010041).
- [46] H. J. Cortina-Marrero, C. Martínez-Alonso, L. Hechavarria-Difur and H. Hu, "Photovoltaic performance improvement in planar P3HT/CdS solar cells induced by structural, optical and electrical property modification in thermal annealed P3HT thin films", *The European Physical Journal Applied Physics* **2013**, *63*, 10201 (doi: 10.1051/epjap/2013120361).

- [47] B. Vercelli, G. Zotti, a. Berlin and M. Natali, "Self-Assembled Structures of Semiconductor Nanocrystals and Polymers for Photovoltaics. (3) PbSe Nanocrystal–Polymer LBL Multilayers. Optical, Electrochemical, Photoelectrochemical, and Photoconductive Properties", *Chemistry of Materials* **2010**, *22*, 2001–2009 (doi: 10.1021/cm903824e).
- [48] A. H. Khan, U. Thupakula, A. Dalui, S. Maji, A. Debangshi and S. Acharya, "Evolution of Long Range Bandgap Tunable Lead Sulfide Nanocrystals with Photovoltaic Properties", *Journal of Physical Chemistry C* **2013**, *117*, 7934–7939.
- [49] Y. N. Liang, K. Yu, Q. Yan and X. Hu, "Colloidal CuInSe<sub>2</sub> nanocrystals: from gradient stoichiometry toward homogeneous alloyed structure mediated by conducting polymer P3HT.", *ACS applied materials & interfaces* **2013**, *5*, 4100–4106 (doi: 10.1021/am3032212).
- [50] T. Rath, V. Kaltenhauser, W. Haas, A. Reichmann, F. Hofer and G. Trimmel, "Solution-processed small molecule/copper indium sulfide hybrid solar cells", *Solar Energy Materials and Solar Cells* **2013**, *114*, 38–42 (doi: 10.1016/j.solmat.2013.02.024).
- [51] E. Maier, T. Rath, W. Haas, O. Werzer, R. Saf, F. Hofer, D. Meissner, O. Volobujeva, S. Bereznev, E. Mellikov, H. Amenitsch, R. Resel and G. Trimmel, "CuInS<sub>2</sub>–Poly(3-(ethyl-4-butanoate)thiophene) nanocomposite solar cells: Preparation by an in situ formation route, performance and stability issues", *Solar Energy Materials and Solar Cells* **2011**, *95*, 1354–1361 (doi: 10.1016/j.solmat.2010.12.025).

- [52] S. Ren, L.-Y. Chang, S.-K. Lim, J. Zhao, M. Smith, N. Zhao, V. Bulović, M. Bawendi and S. Gradecak, "Inorganic-organic hybrid solar cell: bridging quantum dots to conjugated polymer nanowires", *Nano letters* **2011**, *11*, 3998–4002 (doi: 10.1021/nl202435t).
- [53] M. Wright and A. Uddin, "Organic—inorganic hybrid solar cells: A comparative review", *Solar Energy Materials and Solar Cells* **2012**, *107*, 87–111 (doi: 10.1016/j.solmat.2012.07.006).
- [54] L. X. Reynolds, T. Lutz, S. Dowland, A. MacLachlan, S. King and S. a Haque, "Charge photogeneration in hybrid solar cells: a comparison between quantum dots and in situ grown CdS.", *Nanoscale* **2012**, *4*, 1561–1564 (doi: 10.1039/c2nr12081j).
- [55] S. Dowland, T. Lutz, A. Ward, S. P. King, A. Sudlow, M. S. Hill, K. C. Molloy and S. A. Haque, "Direct growth of metal sulfide nanoparticle networks in solid-state polymer films for hybrid inorganic-organic solar cells", *Advanced Materials* **2011**, *23*, 2739–2744 (doi: 10.1002/adma.201100625).
- [56] T. Rath, M. Edler, W. Haas, A. Fischereder, S. Moscher, A. Schenk, R. Trattnig, M. Sezen, G. Mauthner, A. Pein, D. Meischler, K. Bartl, R. Saf, N. Bansal, S. A. Haque, F. Hofer, E. J. W. List and G. Trimmel, "A Direct Route Towards Polymer/Copper Indium Sulfide Nanocomposite Solar Cells", *Advanced Energy Materials* **2011**, *1*, 1046–1050 (doi: 10.1002/aenm.201100442).
- [57] A. J. Heeger, "Nobel Lecture: Semiconducting and metallic polymers: generation of polymeric materials" **2001**, *73*, 681–700.

- [58] G. Garcia-Belmonte, A. Munar, E. M. Barea, J. Bisquert, I. Ugarte and R. Pacios, "Charge carrier mobility and lifetime of organic bulk heterojunctions analyzed by impedance spectroscopy", *Organic Electronics* **2008**, 9, 847–851 (doi: 10.1016/j.orgel.2008.06.007).
- [59] B. M. Omer, "Optical Properties of MEH-PPV and MEH-PPV/ [6,6]-Phenyl C61-butyric Acid 3-ethylthiophene Ester Thin Films", *Journal of Nano- and Electronic Physics* **2012**, 4, 04006.
- [60] A. Misra, P. Kumar, R. Srivastava, S. K. Dhawan, M. N. Kamalasanan and S. Chandra, "Electrochemical and optical studies of conjugated polymers for three primary colours" **2005**, 43, 921–925.
- [61] S. E. Shaheen, C. J. Brabec, N. S. Sariciftci, F. Padinger, T. Fromherz and J. C. Hummelen, "2.5% Efficient Organic Plastic Solar Cells", *Applied Physics Letters* **2001**, 78, 841–843 (doi: 10.1063/1.1345834).
- [62] D. Mühlbacher, H. Neugebauer, A. Cravino, N. S. Sariciftci, J. K. J. Van Duren, A. Dhanabalan, P. A. Van Hal, R. A. J. Janssen and J. C. Hummelen, "Comparison of electrochemical and spectroscopic data of the low-bandgap polymer ptptb", *Molecular Crystals and Liquid Crystals* **2002**, 385, 85–92 (doi: 10.1080/713738793).
- [63] R. Kroon, M. Lenes, J. C. Hummelen, P. W. M. Blom and B. de Boer, "Small Bandgap Polymers for Organic Solar Cells (Polymer Material Development in the Last 5 Years)", *Polymer Reviews* **2008**, 48, 531–582 (doi: 10.1080/15583720802231833).

- [64] C. Winder and N. S. Sariciftci, "Low bandgap polymers for photon harvesting in bulk heterojunction solar cells", *Journal of Materials Chemistry* **2004**, *14*, 1077 (doi: 10.1039/b306630d).
- [65] E. Bundgaard and F. C. Krebs, "Low band gap polymers for organic photovoltaics", *Solar Energy Materials and Solar Cells* **2007**, *91*, 954–985 (doi: 10.1016/j.solmat.2007.01.015).
- [66] W. Cai, X. Gong and Y. Cao, "Polymer solar cells: Recent development and possible routes for improvement in the performance", *Solar Energy Materials and Solar Cells* **2010**, *94*, 114–127 (doi: 10.1016/j.solmat.2009.10.005).
- [67] T. Ameri, G. Dennler, C. Waldauf, P. Denk, K. Forberich, M. C. Scharber, C. J. Brabec and K. Hingerl, "Realization, characterization, and optical modeling of inverted bulk-heterojunction organic solar cells", *Journal of Applied Physics* **2008**, *103*, 1–6 (doi: 10.1063/1.2902804).
- [68] H. K. Kodali and B. Ganapathysubramanian, "Sensitivity analysis of current generation in organic solar cells—comparing bilayer, sawtooth, and bulk heterojunction morphologies", *Solar Energy Materials and Solar Cells* **2013**, *111*, 66–73 (doi: 10.1016/j.solmat.2012.12.004).
- [69] Y. Liang, Y. Wu, D. Feng, S.-T. Tsai, H.-J. Son, G. Li and L. Yu, "Development of new semiconducting polymers for high performance solar cells.", *Journal of the American Chemical Society* **2009**, *131*, 56–57 (doi: 10.1021/ja808373p).



- [70] P. Boland, K. Lee and G. Namkoong, "Device optimization in PCPDTBT:PCBM plastic solar cells", *Solar Energy Materials and Solar Cells* **2010**, 94, 915–920 (doi: 10.1016/j.solmat.2010.01.022).
- [71] J. Müller, B. Rech, J. Springer and M. Vanecek, "TCO and light trapping in silicon thin film solar cells", *Solar Energy* **2004**, 77, 917–930 (doi: 10.1016/j.solener.2004.03.015).
- [72] G. Jin, P. I. Widenborg, P. Campbell and S. Varlamov, "Lambertian matched absorption enhancement in PECVD poly-Si thin film on aluminum induced textured glass superstrates for solar cell applications", *Progress in Photovoltaics: Research and Applications* **2010**, 18, 582–589 (doi: 10.1002/pip.981).
- [73] N. S. Sariciftci, L. Smilowitz, A. J. Heeger and F. Wudl, "Photoinduced Electron Transfer from a Conducting Polymer to Buckminsterfullerene", *Science* **1992**, 258, 1474–1476 (doi: 10.1126/science.258.5087.1474).
- [74] C. J. Brabec, S. Gowrisanker, J. J. M. Halls, D. Laird, S. Jia and S. P. Williams, "Polymer-fullerene bulk-heterojunction solar cells.", *Advanced materials* **2010**, 22, 3839–3856 (doi: 10.1002/adma.200903697).
- [75] S. H. Park, A. Roy, S. Beaupre, S. Cho, N. Coates, J. S. Moon, D. Moses, M. Leclerc, K. Lee and A. J. Heeger, "Bulk heterojunction solar cells with internal quantum efficiency approaching 100%", *Nature Photonics* **2009**, 3, 297–302.

- [76] R. N. Marks, J. J. M. Halls, D. D. C. Bradley, R. H. Friend and A. B. Holmes, "The photovoltaic response in poly (p-phenylene vinylene) thin-film devices", *Journal of Physics: Condensed Matter* **1994**, *6*, 1379–1394.
- [77] C. J. Brabec, G. Zerza, G. Cerullo, S. De Silvestri, S. Luzzati, J. C. Hummelen and S. Sariciftci, "Tracing photoinduced electron transfer process in conjugated polymer/fullerene bulk heterojunctions in real time", *Chemical Physics Letters* **2001**, *340*, 232–236.
- [78] V. Mihailetschi, J. Wildeman and P. Blom, "Space-Charge Limited Photocurrent", *Physical Review Letters* **2005**, *94*, 126602 (doi: 10.1103/PhysRevLett.94.126602).
- [79] A. Moliton and J. Nunzi, "Review: How to model the behaviour of organic photovoltaic cells", *Polymer International* **2006**, *55*, 583–600 (doi: 10.1002/pi).
- [80] J. C. Hummelen, B. W. Knight, F. LePeq and F. Wudl, "Preparation and Characterization of Fulleroid and Methanofullerene Derivatives", *Journal of Organic Chemistry* **1995**, *60*, 532–538.
- [81] G. Yu, J. Gao, J. C. Hummelen, F. Wudl and A. J. Heeger, "Polymer Photovoltaic Cells: Enhanced Efficiencies via a Network of Internal Donor-Acceptor Heterojunctions", *Science* **1995**, *270*, 1789–1791 (doi: 10.1126/science.270.5243.1789).
- [82] J. Weickert, R. B. Dunbar, H. C. Hesse, W. Wiedemann and L. Schmidt-Mende, "Nanostructured organic and hybrid solar cells.", *Advanced materials (Deerfield Beach, Fla.)* **2011**, *23*, 1810–1828 (doi: 10.1002/adma.201003991).

- [83] Y. Yang, K. Mielczarek, M. Aryal, A. Zakhidov and W. Hu, "Nanoimprinted polymer solar cell.", *ACS nano* **2012**, *6*, 2877–2892 (doi: 10.1021/nn3001388).
- [84] T. Rath, C. Padeste, M. Vockenhuber, C. Fradler, M. Edler, A. Reichmann, I. Letofsky-Papst, F. Hofer, Y. Ekinici and T. Griesser, "Direct extreme UV-lithographic conversion of metal xanthates into nanostructured metal sulfide layers for hybrid photovoltaics", *Journal of Materials Chemistry A* **2013**, *1*, 11135–11140 (doi: 10.1039/c3ta12592k).
- [85] C. Fradler, T. Rath, S. Dunst, I. Letofsky-Papst, R. Saf, B. Kunert, F. Hofer, R. Resel and G. Trimmel, "Flexible Polymer/Copper Indium Sulfide Hybrid Solar Cells and Modules Based on the Metal Xanthate Route and Low Temperature Annealing", *Solar Energy Materials & Solar Cells*, in press (doi: 10.1016/j.solmat.2014.01.043).
- [86] M. Helgesen, R. Søndergaard and F. C. Krebs, "Advanced materials and processes for polymer solar cell devices", *Journal of Materials Chemistry* **2010**, *20*, 36–60 (doi: 10.1039/b913168j).
- [87] I. Gur, N. A. Fromer, C.-P. Chen, A. G. Kanaras and A. P. Alivisatos, "Hybrid solar cells with prescribed nanoscale morphologies based on hyperbranched semiconductor nanocrystals", *Nano letters* **2007**, *7*, 409–414 (doi: 10.1021/nl062660t).
- [88] C. de Mello Donegá, "Synthesis and properties of colloidal heteronanocrystals", *Chemical Society reviews* **2011**, *40*, 1512–1546 (doi: 10.1039/c0cs00055h).

- [89] F. Gao, S. Ren and J. Wang, "The renaissance of hybrid solar cells: progresses, challenges, and perspectives", *Energy & Environmental Science* **2013**, 6, 2020–2040 (doi: 10.1039/c3ee23666h).
- [90] Y. Zhou, M. Eck and M. Krüger, "Bulk-heterojunction hybrid solar cells based on colloidal nanocrystals and conjugated polymers", *Energy & Environmental Science* **2010**, 3, 1851–1864 (doi: 10.1039/c0ee00143k).
- [91] R. Zhou and J. Xue, "Hybrid polymer-nanocrystal materials for photovoltaic applications", *Chemphyschem: a European journal of chemical physics and physical chemistry* **2012**, 13, 2471–2480 (doi: 10.1002/cphc.201101016).
- [92] B. R. Saunders, "Hybrid polymer/nanoparticle solar cells: preparation, principles and challenges", *Journal of colloid and interface science* **2012**, 369, 1–15 (doi: 10.1016/j.jcis.2011.12.016).
- [93] P. Reiss, E. Couderc, J. De Girolamo and A. Pron, "Conjugated polymers/semiconductor nanocrystals hybrid materials-preparation, electrical transport properties and applications", *Nanoscale* **2011**, 3, 446–489 (doi: 10.1039/c0nr00403k).
- [94] L. Zhao and Z. Lin, "Crafting semiconductor organic-inorganic nanocomposites via placing conjugated polymers in intimate contact with nanocrystals for hybrid solar cells", *Advanced materials (Deerfield Beach, Fla.)* **2012**, 24, 4353–4368 (doi: 10.1002/adma.201201196).

- [95] E. Martínez-Ferrero, J. Albero and E. Palomares, "Materials, Nanomorphology, and Interfacial Charge Transfer Reactions in Quantum Dot/Polymer Solar Cell Devices", *The Journal of Physical Chemistry Letters* **2010**, *1*, 3039–3045 (doi: 10.1021/jz101228z).
- [96] A. J. Moulé, L. Chang, C. Thambidurai, R. Vidu and P. Stroeve, "Hybrid solar cells: basic principles and the role of ligands", *Journal of Materials Chemistry* **2012**, *22*, 2351–2368 (doi: 10.1039/c1jm14829j).
- [97] K. F. Jeltsch, M. Schädel, J.-B. Bonekamp, P. Niyamakom, F. Rauscher, H. W. A. Lademann, I. Dumsch, S. Allard, U. Scherf and K. Meerholz, "Efficiency Enhanced Hybrid Solar Cells Using a Blend of Quantum Dots and Nanorods", *Advanced Functional Materials* **2012**, *22*, 397–404 (doi: 10.1002/adfm.201101809).
- [98] Z. Chen, H. Zhang, X. Du, X. Cheng, X. Chen, Y. Jiang and B. Yang, "From planar-heterojunction to n-i structure: an efficient strategy to improve short-circuit current and power conversion efficiency of aqueous-solution-processed hybrid solar cells", *Energy & Environmental Science* **2013**, *6*, 1597–1603 (doi: 10.1039/c3ee40481a).
- [99] J. Seo, M. J. Cho, D. Lee, A. N. Cartwright and P. N. Prasad, "Efficient heterojunction photovoltaic cell utilizing nanocomposites of lead sulfide nanocrystals and a low-bandgap polymer", *Advanced Materials* **2011**, *23*, 3984–3988 (doi: 10.1002/adma.201101912).

- [100] S. D. Oosterhout, M. M. Wienk, S. S. van Bavel, R. Thiedmann, L. J. A. Koster, J. Gilot, J. Loos, V. Schmidt and R. A. J. Janssen, "The effect of three-dimensional morphology on the efficiency of hybrid polymer solar cells", *Nature Materials* **2009**, 8, 818–824 (doi: 10.1038/nmat2533).
- [101] R. Zhou, R. Stalder, D. Xie, W. Cao, Y. Zheng, Y. Yang, M. Plaisant, P. H. Holloway, K. S. Schanze, J. R. Reynolds and J. Xue, "Enhancing the efficiency of solution-processed polymer:colloidal nanocrystal hybrid photovoltaic cells using ethanedithiol treatment", *ACS nano* **2013**, 7, 4846–4854 (doi: 10.1021/nn305823w).
- [102] Z. Liu, Y. Sun, J. Yuan, H. Wei, X. Huang, L. Han, W. Wang, H. Wang and W. Ma, "High-Efficiency Hybrid Solar Cells Based on Polymer/PbS<sub>x</sub>Se<sub>1-x</sub> Nanocrystals Benefiting from Vertical Phase Segregation", *Advanced materials (Deerfield Beach, Fla.)* **2013**, 25, 5772–5778 (doi: 10.1002/adma.201302340).
- [103] H. C. Leventis, S. P. King, A. Sudlow, M. S. Hill, K. C. Molloy and S. A. Haque, "Nanostructured hybrid polymer-inorganic solar cell active layers formed by controllable in situ growth of semiconducting sulfide networks", *Nano Letters* **2010**, 10, 1253–1258 (doi: 10.1021/nl903787j).
- [104] M. Arar, A. Pein, W. Haas, F. Hofer, K. Norrman, F. C. Krebs, T. Rath and G. Trimmel, "Comprehensive Investigation of Silver Nanoparticle/Aluminum Electrodes for Copper Indium Sulfide/Polymer Hybrid Solar Cells", *The Journal of Physical Chemistry C* **2012**, 116, 19191–19196 (doi: 10.1021/jp306242e).

- [105] M. Jäger, R. Trattnig, M. Postl, W. Haas, B. Kunert, R. Resel, F. Hofer, A. Klug, G. Trimmel and E. J. W. List, "Influence of the bridging atom in fluorene analogue low-bandgap polymers on photophysical and morphological properties of copper indium sulfide/polymer nanocomposite solar cells", *Journal of Polymer Science Part B: Polymer Physics* **2013**, 51, 1400–1410 (doi: 10.1002/polb.23350).
- [106] N. Bansal, F. T. F. O'Mahony, T. Lutz and S. A. Haque, "Solution Processed Polymer-Inorganic Semiconductor Solar Cells Employing  $\text{Sb}_2\text{S}_3$  as a Light Harvesting and Electron Transporting Material", *Advanced Energy Materials* **2013**, 3, 986–990 (doi: 10.1002/aenm.201300017).
- [107] V. Kaltenhauser, T. Rath, M. Edler, A. Reichmann and G. Trimmel, "Exploring polymer/nanoparticle hybrid solar cells in tandem architecture", *RSC Advances* **2013**, 3, 18643–18650 (doi: 10.1039/c3ra43842b).
- [108] N. Bansal, L. X. Reynolds, A. MacLachlan, T. Lutz, R. S. Ashraf, W. Zhang, C. B. Nielsen, I. McCulloch, D. G. Rebois, T. Kirchartz, M. S. Hill, K. C. Molloy, J. Nelson and S. A. Haque, "Influence of Crystallinity and Energetics on Charge Separation in Polymer–Inorganic Nanocomposite Films for Solar Cells", *Scientific Reports* **2013**, 3, 1531 (doi: 10.1038/srep01531).

- [109] S. a. Dowland, L. X. Reynolds, A. MacLachlan, U. B. Cappel and S. a. Haque, "Photoinduced electron and hole transfer in CdS:P3HT nanocomposite films: effect of nanomorphology on charge separation yield and solar cell performance", *Journal of Materials Chemistry A* **2013**, *1*, 13896 (doi: 10.1039/c3ta12962d).
- [110] M. Arar, M. Gruber, M. Edler, W. Haas, F. Hofer, N. Bansal, L. X. Reynolds, S. a Haque, K. Zojer, G. Trimmel and T. Rath, "Influence of morphology and polymer:nanoparticle ratio on device performance of hybrid solar cells-an approach in experiment and simulation.", *Nanotechnology* **2013**, *24*, 484005 (doi: 10.1088/0957-4484/24/48/484005).
- [111] I. Degani, R. Fochi and C. Magistris, "O,S-Dimethyl Carbonodithioate as a Phosgene Substitute for the Preparation of S-Methyl Alkylcarbamothioates and Dialkylcarbamothioates", *Synthesis* **2009**, *22*, 3807–3818 (doi: 10.1055/s-0029-1218117).
- [112] A. Kharkwal, S. Sharma, K. Jain, L. Arora, P. Chawla, A. K. Singh and S. Chand, "Polymeric stabilization of hybrid nanocomposites: a comparison between in situ and ex situ-grown CuInS<sub>2</sub> in poly(3-hexylthiophene) polymer", *Colloid and Polymer Science* **2013**, *291*, 2607–2617 (doi: 10.1007/s00396-013-2967-0).
- [113] M. Jørgensen, K. Norrman and F. C. Krebs, "Stability/degradation of polymer solar cells", *Solar Energy Materials and Solar Cells* **2008**, *92*, 686–714 (doi: 10.1016/j.solmat.2008.01.005).



- [114] S. Kwon, K.-G. Lim, M. Shim, H. C. Moon, J. Park, G. Jeon, J. Shin, K. Cho, T.-W. Lee and J. K. Kim, "Air-stable inverted structure of hybrid solar cells using a cesium-doped ZnO electron transport layer prepared by a sol-gel process", *Journal of Materials Chemistry A* **2013**, *1*, 11802–11808 (doi: 10.1039/c3ta12425h).
- [115] B. Reeja-Jayan and A. Manthiram, "Understanding the improved stability of hybrid polymer solar cells fabricated with copper electrodes.", *ACS applied materials & interfaces* **2011**, *3*, 1492–1501 (doi: 10.1021/am200067d).
- [116] R. Zhou, Y. Zheng, L. Qian, Y. Yang, P. H. Holloway and J. Xue, "Solution-processed, nanostructured hybrid solar cells with broad spectral sensitivity and stability", *Nanoscale* **2012**, *4*, 3507–3514 (doi: 10.1039/c2nr30210a).
- [117] J. Wu, G. Yue, Y. Xiao, J. Lin, M. Huang, Z. Lan, Q. Tang, Y. Huang, L. Fan, S. Yin and T. Sato, "An ultraviolet responsive hybrid solar cell based on titania/poly(3-hexylthiophene)", *Scientific reports* **2013**, *3*, 1283 (doi: 10.1038/srep01283).
- [118] M. Jørgensen, K. Norrman, S. A. Gevorgyan, T. Tromholt, B. Andreasen and F. C. Krebs, "Stability of polymer solar cells", *Advanced materials (Deerfield Beach, Fla.)* **2012**, *24*, 580–612 (doi: 10.1002/adma.201104187).
- [119] R. Roesch, K.-R. Eberhardt, S. Engmann, G. Gobsch and H. Hoppe, "Polymer solar cells with enhanced lifetime by improved electrode stability and sealing", *Solar Energy Materials and Solar Cells* **2013**, *117*, 59–66 (doi: 10.1016/j.solmat.2013.05.013).

- [120] B. L. Groenendaal, F. Jonas, D. Freitag, H. Pielartzik and J. R. Reynolds, "Poly(3,4-ethylenedioxythiophene) and Its Derivatives: Past, Present, and Future", *Advanced Materials* **2000**, 481–494.
- [121] F. C. Krebs (Editor), *Polymer Photovoltaics - A Practical Approach*, Bellingham, Washington: Society of Photo-Optical Instrumentation Engineers, **2008**.
- [122] J. Meyer, K. Zilberberg, T. Riedl and A. Kahn, "Electronic structure of Vanadium pentoxide: An efficient hole injector for organic electronic materials", *Journal of Applied Physics* **2011**, 110, 033710 (doi: 10.1063/1.3611392).
- [123] K. Zilberberg, S. Trost, H. Schmidt and T. Riedl, "Solution Processed Vanadium Pentoxide as Charge Extraction Layer for Organic Solar Cells", *Advanced Energy Materials* **2011**, 1, 377–381 (doi: 10.1002/aenm.201100076).
- [124] V. Shrotriya, G. Li, Y. Yao, C.-W. Chu and Y. Yang, "Transition metal oxides as the buffer layer for polymer photovoltaic cells", *Applied Physics Letters* **2006**, 88, 073508 (doi: 10.1063/1.2174093).
- [125] N. Espinosa, H. F. Dam, D. M. Tanenbaum, J. W. Andreasen, M. Jørgensen and F. C. Krebs, "Roll-to-Roll Processing of Inverted Polymer Solar Cells using Hydrated Vanadium(V)Oxide as a PEDOT:PSS Replacement", *Materials* **2011**, 4, 169–182 (doi: 10.3390/ma4010169).
- [126] R. Po, C. Carbonera, A. Bernardi and N. Camaioni, "The role of buffer layers in polymer solar cells", *Energy & Environmental Science* **2011**, 4, 285 (doi: 10.1039/c0ee00273a).

- [127] C. Noguera, *Physics and Chemistry of Oxide Surfaces*, Cambridge University Press, **1996** (doi: 10.1017/CBO9780511524301).
- [128] T. Kuwabara, T. Nakayama, K. Uozumi, T. Yamaguchi and K. Takahashi, "Highly durable inverted-type organic solar cell using amorphous titanium oxide as electron collection electrode inserted between ITO and organic layer", *Solar Energy Materials and Solar Cells* **2008**, *92*, 1476–1482 (doi: 10.1016/j.solmat.2008.06.012).
- [129] J. Kim, G. Kim, Y. Choi, J. Lee, S. Heum Park and K. Lee, "Light-soaking issue in polymer solar cells: Photoinduced energy level alignment at the sol-gel processed metal oxide and indium tin oxide interface", *Journal of Applied Physics* **2012**, *111*, 114511 (doi: 10.1063/1.4728173).
- [130] S. Cho, K. Lee and A. J. Heeger, "Extended Lifetime of Organic Field-Effect Transistors Encapsulated with Titanium Sub-Oxide as an "Active" Passivation/Barrier Layer", *Advanced Materials* **2009**, *21*, 1941–1944 (doi: 10.1002/adma.200803013).
- [131] T. Kuwabara, H. Sugiyama, M. Kuzuba, T. Yamaguchi and K. Takahashi, "Inverted bulk-heterojunction organic solar cell using chemical bath deposited titanium oxide as electron collection layer", *Organic Electronics* **2010**, *11*, 1136–1140 (doi: 10.1016/j.orgel.2010.04.008).
- [132] J. Y. Kim, S. H. Kim, H.-H. Lee, K. Lee, W. Ma, X. Gong and A. J. Heeger, "New Architecture for High-Efficiency Polymer Photovoltaic Cells Using Solution-Based Titanium Oxide as an Optical Spacer", *Advanced Materials* **2006**, *18*, 572–576 (doi: 10.1002/adma.200501825).

- [133] W. M. H. Sachtler, G. J. H. Dorgelo and A. A. Holscher, "The work function of gold", *Surface Science* **1966**, 5, 221–229.
- [134] M. Uda, A. Nakamura and T. Yamamoto, "Work function of polycrystalline Ag, Au and Al", *Journal of Electron Spectroscopy and Related Phenomena* **1998**, 88-91, 643–648.
- [135] J. S. Kim, B. Lägél, E. Moons, N. Johansson, I. D. Baikie, W. R. Salaneck, R. H. Friend and F. Cacialli, "Kelvin probe and ultraviolet photoemission measurements of indium tin oxide work function : a comparison", *Synthetic Metals* **2000**, 111-112, 311–314.
- [136] L. Chkoda, C. Heske, M. Sokolowski, E. Umbach, F. Steuber, J. Staudigel, M. Stößel and J. Simmerer, "Work function of ITO substrates and band-offsets at the TPD/ITO interface determined by photoelectron spectroscopy", *Synthetic Metals* **2000**, 111-112, 315–319 (doi: 10.1016/S0379-6779(99)00355-0).
- [137] Y. Park, V. Choong, Y. Gao, B. R. Hsieh and C. W. Tang, "Work function of indium tin oxide transparent conductor measured by photoelectron spectroscopy", *Applied Physics Letters* **1996**, 68, 2699 (doi: 10.1063/1.116313).
- [138] A. Manor, E. A. Katz, T. Tromholt and F. C. Krebs, "Enhancing functionality of ZnO hole blocking layer in organic photovoltaics", *Solar Energy Materials and Solar Cells* **2012**, 98, 491–493 (doi: 10.1016/j.solmat.2011.11.026).
- [139] Z. Lin, C. Jiang, C. Zhu and J. Zhang, "Development of Inverted Organic Solar Cells with TiO<sub>2</sub> Interface Layer by Using Low-Temperature Atomic Layer Deposition" **2013**, 5, 713–718.

- [140] S. Sista, M.-H. Park, Z. Hong, Y. Wu, J. Hou, W. L. Kwan, G. Li and Y. Yang, "Highly efficient tandem polymer photovoltaic cells", *Advanced Materials* **2010**, *22*, 380–383 (doi: 10.1002/adma.200901624).
- [141] M. Glatthaar, M. Riede, N. Keegan, K. Sylvester-Hvid, B. Zimmermann, M. Niggemann, a. Hinsch and a. Gombert, "Efficiency limiting factors of organic bulk heterojunction solar cells identified by electrical impedance spectroscopy", *Solar Energy Materials and Solar Cells* **2007**, *91*, 390–393 (doi: 10.1016/j.solmat.2006.10.020).
- [142] M. R. Lilliedal, A. J. Medford, M. V. Madsen, K. Norrman and F. C. Krebs, "The effect of post-processing treatments on inflection points in current–voltage curves of roll-to-roll processed polymer photovoltaics", *Solar Energy Materials and Solar Cells* **2010**, *94*, 2018–2031 (doi: 10.1016/j.solmat.2010.06.007).
- [143] B. A. Gregg, S. Chen and S. Ferrere, "Enhanced Dye-Sensitized Photoconversion Efficiency via Reversible Production of UV-Induced Surface States in Nanoporous TiO<sub>2</sub>" **2003**, *107*, 3019–3029.
- [144] T. Kuwabara, Y. Kawahara, T. Yamaguchi and K. Takahashi, "Characterization of inverted-type organic solar cells with a ZnO layer as the electron collection electrode by ac impedance spectroscopy.", *ACS applied materials & interfaces* **2009**, *1*, 2107–2110 (doi: 10.1021/am900446x).

- [145] K. Komaguchi, T. Maruoka, H. Nakano, I. Imae, Y. Ooyama and Y. Harima, "ESR Study on the Reversible Electron Transfer from O<sub>2</sub><sup>2-</sup> to Ti<sup>4+</sup> on TiO<sub>2</sub> Nanoparticles Induced by Visible-Light Illumination" **2009**, 1160–1163.
- [146] R. Wang, K. Hashimoto, A. Fujishima, M. Chikuni, E. Kojima, A. Kitamura, M. Shimohigoshi and T. Watanabe, "Photogeneration of Highly Amphiphilic TiO<sub>2</sub> Surfaces" **1998**, *10*, 135–138.
- [147] G. K. Mor, S. Kim, M. Paulose, O. K. Varghese, K. Shankar, J. Basham and C. A. Grimes, "Visible to near-infrared light harvesting in TiO<sub>2</sub> nanotube array-P3HT based heterojunction solar cells.", *Nano letters* **2009**, *9*, 4250–4257 (doi: 10.1021/nl9024853).
- [148] S. Jeong, E. C. Garnett, S. Wang, Z. Yu, S. Fan, M. L. Brongersma, M. D. McGehee and Y. Cui, "Hybrid silicon nanocone-polymer solar cells.", *Nano letters* **2012**, *12*, 2971–2976 (doi: 10.1021/nl300713x).
- [149] K.-Q. Peng and S.-T. Lee, "Silicon nanowires for photovoltaic solar energy conversion.", *Advanced Materials* **2011**, *23*, 198–215 (doi: 10.1002/adma.201002410).
- [150] S.-C. Shiu, J.-J. Chao, S.-C. Hung, C.-L. Yeh and C.-F. Lin, "Morphology Dependence of Silicon Nanowire/Poly(3,4-ethylenedioxythiophene):Poly(styrenesulfonate) Heterojunction Solar Cells", *Chemistry of Materials* **2010**, *22*, 3108–3113 (doi: 10.1021/cm100086x).

- [151] G. Mariani, Y. Wang, P.-S. Wong, A. Lech, C.-H. Hung, J. Shapiro, S. Prikhodko, M. El-Kady, R. B. Kaner and D. L. Huffaker, "Three-dimensional core-shell hybrid solar cells via controlled in situ materials engineering.", *Nano letters* **2012**, *12*, 3581–3586 (doi: 10.1021/nl301251q).
- [152] P. Lu and A. V Walker, "Making Nanoflowerbeds: Reaction Pathways Involved in the Selective Chemical Bath Deposition of ZnS on Functionalized Alkanethiolate Self- Assembled Monolayers", *ACS nano* **2009**, *3*, 370–378.
- [153] X. Meng, Y. Lu, B. Yang, G. Yi and J. Jia, "Fabrication and photoelectrochemical characteristics of the patterned CdS microarrays on indium tin oxide substrates.", *ACS applied materials & interfaces* **2010**, *2*, 3467–3472 (doi: 10.1021/am100548w).
- [154] H. Lin, H. Liu, X. Qian, S.-W. Lai, Y. Li, N. Chen, C. Ouyang, C.-M. Che and Y. Li, "Constructing a blue light photodetector on inorganic/organic p-n heterojunction nanowire arrays.", *Inorganic chemistry* **2011**, *50*, 7749–7753 (doi: 10.1021/ic200900a).
- [155] X. Fang, L. Wu and L. Hu, "ZnS Nanostructure Arrays: A Developing Material Star.", *Advanced Materials* **2011**, *23*, 585–598 (doi: 10.1002/adma.201003624).
- [156] S. Mokkaapati and K. R. Catchpole, "Nanophotonic light trapping in solar cells", *Journal of Applied Physics* **2012**, *112*, 101101 (doi: 10.1063/1.4747795).

- [157] J. Jean, S. Chang, P. R. Brown, J. J. Cheng, P. H. Rekemeyer, M. G. Bawendi, S. Gradečak and V. Bulović, "ZnO nanowire arrays for enhanced photocurrent in PbS quantum dot solar cells.", *Advanced Materials* **2013**, *25*, 2790–2796 (doi: 10.1002/adma.201204192).
- [158] F. F. Amos, S. a Morin, J. a Streifer, R. J. Hamers and S. Jin, "Photodetector arrays directly assembled onto polymer substrates from aqueous solution.", *Journal of the American Chemical Society* **2007**, *129*, 14296–14302 (doi: 10.1021/ja073675b).
- [159] Y. K. Hwang, S. Y. Woo, J. H. Lee, D. Jung and Y. Kwon, "Micropatterned CdS Thin Films by Selective Solution Deposition Using Microcontact Printing Techniques", *Chemistry of Materials* **2000**, *12*, 2059–2063.
- [160] Y. Lu, S. Liang, M. Chen and J. Jia, "Fabrication and characterization of positive and negative copper sulfide micropatterns on self-assembled monolayers.", *Journal of colloid and interface science* **2009**, *332*, 32–38 (doi: 10.1016/j.jcis.2008.11.066).
- [161] B. Radha, S. Kiruthika and G. U. Kulkarni, "Metal anion-alkyl ammonium complexes as direct write precursors to produce nanopatterns of metals, nitrides, oxides, sulfides, and alloys.", *Journal of the American Chemical Society* **2011**, *133*, 12706–13 (doi: 10.1021/ja2039612).



- [162] L. Persano, A. Camposeo, F. Di Benedetto, R. Stabile, A. M. Laera, E. Piscopiello, L. Tapfer and D. Pisignano, "CdS-polymer nanocomposites and light-emitting fibers by in situ electron-beam synthesis and lithography.", *Advanced materials (Deerfield Beach, Fla.)* **2012**, *24*, 5320–6 (doi: 10.1002/adma.201202440).
- [163] L. R. Giam, S. He, N. E. Horwitz, D. J. Eichelsdoerfer, J. Chai, Z. Zheng, D. Kim, W. Shim and C. a Mirkin, "Positionally defined, binary semiconductor nanoparticles synthesized by scanning probe block copolymer lithography.", *Nano letters* **2012**, *12*, 1022–5 (doi: 10.1021/nl204233r).
- [164] H. Chu, L. Ding, J. Wang, X. Li, L. You and Y. Li, "In Situ Epitaxial Growth of Triangular CdS Nanoplates on Mica by Dip-Pen Nanolithography", *The Journal of Physical Chemistry C* **2008**, *112*, 18938–18942 (doi: 10.1021/jp807746g).
- [165] J. M. Clark, G. Kociok-Köhn, N. J. Harnett, M. S. Hill, R. Hill, K. C. Molloy, H. Saponia, D. Stanton and A. Sudlow, "Formation of PbS materials from lead xanthate precursors.", *Dalton transactions (Cambridge, England : 2003)* **2011**, *40*, 6893–6900 (doi: 10.1039/c1dt10273g).
- [166] M. Tejos, B. G. Rolón, R. del Río and G. Cabello, "CdS amorphous thin films photochemical synthesis and optical characterization", *Materials Science in Semiconductor Processing* **2008**, *11*, 94–99 (doi: 10.1016/j.mssp.2009.04.004).

- [167] J. J. Nairn, P. J. Shapiro, B. Twamley, T. Pounds, R. von Wandruszka, T. R. Fletcher, M. Williams, C. Wang and M. G. Norton, "Preparation of ultrafine chalcopyrite nanoparticles via the photochemical decomposition of molecular single-source precursors.", *Nano letters* **2006**, 6, 1218–1223 (doi: 10.1021/nl060661f).
- [168] H. J. Lewerenz, "Development of copperindiumdisulfide into a solar material", *Solar Energy Materials and Solar Cells* **2004**, 83, 395–407 (doi: 10.1016/j.solmat.2004.02.034).
- [169] M. C. Zouaghi, T. Ben Nasrallah, S. Marsillac and J. C. Bernede, "Physico-chemical characterization of spray-deposited CuInS<sub>2</sub> thin films", *Thin Solid Films* **2001**, 382, 39–46.
- [170] C. Wagner and N. Harned, "EUV lithography: Lithography gets extreme", *Nature Photonics* **2010**, 4, 24–26 (doi: 10.1038/nphoton.2009.251).
- [171] B. Päivänranta, A. Langner, E. Kirk, C. David and Y. Ekinci, "Sub-10 nm patterning using EUV interference lithography.", *Nanotechnology* **2011**, 22, 375302 (doi: 10.1088/0957-4484/22/37/375302).
- [172] V. Auzelyte, D. Grützmacher, L. J. Heyderman, T. Thomson, A. Turchanin, C. David, H. H. Solak, S. Olliges, C. Padeste, P. K. Sahoo, F. Luo, C. Dais and P. Farquet, "Extreme ultraviolet interference lithography at the Paul Scherrer Institut", *Journal of Micro/Nanolithography, MEMS, and MOEMS* **2009**, 8, 21204–21210 (doi: 10.1117/1.3116559).

- [173] L. Wang, B. Terhalle, V. a. Guzenko, A. Farhan, M. Hojeij and Y. Ekinici, "Generation of high-resolution kagome lattice structures using extreme ultraviolet interference lithography", *Applied Physics Letters* **2012**, *101*, 093104 (doi: 10.1063/1.4748758).
- [174] L. Wang, B. Terhalle, M. Hojeij, V. a. Guzenko and Y. Ekinici, "High-resolution nanopatterning by achromatic spatial frequency multiplication with electroplated grating structures", *Journal of Vacuum Science & Technology B: Microelectronics and Nanometer Structures* **2012**, *30*, 031603 (doi: 10.1116/1.3697753).
- [175] L. Wang, H. H. Solak and Y. Ekinici, "Fabrication of high-resolution large-area patterns using EUV interference lithography in a scan-exposure mode.", *Nanotechnology* **2012**, *23*, 305303 (doi: 10.1088/0957-4484/23/30/305303).
- [176] I. Horcas, R. Fernández, J. M. Gómez-Rodríguez, J. Colchero, J. Gómez-Herrero and a M. Baro, "WSXM: a software for scanning probe microscopy and a tool for nanotechnology.", *The Review of scientific instruments* **2007**, *78*, 013705 (doi: 10.1063/1.2432410).
- [177] G. Socrates, *Infrared Characteristic Group Frequences: Tables and Charts* , Second Edi. , Chichester: Wiley, **1994**.
- [178] D. Barreca, A. Gasparotto, C. Maragno, R. Seraglia, E. Tondello, A. Venzo, V. Krishnan and H. Bertagnolli, "Synthesis and characterization of zinc bis(O-isopropylxanthate) as a single-source chemical vapor deposition precursor for ZnS", *Applied Organometallic Chemistry* **2005**, *19*, 1002–1009 (doi: 10.1002/aoc.948).

## 5 List of Publications

### Articles

Flexible Polymer/Copper Indium Sulfide Hybrid Solar Cells and Modules Based on the Metal Xanthate Route and Low Temperature Annealing - Fradler, C.; Rath, T.; Dunst, S.; Letofsky-Papst, I.; Saf, R.; Kunert, B.; Hofer, F.; Resel, R.; Trimmel G.; *in press* (doi: 10.1016/j.solmat.2014.01.043).

Direct Extreme UV-lithographic conversion of metal xanthates into nanostructured metal sulfide layers for hybrid photovoltaics - Rath, T.; Padeste, C.; Vockenhuber, M.; Fradler, C.; Edler, M.; Reichmann, A.; Letofsky-Papst, I.; Hofer, F.; Ekinici, Y.; Griesser, T.; *Journal of Materials Chemistry A*, 2013, 1, 11135-11140 (doi: 10.1039/c3ta12592k).

### Oral Presentations

Stability issues of CuInS<sub>2</sub>-polymer hybrid solar cells - Dunst, S.; Nestl, S.; Moscher, S.; Fradler, C.; Rath, T.; Trimmel, G.: *EMRS Spring Meeting 2012*, Strasbourg, 2012.

Copper Indium Sulphide / Polymer Nanocomposite Solar Cells - Rath, T.; Arar, M.; Pein, A.; Fradler, C.; Kaltenhauser, V.; Edler, M.; Moscher, S.; Trattinig, R.; List, E.; Haas, W.; Dunst, S.; Hofer, F.; Trimmel, G.: *27th European PV Solar Energy Conference and Exhibition*, Frankfurt, 2012.

Polymer Nanocomposite Solar Cells based on in-situ formed CuInS<sub>2</sub> - Fradler, C.; Rath, T.; Edler, M.; Fischereder, A.; Moscher, S.; Pein, A.; Trattnig, R.; Mauthner, G.; List, E.; Haas, W.; Hofer, F.; Trimmel, G.: *SPIE Optics + Photonics: Organic Photovoltaics*, San Diego, 2011.

Application of Nanocomposite Layers of Sulfidic Nanoparticles and Electroactive Polymers in Hybrid Photovoltaics - Rath, T.; Maier, E.; Larissegger, S.; Fischereder, A.; Edler, M.; Haas, W.; Fradler, C.; Moscher, S.; Santis Alvarez, A.; Saf, R.; Mauthner, G.; List, E.; Hofer, F.; Trimmel, G.; *European Polymer Congress 2009*, Graz, 2009.

Hybrid Photovoltaic Cells via a Novel Direct Route - Maier, E.; Edler, M.; Fischereder, A.; Fradler, C.; Haas, W.; Hofer, F.; Larissegger, S.; Mauthner, G.; Meischler, D.; Pein, A.; Rath, T.; Saf, R.; Santis Alvarez, A.; Trattnig, R.; Stelzer, F.; List, E.; Trimmel, G.: *NAWI Graz Workshop 2009*, Graz, 2009.

Application of Nanocomposite Layers consisting of Electroactive Polymers and Sulfidic Nanoparticles in Hybrid Photovoltaics - Rath, T.; Maier, E.; Fischereder, A.; Edler, M.; Haas, W.; Fradler, C.; Moscher, S.; Larissegger, S.; Santis Alvarez, A.; Meischler, D.; Saf, R.; Mauthner, G.; List, E.; Hofer, F.; Trimmel, G.: *SLONANO 2009*, Ljubljana, 2009.

### **Poster Presentations**

Inverted P*Si*F-DBT/Copper Indium Sulfide Hybrid Solar Sells: Optimization and Enhancement - Fradler, C.; Rath, T.; Trimmel, G.: *39th IEEE Photovoltaic Specialists Conference*, Tampa, 2013.

Polymer / copper indium sulphide hybrid solar cells. - Rath, T.; Edler, M.; Haas, W.; Moscher, S.; Trattnig, R.; Jäger, M.; Pein, A.; Kaltenhauser, V.; Dunst, S.; Arar, M.; Fradler, C.; Saf, R.; Postl, M.; Seidl, M.; Bansal, N.; Haque, S. A.; Hofer, F.; List, E.; Trimmel, G.: *EMRS Spring Meeting 2012*, Strasbourg, 2012.

Fill Factor Enhancement for PSiF-DBT/CIS Solar Cells through Silver-modified Aluminum Electrodes - Arar, M.; Pein, A.; Haas, W.; Kaltenhauser, V.; Fradler, C.; Dunst, S.; Hofer, F.; Norrman, K.; Krebs, F. C.; Rath, T.; Trimmel, G.: *Plastic Electronics 2012*, Dresden, 2012.

A Direct In Situ-Preparation Route for Organic-Inorganic Hybrid Solar Cells Based on Metal Sulfides and Conjugated Polymers - Rath, T.; Edler, M.; Haas, W.; Moscher, S.; Pein, A.; Kaltenhauser, V.; Dunst, S.; Arar, M.; Fradler, C.; Saf, R.; Trattnig, R.; Jäger, M.; Postl, M.; Seidl, M.; Bansal, N.; Haque, S. A.; Hofer, F.; List, E.; Trimmel, G.: *Plastic Electronics 2012*, Dresden, 2012.

A time resolved X-ray scattering study of the thermal formation process of thin nanocrystalline metal sulfide layers - Rath, T.; Larissegger, S.; Fradler, C.; Amenitsch, H.; Trimmel, G.: *EMRS 2009*, Strasbourg, 2009.

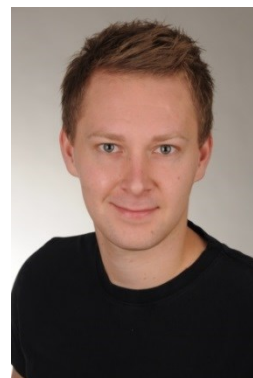
Direct Formation of Sulfidic Nanoparticles in Semiconducting Organic Matrices for Hybrid Photovoltaics - Trimmel, G.; Maier, E.; Rath, T.; Larissegger, S.; Fischereder, A.; Edler, M.; Haas, W.; Fradler, C.; Moscher, S.; Santis Alvarez, A.; Saf, R.; Mauthner, G.; List, E.; Hofer, F.: *EMRS 2009*, Strasbourg, 2009.

## 6 Curriculum Vitae

### PERSÖNLICHE DATEN

---

<b>Name</b>	Christopher Fradler, DI
<b>Geboren in</b>	Graz, am 25.07.1984
<b>Adresse</b>	Grottenhofstrasse 10/2/11, 8053 Graz
<b>Staatsbürgerschaft</b>	Österreich



### AUSBILDUNG

---

<i>seit 10/2010</i>	<b>Doktoratsstudium der techn. Wissenschaften, TU Graz</b>
<i>10/2002 - 09/2010</i>	<b>Diplomstudium der Technischen Chemie, TU Graz</b> <ul style="list-style-type: none"><li>– Studiengang Chemieingenieurwesen</li><li>– Diplomarbeit: “Investigations on the Layer Formation in Nanocomposite Solar Cells“</li></ul>
<i>09/1994 - 07/2002</i>	<b>Bundesrealgymnasium Oeverseegasse, Graz</b> <ul style="list-style-type: none"><li>– Matura mit ausgezeichnetem Erfolg bestanden</li><li>– Teilnahme am Bundeswettbewerb der Chemie-Olympiade 2002</li></ul>
<i>09/1990 - 07/1994</i>	<b>Volksschule der Grazer Schulschwestern, Graz</b>

---

## Berufserfahrung

---

*seit 01/2011* **Betreuung von Studierenden, TU Graz**

Laborübungen, Projektlabore, Abschlussarbeiten

*02/2007 –  
11/2009* **Selbständig erwerbstätig für Roche Diagnostics Graz GmbH**

- Beschäftigungsumfang: 20 Stunden/Woche
- Abteilung: R&D/Software-Test und Qualitätsmanagement
  - Test von Bedienungs- und Steuerungssoftware im Rahmen einer Produktentwicklung
  - Validierung von Testsoftware

*07/2006 –  
08/2006* **Praktikum: Roche Diagnostics Graz GmbH**

Sechswöchiges Praktikum in der Abteilung R&D/Projektmanagement

- Projektdokumentation
- Produktanforderungsmanagement

## ZIVILDIENST

---

*10/2007 -  
06/2008* **Jugendzentrum DonBosco Graz**

Sozial- und Lernbetreuung von Kindern und Jugendlichen



## ZUSÄTZLICHE QUALIFIKATIONEN

---

- EDV-Kenntnisse*
- MS Office
  - Origin
  - Programmierkenntnisse (VBA)
  - IBM Rational RequisitePro und IBM Rational ClearQuest
- Sprachen*
- Deutsch Muttersprache
  - Englisch Verhandlungssicher
  - Spanisch Grundkenntnisse
- Weiterbildungen*
- Absolvierung zahlreicher Seminare am Zentrum für soziale Kompetenz, Karl-Franzens-Universität Graz**
- Grundlagen der Rhetorik
  - Führen von MitarbeiterInnen und Teams
  - Kommunikationstraining
  - Gruppendynamik
- Sportmanagement Basis Kurs der BSO**

## PERSÖNLICHE INTERESSEN

---

### **Tischtennis**

Jahrelanger Bundesligaspieler und Trainer, oftmaliger steirischer Meister

*Ehrenamtliche Tätigkeiten* seit 09/2010 **Mitglied der Jugendkommission der Bundes-Sportorganisation (BSO)**

07/2002 - 12/2011 **Vorstandsmitglied des Tischtennisvereins Don Bosco Graz**